

PLACE IN RETURN BOX to remove this checkout from your record.
TO AVOID FINES return on or before date due.

DATE DUE	DATE DUE	DATE DUE
_____	_____	_____
_____	_____	_____
_____	_____	_____
_____	_____	_____
_____	_____	_____
_____	_____	_____
_____	_____	_____

MSU Is An Affirmative Action/Equal Opportunity Institution

c:\circ\dstdue.pm3-p.1

**VIBRATIONAL STUDIES OF METALLOPROTEINS AND
RELATED MODEL COMPOUNDS**

By

Matthew Terrell Gardner

A DISSERTATION

**Submitted to
Michigan State University
in partial fulfillment of the requirements
for the degree of**

DOCTOR OF PHILOSOPHY

Department of Chemistry

1997

An ultimate goal of the understanding of functions. Vibrational spectroscopy has the ability to provide structural information from vibrational spectra. This is particularly true for three systems, in order to determine the mechanism by which the order of increasing complexity of compound synthesis, the center of oxidation, the vibrational properties of the cyanide moiety, and the secondary structure of the enzyme, which

ABSTRACT

VIBRATIONAL STUDIES OF METALLOPROTEINS AND RELATED MODEL COMPOUNDS

By

Matthew T. Gardner

An ultimate goal of biophysical studies of enzymes is to achieve an understanding of the mechanism by which enzymes carry out their biological functions. Vibrational spectroscopy is just one method that can be used to achieve this goal. It has the advantage that it has the potential to elucidate both mechanistic, and structural information about the system being studied. We have applied two forms of vibrational spectroscopies, resonance Raman, and infrared absorption spectroscopy, to three systems, a synthetic model of an enzymatic active site, and two enzymatic systems, in order to achieve a greater understanding of the structure, function and mechanism by which they operate. The experiments detailed here, are arranged in order of increasing complexity and technical challenge. The first system, a model compound synthesized as an analogue to the cyanide ligated form of the binuclear center of oxidized cytochrome c oxidase, was studied, and found to exhibit unique vibrational properties. These properties are attributed to the bridging geometry of the cyanide moiety between the copper and iron atoms of the model complex.

The second system presented is the enzyme soluble guanylate cyclase. This enzyme, which is the only known physiological receptor for •NO, was found to have a

unique heme

stretching fre

heme-enzyme

accounts for

binding kinet

The

photosynthesi

molecular oxy

manganese at

spectroscopy.

information re

cycle of the en

unique heme-binding pocket. The CO-bound form of this enzyme exhibits a CO stretching frequency higher than has been previously reported for any CO-ligated heme-enzyme. This, we confirm, is attributable to a highly polar heme pocket, which accounts for not only the observed vibrational properties of CO, but also the ligand binding kinetics of the enzyme.

The third system studied is the oxygen evolving complex of the photosynthetic enzyme, photosystem II. This enzyme, which oxidizes water to molecular oxygen in plants and cyanobacteria, has an active site consisting of four manganese atoms. We have developed novel methods whereby, using infrared spectroscopy, we can look directly at the manganese cluster and thus have access to information regarding the specific molecular intermediates in the oxygen evolving cycle of the enzyme.

To my Dad

There are ma

made to my w

own way, ma

and others as w

On the work si

-The te

Specific

Ron Ha

and John

and from

advice a

-The C

are ble

These g

-The B

that I r

what w

ACKNOWLEDGEMENTS

There are many folks to whom I owe a great deal. The contributions people have made to my work and my life over the past six years vary widely. But each, in their own way, made my life better, my work easier, or both. I would like everyone here, and others as well, to accept my heartfelt thanks.

On the work side of things, the folks I especially would like to thank include:

- The technical support/professional staff here at Michigan State University.

Specifically I would like to thank Russ Geyer, Sam Jackson, Dick Menke, Ron Haas, Scott Sanderson, Scott Bankroff, Manfred Langer, Keki Mistry, and John Rugis. Each one of them has the ability to take some ethereal idea, and from that, produce exactly what it is that that you need. Their input, advice and expertise was indispensable

- The Computer gang, Dr. Tom Carter, Dr. Tom Atkinson, and Paul Reed. We are blessed here at MSU with top-notch computer facilities and networks. These guys were always available and helpful in many different ways.

- The Business Office. Those folks put up with my endless requests for things that I needed yesterday. I appreciate their efforts and their understanding of what was usually my own lack of foresight.

On the person

gratitude:

- The

every

intelle

behol

- My

backp

always

-The D

shared

definite

how m

-Profes

convinc

Bowlby

not taki

for alw

providi

not leas

-My cur

P., Pier

On the personal side of things, there's even more folks to whom I owe a lot of gratitude:

- The gang at Science Theatre. It was an immense pleasure to work with everyone at ST. The dedication of this group of people, the intensity of their intellects, and the fun they pumped into everything we did, was awesome to behold. Thanks for letting me work with you and for you.

- My friend Chris. Our adventures together learning how to home brew, our backpacking journeys, and really getting into photography are things I'll always cherish. And we'll do a ton more of them (So, middle of September??)

- The Dagwoods Gang: Chris, Sara Helvoigt, Per Askeland and Michelle. We shared a lot of good times together. My sanity and my sense of humor were definitely retained because of the time we spent there. If you thought about how much money we have spent there....

- Professor Charlie Yocum, for being the person who single handedly convinced me that being a died-in-the-wool liberal was a good thing. Dr. Neil Bowlby for having an expansive intellect that I envy, Dr. Matthew Espe for not taking any shit from this "liberal arts" East-Coaster, Dr. Curt Hoganson for always asking the right questions, for keeping me honest, and for providing incredible insight to just about any scientific discussion and last but not least, Dr. Michelle Mac, for being a friend and confidant through it all.

- My current research group: Andy, Curt, John, Kristy, Denis, Costas, Michelle P., Pierre, Nadia, Heather, Marilena, Catherine, Matt, Kris, Gwynne and Hans.

Y

m

-P

Es

Go

lot

-My

my

not o

-Prof

impor

somet

-Dr.

indispe

details

make a

-My ad

me how

ranging

enthusia

as scien

his pois

You folks have put up with me above and beyond the call of duty and made my time here a blast. Thanks.

-Past members of my research group and other colleagues, including Dr. Matt Espe, Dr. Geurt Deinum, Dr. Yvonne Gindt, Dr. Craig Essenmacher, Dr. Jerry Godbout, and Dr. Tom Halasinski. The subbasement was a lot more fun and a lot more interesting with those last two guys.

-My friends here in Lansing. Danielle and Rod, Bill and Aimee. You folks are my friends for life. The fun we had and the games we played, made Lansing not only tolerable, but a place I look forward to returning to.

-Professor George Leroi who allowed me the use of his lab space, and more importantly, whose warm and compassionate way of interacting with people is something I aspire to.

-Dr. Andy Chu. Andy's help, friendship, and collaboration was an indispensable aspect of the photosystem II work. His dogged attention to details ensured the biological relevance of all that we did. This work is going to make a splash because of him.

-My advisor, Professor Jerry Babcock, for more than a few things. He taught me how to do science (if he wants to claim credit). He indulged my wide-ranging interests, yet, when necessary, beat me to a pulp to stay focused. His enthusiasm for science is infectious, and his attention to us as people, as well as scientists, made graduate school a complete experience. I will never forget his poise delivering the plenary lecture at Montpellier. Nor will I forget his

laug

willi

in m

-My

Mon

Pete

each

-Sue

have

learn

made

laughing in the face of danger on the rapids of the Sturgeon River, or his willingness to handover his hard –earned dough on poker nights. I owe a lot, in many different ways, to Jerry.

-My family. Without their love and support, I couldn't have done this. My Mom, Maich, my stepdad, Ed, my stepmom Suze, my greatly missed dad, Peter, my brothers Chris, Josh and Zack, and my sisters Amanda and Griffin, each played a huge role in this work, and for that I will always be grateful.

-Sue. She is my partner and friend. We've been through a lot together and have many more adventures coming. We have learned, and will continue to learn a lot from each other. Her love and support, kindness and affection have made these years wonderful. We're a good team.

LIST OF T

LIST OF F

CHAPTER

Abs

Vibr

Infra

Ram

Four

Sign

Refe

CHAPTER .

Abstr

Intro

Mate

Resul

Discu

Refere

TABLE OF CONTENTS

LIST OF TABLES.....	x
LIST OF FIGURES.....	xi
 CHAPTER 1 Introduction to Vibrational Spectroscopy of Biological Systems	
Abstract.....	1
Vibrational Spectroscopy of Biological Systems.....	2
Infrared Spectroscopy.....	3
Raman Spectroscopy.....	4
Fourier Transform Infrared (FTIR) Spectroscopy.....	11
Signal-to-Noise Considerations in FTIR.....	16
References.....	20
 CHAPTER 2 Vibrational Analysis Of A Molecular Heme-Copper Assembly With A Nearly Linear Fe^{III}-Cn-Cu^{II} Bridge: Insight Into Cyanide Binding To Fully Oxidized Cytochrome C Oxidase	
Abstract.....	21
Introduction.....	22
Materials and Methods.....	26
Results	
UV-Visible Spectroscopy.....	33
Infrared Spectroscopy.....	33
Resonance Raman Spectroscopy.....	40
Vibrational Analysis.....	40
Discussion	
Electronic Structure and Vibrational Characteristics.....	46
Normal Mode Composition.....	47
Resonance Enhancement Conditions.....	51
Relevance to Cytochrome c Oxidase.....	52
References.....	57

CHAPTER 3 S

TE

C

Abstract

Introduc

Ir

R

Materials

Results

Referenc

CHAPTER 4 P

I

Abstract

Introduc

What W

FTIR of

Detector

Window

Temper

Conclus

Referenc

CHAPTER 5 I

I

Abstract

Introduc

Material

Results

Discuss

Conclus

Referenc

CHAPTER 3	Small Molecule Binding To Heme Proteins: Vibrational Spectroscopy of The Ligand Binding Site in The •NO Binding Enzyme Soluble Guanylate Cyclase	
Abstract.....		60
Introduction.....		61
Infrared Spectroscopy of Heme Proteins.....		62
Resonance Raman of Heme Ligand Interactions.....		64
Materials and Methods.....		74
Results and Discussion.....		74
References.....		78
 CHAPTER 4	 Probing Low-Frequency Vibrations in Metalloproteins Using Light Induced Infrared Difference Spectroscopy: Challenges and Solutions	
Abstract.....		80
Introduction.....		80
What Will be Found in the Low-Frequency Region?.....		83
FTIR of Aqueous Systems: The Low Frequency Challenge.....		84
Detectors.....		96
Window/Substrate Materials.....		99
Temperature Control.....		102
Conclusions.....		108
References.....		110
 CHAPTER 5	 Low Frequency Modes in the Light-Induced FTIR Difference Spectrum of Photosystem II	
Abstract.....		112
Introduction.....		113
Materials and Methods.....		130
Results.....		133
Discussion.....		158
Conclusions.....		176
References.....		179

Table 2-1

Table 2-2

Table 2-3

Table 2-4

Table 2-5

Table 3-1

Table 4-1

Table 4-2

Table 4-3

Table 5-1

Table 5-2

Table 5-3

List of Tables

Table 2-1	Isotopic Dependence of Vibrational Frequencies.....	36
Table 2-2	Extinction Coefficients of Various C≡N Stretches.....	36
Table 2-3	Vibrational Frequencies for C≡N in Selected Structures.....	39
Table 2-4	Force Constants for NCA of Fe-CN-Cu system.....	44
Table 2-5	Experimental and Calculated Vibrational Frequencies (cm ⁻¹).....	45
Table 3-1	Vibrational Frequencies of Various CO-adducts of Heme-enzymes.....	73
Table 4-1	Vibrational Frequencies of Protein and Metal-Ligand Structures.....	82
Table 4-2	Infrared Absorbances of H ₂ O and D ₂ O.....	87
Table 4-3	Properties of Infrared Window Materials.....	101
Table 5-1	Vibrational Data (1800-1000 cm ⁻¹) From Various LI-FTIR Measurements of Photosystem II.....	162
Table 5-2	Group Frequencies of Protein-based Vibrations.....	163
Table 5-3	Low-Frequency Vibrations Possibly Present in Photosystem II.....	168

Figure 1-1: S

Figure 1-2: S

Figure 1-3: S

Figure 2-1: T
E
r

Figure 2-2: U
a
V
a

Figure 2-3: F
i
Y

Figure 2-4: S

Figure 2-5: S

Figure 2-6: S

Figure 2-7: S

List of Figures

Figure 1-1:	Schematic of Raman scattering spectrometer.....	7
Figure 1-2:	Schematic of scanning infrared spectrometer.....	12
Figure 1-3:	Schematic of Michelson Interferometer.....	14
Figure 2-1:	Top: Schematic representation of [(1-MeIm)Fe(OEP)-CN-Cu(Me ₆ tren)] ²⁺ Bottom: Model used for normal coordinate analysis. Point masses represent atoms or fractional representations of ligands.....	25
Figure 2-2:	UV-Vis absorption spectra of “bridged”, [(py)Fe(OEP)-CN-Cu(Me ₆ tren)], and “unbridged”, [(py)Fe(OEP)-CN], complexes. Sample concentrations were 2.2 mM (bridged) and 1.9mM (unbridged). Spectra were dissolve in acetone and spectra were recorded in a CaF ₂ cell, 50μM pathlength.....	34
Figure 2-3:	FTIR spectrum of [(1-MeIm)Fe(OEP)-CN-Cu(Me ₆ tren)] ²⁺ and isotopomers. Spectral conditions described in Materials and Methods.....	37
Figure 2-4:	FTIR spectrum of [(1-MeIm)Fe(OEP)-CN-Cu(Me ₆ tren)] ²⁺ and isotopomers. Spectral conditions described in Materials and Methods.....	38
Figure 2-5:	Resonance Raman spectrum of [(1-MeIm)Fe(OEP)-CN-Cu(Me ₆ tren)] ²⁺ and isotopomers. Spectral conditions described in Materials and Methods.....	41
Figure 2-6:	Resonance Raman spectrum of [(1-MeIm)Fe(OEP)-CN-Cu(Me ₆ tren)] ²⁺ and isotopomers. Spectral conditions described in Materials and Methods.....	42
Figure 2-7:	Plot of calculated vibrational frequencies versus Fe-C stretching/Fe-C-N bending interaction force constant.....	49

Figure 2-8:

Figure 2-9:

Figure 3-1:

Figure 3-2:

Figure 3-3:

Figure 3-4:

Figure 3-5:

Figure 4-1:

Figure 4-2:

Figure 4-3:

Figure 4-4:

Figure 4-5:

Figure 4-6:

Figure 2-8:	Plot of calculated vibrational frequencies versus Cu-N stretching/Cu-N-C bending interaction force constant.....	50
Figure 2-9:	Representation of the binuclear center of oxidized cytochrome c oxidase.....	55
Figure 3-1:	Infrared absorption spectrum of water, CaF ₂ cell, 50μm pathlength, 25 °C. Approximate frequencies of X-Y stretches of heme-ligated XY diatomic ligands are shown (XY = C≡N or C≡O).....	65
Figure 3-2:	UV-Vis spectrum of heme-ligand complex ([<i>(py)Fe(OEP)-CN</i>]). Sample concentration = 2.2 mM, in acetone. Spectrum acquired in 50μm CaF ₂ cell, room temperature.....	67
Figure 3-3:	Correlation between Fe-C stretching frequencies and C-O stretching frequencies for a variety of histidine ligated carbonmonoxy heme complexes. Adapted from [16].....	68
Figure 3-4:	Resonance Raman spectrum of isotopomers of carbonmonoxy-soluble guanylate cyclase. Laser excitation λ=423 nm[20].....	72
Figure 3-5:	FTIR spectrum of isotopomers of carbonmonoxy-soluble guanylate cyclase. Spectral conditions given in Materials and Methods.....	76
Figure 4-1:	Infrared absorption spectrum of water. Spectrum acquired in an AgCl cell, room temperature, 32 scans, ~5μm pathlength.....	86
Figure 4-2:	Difference spectrum of water sample showing poor subtraction characteristics below 1000 cm ⁻¹ . 5μm pathlength, 200K, AgCl sample cell.....	88
Figure 4-3:	Construction of a theoretical light-induced difference spectrum.....	91
Figure 4-4:	Partially hydrated films of PSII samples, with and without sucrose in the drying medium. Sample temperature: 25 °C.....	95
Figure 4-5:	Difference bands induced by temperature fluctuation of partially hydrated film of photosystem II. The spectrum was acquired by cooling the sample to 200K, acquiring one spectrum (500 scans), raising the temperature 0.2 °C, and acquiring a second spectrum (500 scans). The ratio of the two spectra resulted in the displayed difference spectrum.....	104
Figure 4-6:	Temperature control system for low temperature FTIR experiments.....	106

Figure 4-7:

Figure 5-1:

Figure 5-2:

Figure 5-3:

Figure 5-4:

Figure 5-5:

Figure 5-6:

Figure 5-7:

Figure 5-8a:

Figure 5-8b:

Figure 5-9:

Figure 5-10a)

Figure 5-11 a)

Figure 4-7:	Sample compartment for low-temperature FTIR experiments.....	107
Figure 5-1:	Schematic of the Photosystem II reaction center. Numbers are approximate molecular weights of the constituent polypeptides. See text for description of components.....	115
Figure 5-2:	Schematic depicting the primary photochemical events in photosystem II.....	116
Figure 5-3:	Kok model for oxygen evolution.....	119
Figure 5-4:	Multiline EPR spectrum of BBY particles, 200K illumination. 8K sample temperature. Spectrum is the difference between a EPR spectrum acquired after illumination at 200K, and the EPR spectrum of the sample before illumination. Microwave power: 2 mW, 20 gauss modulation amplitude, gain = 1×10^5	120
Figure 5-5:	Open “C” model for the manganese cluster of Photosystem II.....	122
Figure 5-6:	Scheme of oxidation states of manganese cluster during the catalytic cycle of water oxidation.....	123
Figure 5-7:	Proposed sequence of steps in the water oxidation process.....	126
Figure 5-8a:	Dark stable EPR signal from Y_D in BBY particles. Microwave power 1mW, 2.5 gauss modulation amplitude, 2 minute scan, room temperature.....	136
Figure 5-8b:	Tris-washed BBY particles, before, and under illumination. Same spectral conditions as Figure 5-8a.....	137
Figure 5-9:	S_2 -multiline signal from partially dehydrated film of O_2 evolving BBY particles illuminated at 200K. 2mW microwave power, 20 gauss modulation amplitude, gain = 1×10^5	138
Figure 5-10a)	(top) EPR spectrum, 200K, partially hydrated BBY particles, b) tris-washed BBY particles before (black) and after (red) illumination. Microwave power = 0.2mW, 4 gauss modulation amplitude, gain = 1×10^5	140
Figure 5-11 a)	(top) and b) (bottom) Black: $S_2Q_A^-/S_1Q_A^-$ light induced FTIR difference spectra of BBY particles, 200K, 9000 scans. Red: “dark-dark” for noise reference.....	142

Figure 5-12a) (U
v

Figure 5-13: N
c
n

Figure 5-14a: l
i
2
2

Figure 5-14b: l
A
T

Figure 5-14c:

Figure 5-15a:

Figure 5-15b:

Figure 5-16 a)

Figure 5-17a)

Figure 5-18a)

Figure 5-19a)

Figure 5-12a) (top) and b) (bottom) Light-induced FTIR difference spectrum of tris-washed BBY particles, 200K. 6000 scans.....	143
Figure 5-13: Multiline EPR spectrum of partially-hydrated reaction center cores. 200 μ g chlorophyll dried on mylar. Microwave power: 2 mW, 20 gauss modulation amplitude, gain = 1×10^5 . Temperature = 8K.....	146
Figure 5-14a: EPR spectrum of O ₂ evolving RCCs, before (black) and under (red) illumination. Integration indicates the formation of chlorophyll radical in approximately ~50% of the centers. Same spectral conditions as Figure 5-10.....	147
Figure 5-14b: EPR spectrum of Tris-washed RCCs at 200K, before (black) and under (red) illumination. Integration of signals shows generation of chlorophyll radical in approximately 85% of centers. Same spectral conditions as Figure 5-10.....	148
Figure 5-14c: EPR spectrum of Sr ²⁺ substituted RCCs at 200K before (black) and after (red) illumination. Integration of signals showed chlorophyll radicals generated in approximately 75% of the centers. Same spectral conditions as Figure 5-10.....	149
Figure 5-15a: EPR spectrum of Sr ²⁺ substituted g=4.1 signal in partially hydrated RCC sample. Spectral conditions same as Figure 5-13.....	150
Figure 5-15b: EPR spectrum of NH ₃ substituted g=4.1 signal in partially hydrated RCC sample. Spectral conditions same as Figure 5-13.....	151
Figure 5-16 a) top and b) bottom. LI-FTIR difference spectrum of the S ₂ Q _A -/S ₁ Q _A state. reaction center cores, 200K illumination. 6500 scans total. Red spectrum is dark/dark for noise reference.....	153
Figure 5-17a) top and b) bottom. (black)LI-FTIR spectrum of tris treated reaction center cores, 200K.(red-dash) O ₂ evolving RCCs (Figure 5-16). Tris-spectrum average of 12 samples, 6000 scans. 200 K.....	154
Figure 5-18a) top, and b) bottom.(black) LI-FTIR spectrum of NH ₂ OH treated RCCs (manganese depleted), 200K, 6000 scans. (red-dash) O ₂ evolving samples (Figure 5-16).....	155
Figure 5-19a) top, and b) bottom. (black) LI-FTIR spectrum of RCCs soaked in ¹⁸ O-labeled buffer. 6000 scans, 200K. (red-dash) O ₂ evolving RCCs (Figure 5-16).....	156

Figure 5-20a)

Figure 5-21a)

Figure 5-22 a)

Figure 5-23:a)

Figure 5-24:

Figure 5-25:

Figure 5-20a) top, and b) bottom. (black) LI-FTIR spectrum of RCCs turned over in presence of ^{18}O -labeled buffer. 6000 scans, 200K. (red-dash) O_2 evolving RCCs (Figure 5-16).....	157
Figure 5-21a) top and b) bottom. (black) LI-FTIR difference spectrum of NH_3 treated RCCs. (g=4.1 conditions) 3000 scans. (red-dash) O_2 evolving RCCs (Figure 5-16).....	159
Figure 5-22 a) top and b) bottom. LI-FTIR difference spectra of Sr^{2+} substituted RCCs (g=4.1) conditions. 4000 scans. (red-dash) O_2 evolving RCCs (Figure 5-16).....	160
Figure 5-23:a) top 800-600 cm^{-1} range of LI-FTIR difference spectrum of tris-washed and O_2 evolving RCC samples. 5000 scans (tris washed) and 6500 scans (O_2 evolving) respectively b) 800-600 cm^{-1} range of NH_2OH and O_2 evolving RCCs. 4000 scans (NH_2OH) and 6500 scans (O_2 evolving)....	172
Figure 5-24: 800-600 cm^{-1} range of LI-FTIR spectrum of RCCs allowed to turnover in presence of ^{18}O labeled water. (red-dash) O_2 evolving RCCs (Figure 5-16).....	175
Figure 5-25: 800-600 cm^{-1} range of LI-FTIR spectrum of Sr^{2+} substituted RCCs. LI-FTIR spectrum of O_2 evolving samples shown for reference.....	177

Abstract

Vibrat
and the bond
various vibr
structure of
vibrational
techniques.
description
systems wi
smaller mol
sample con
fragility of
pieces of v
problems o
spectroscop
spectroscop

CHAPTER 1

INTRODUCTION TO VIBRATIONAL SPECTROSCOPY OF BIOLOGICAL SYSTEMS

Abstract

Vibrational spectroscopy provides a direct probe of the geometrical environment and the bonding interactions of a molecular system. One can use the data acquired from various vibrational spectroscopic studies and draw detailed conclusions about the structure of the site under investigation. The two primary methods of acquiring vibrational data from molecules are infrared and Raman spectroscopies. These techniques, when used in conjunction with one another, can provide a nearly complete description of the vibrational behavior of the system. However the study of biological systems with vibrational spectroscopy has, until recently, lagged behind studies of smaller molecules that used these techniques. This is due to issues arising from the lower sample concentrations typically achievable with biological samples, as well as the relative fragility of the samples being studied. In this dissertation are presented several different pieces of work that demonstrate the utility of vibrational spectroscopy when applied to problems of biological relevance. These projects are presented in the order of increasing spectroscopic and technical complexity, and show that biological vibrational spectroscopy can lend important insight to mechanistic and structural questions.

Vi

the

sp

abl

is r

sev

of r

the

org

enz

rang

sens

betw

can

quar

Cou

infra

the j

have

mana

Vibrational Spectroscopy of Biological Systems:

Vibrational spectroscopy of biomolecules is a field that has seen much progress in the last twenty years. With the readily accessible technology of lasers, and the widespread acceptance of Fourier-Transform spectroscopies, vibrational studies have been able to shed light on many difficult problems of biological relevance.

A challenge facing all biological spectroscopists relates to signal-to-noise ratios. It is not uncommon for a biological vibrational spectroscopist to desire information about several vibrations in a molecule that may have thousands, tens of thousands or hundreds of thousands normal modes of vibration. Often times we wish to seek information about the active site of a metallo-protein, or look for changes in the vibrational spectra of an organic cofactor, or look directly at a single redox-active amino acid in an enzyme. With enzymes easily reaching molecular weights in the several hundred-thousand Dalton range, it is necessary to have the ability to *detect* these small signals with commensurate sensitivity, while at the same time having methods whereby one can *discriminate* between those signals of interest and the remaining (3N-6) signals that constitute what can be an overwhelming background signal. New developments in the fields of solid-state quantum detectors for the infrared region of the electromagnetic spectrum and Charge-Coupled Device (CCD) type detectors for the visible region have been of great use for infrared and Raman spectroscopists. These technical developments in conjunction with the judicious use of isotopic labeling and reaction modulated difference spectroscopies have made the issues of signal detection and signal discrimination much more manageable.

While

utility in ma

properties of

investigator

of the particu

Infrared Sp

Infran

molecular sy

energy differ

If we

harmonic osc

(1) $\Psi(x,t)$

then at time =

that describes

that describes

places all of

transition bet

of the coeffic

expression th

Ψ_0 to Ψ_1 is re

$\frac{d(c \cdot t)}{d}$

(2)

While both Raman spectroscopy and infrared spectroscopy have proven their utility in many different biological contexts, they are sometimes limited by the specific properties of the individual enzyme being studied. The choice as to which techniques an investigator will utilize for a given biological system depends upon the optical properties of the particular sample.

Infrared Spectroscopy

Infrared spectroscopy[1] is a technique whereby vibrational transitions in a molecular system are induced by the application of light of energy that matches the energy difference between the ground and first excited vibrational states of the system.

If we assume that the total vibrational wave function, $\Psi(x,t)$, of a simple diatomic harmonic oscillator can be described with a two state equation.

$$(1) \quad \Psi(x,t) = c_0 \Psi_0(x,t) + c_1 \Psi_1(x,t)$$

then at time = 0, we will assume that $c_1 = 0$ and $c_0 = 1$, where $\Psi_0(x,t)$ is the wave function that describes the system in its ground vibrational state, and $\Psi_1(x,t)$ is the wave function that describes the system in the first excited vibrational state. This assumption, in effect, places all of the oscillators in their ground vibrational state, Ψ_0 . In order to induce a transition between the two states we need to provide a mechanism that changes the values of the coefficients c_0 and c_1 . If we apply radiation in order to induce a transition, then the expression that represents the probability of the system undergoing a transition from Ψ_0 to Ψ_1 is represented by the transition moment integral

$$(2) \quad \frac{d(c_1^* c_1)}{dt} \propto \epsilon_0^2 M_{01}^2$$

where c_i repres

c_i^* is the comp

$$(3) \quad M_{01} =$$

where

$$(4) \quad ex =$$

represents the

on the particle.

that is independ

transition integ

$$M_{01} =$$

In this case th

functions. In c

x. In other wo

along a vibra

spectrum.

Raman Spec

Rama

inelastically

scattered lig

molecule is p

proportional

where c_1 represents the coefficient of the first excited vibrational state Ψ_1 , in equation (1), c_1^* is the complex conjugate of c_1 and M_{01} is the transition moment integral

$$(3) \quad M_{01} = \int_{-\infty}^{\infty} ex \psi_1^* \psi_0 dx$$

where

$$(4) \quad ex = \mu$$

represents the dipole moment operator of the molecule. In these equations e is the charge on the particle, and x is the displacement along the x -axis of the particle. If μ is a constant that is independent of the vibration of a molecule, then it would factor out of the above transition integral equation, giving

$$M_{01} = \mu \int_{-\infty}^{\infty} \psi_1^* \psi_0 dx$$

In this case the transition integral would vanish, as ψ_0 and ψ_1 are by definition orthogonal functions. In order that the transition integral be non-zero, μ must change as a function of x . In other words, the dipole moment of the molecule must change as the atoms displace along a vibrational coordinate in order to observe that vibrational mode in the infrared spectrum.

Raman Spectroscopy

Raman spectroscopy is a technique whereby incident light is scattered inelastically from molecules. The energy difference between the incident light and the scattered light is equal to the energy of a vibrational transition of the molecule. If a molecule is placed in an electric field then a dipole will be induced in the molecule that is proportional to the applied electric field.

$$\mu_{\text{ind}}$$

where α , the

If an electric

$$\epsilon =$$

is applied to

$$\mu_{\text{ind}}$$

Assuming the

of the molec

polarizability

$$\alpha = e$$

where α_0 is

polarizability

displacement

for the induc

$$\mu_{\text{ind}}$$

With the sub

$$\cos \theta$$

the expression

$$\mu_{\text{ind}}$$

This equation

$v-v_0$ and $v-v_0$

$$\mu_{\text{induced}} = \alpha \varepsilon$$

where α , the proportionality constant, is also known as the polarizability of the molecule.

If an electric field

$$\varepsilon = \varepsilon_0 \cos 2\pi \nu t$$

is applied to a molecule, then the induced dipole can be represented as

$$\mu_{\text{ind}} = \alpha \varepsilon_0 \cos 2\pi \nu t$$

Assuming that the polarizability, α , is a property that changes as the internal coordinates of the molecule change, then we can represent the polarizability in terms of a static polarizability α_0 , and a varying part, $\Delta\alpha$.

$$\alpha = \alpha_0 + (\Delta\alpha) \cos 2\pi \nu_0 t$$

where α_0 is the equilibrium polarizability, $\Delta\alpha$ is the maximum deviation of the polarizability from the equilibrium value, and ν_0 is the vibrational frequency of the displacement. If we use this factored representation of the polarizability in the expression for the induced dipole, the result is

$$\mu_{\text{ind}} = [\alpha_0 + (\Delta\alpha) \cos 2\pi \nu_0 t] [\varepsilon_0 \cos 2\pi \nu t]$$

With the substitution

$$\cos \theta \cos \phi = \left(\frac{1}{2} \right) [\cos(\theta + \phi) + \cos(\theta - \phi)]$$

the expression for the induced dipole becomes

$$\mu_{\text{ind}} = \alpha_0 \varepsilon_0 \cos 2\pi \nu t + \frac{1}{2} \Delta\alpha \varepsilon_0 [\cos 2\pi(\nu + \nu_0)t + \cos 2\pi(\nu - \nu_0)t]$$

This equation predicts that the induced dipole moment will oscillate at frequencies ν , $\nu + \nu_0$ and $\nu - \nu_0$. The oscillating electric dipole then radiates electromagnetic radiation of

the same fre

non-zero va

incident rad

the vibration

a vibration.

intense, mon

the vibration

samples with

source. In or

passed throu

years. lasers

already high.

spectrometer

collection op

which is the

detected po

spectroscopy.

of the form

$$P =$$

where α is :

the same frequencies, ν , $\nu-\nu_0$ and $\nu+\nu_0$. Thus a vibration (with frequency ν_0) that causes a non-zero value for $\Delta\alpha$ scatters incident radiation at 1) the same frequency, ν , as the incident radiation (Rayleigh scattering), 2) at the incident frequency minus the energy of the vibration, $\nu-\nu_0$, (Stokes radiation), and 3) at the incident frequency plus the energy of a vibration, $\nu+\nu_0$, (anti-Stokes radiation). The advent of laser technologies to provide intense, monochromatic radiation, has made Raman spectroscopy an invaluable tool for the vibrational study of molecular systems.

Early forms of Raman spectroscopy were performed by illuminating samples with single wavelengths of light that originated from a high intensity white light source. In order to select the single wavelengths of light, the white light continuum was passed through a grating, and then the dispersed light was passed to the sample. In recent years, lasers have made the experiment much easier as they readily provide very intense, already highly monochromatic beams of light. See Figure 1-1 for a schematic of a Raman spectrometer system. The scattering from the sample is collected with the appropriate collection optics, then passed to a monochromator which disperses the scattered light which is then detected with a photomultiplier tube one wavelength at a time, or it is detected polychromatically with a CCD-type detector. Analogous to infrared spectroscopy, the probability of Raman transitions is determined by a probability integral of the form

$$P = \int_{-\infty}^{\infty} \psi_1^* \hat{\alpha} \psi_0 dx$$

where α is the polarizability operator for the molecule. If a transition is to be Raman

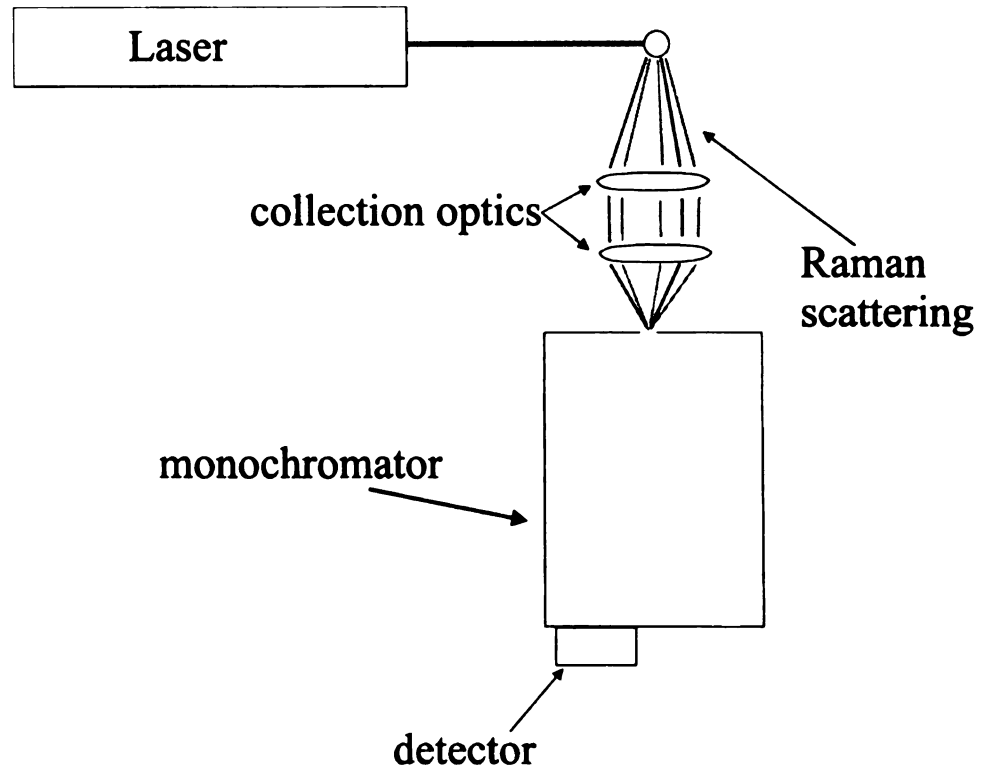


Figure 1-1: Schematic of Raman scattering spectrometer.

active, the

the molecu

If th

the sample.

scattering a

that is as m

is observed

correspond

scattering is

following eq

$$(\alpha_{\rho\sigma}$$

g_i and f_i

electronic sta

resonance te

provides a s

radiation, ν_0

initial and ex

are approxim

However, wh

equal, then a

active, the transition from ψ_0 to ψ_1 must induce a change in the overall polarizability of the molecule.

If the light incident on the sample has the same energy as an optical transition of the sample, then vibrations that are coupled to that optical transition will exhibit Raman scattering at much higher intensities. This intensity enhancement can result in scattering that is as much as 10^3 - 10^4 greater than the scattering from the same vibrational mode that is observed in an experiment in which the energy of the incident light does not correspond to an optical transition. The term that governs the intensity of Raman scattering is $(\alpha_{\rho\sigma})_k$, the polarizability tensor component for the transition k. In the following equation

$$(\alpha_{\rho\sigma})_k = \frac{1}{\hbar} \sum_r \left[\frac{\langle f | M_\rho | r \rangle \langle r | M_\sigma | g \rangle}{\nu_r - \nu_g - \nu_0 + i\Gamma_r} + \frac{\langle f | M_\sigma | r \rangle \langle r | M_\rho | g \rangle}{\nu_r - \nu_f + \nu_0 + i\Gamma_r} \right]$$

$|g\rangle$ and $|f\rangle$ are the initial and final states of the molecule, and $|r\rangle$ is the excited electronic state from which scattering occurs. The first term of this equation is called the *resonance* term. The second is a nonresonant term that, under conditions of resonance, provides a small contribution to the overall signal. When the frequency of the incident radiation, ν_0 is significantly different from the difference in the frequencies between the initial and excited states, $\nu_r - \nu_g$, then the first and second terms of the above equation are approximately equal in their contribution to the overall scattering phenomenon. However, when the incident energy and the energy difference $\nu_r - \nu_g$ are approximately equal, then as the denominator of the first term goes to zero, the first term dominates the

scattering process. The result is a greatly increased change in the polarizability, which results in a large increase in scattering efficiency.

The *resonance Raman* effect has been used widely in the spectra of heme proteins and other metalloproteins[2] that exhibit intense absorption in the visible region of the electromagnetic spectrum. In these systems, Raman scattering that arises from the active site of the enzyme have been observed by using small ligands that exhibit characteristic vibrational signals, isotopic labeling, and site-directed mutagenesis. However, in systems that have cofactors or pigments that exhibit high extinction coefficients, yet where the signals of interest are not coupled to the optical transitions of those cofactors, one must be careful to use an excitation wavelength that avoids regions of any pigment absorbance. Failure to do this will result in spectra that are dominated by cofactor scattering, and scattering from the species of interest will be difficult to detect. Photosynthetic systems are such an example. The light harvesting apparatus of photosynthetic systems is designed to absorb incident light efficiently. Over millennia, the pigments utilized to perform the primary light harvesting role have developed absorption spectra that, while characterized by certain absorption maxima, display significant absorption throughout the visible region of light. As a result, Raman scattering from photosynthetic samples contain vibrational modes from the pigment bed, and any signals arising from molecules in the enzyme that are not themselves efficient absorbers of light are expected to be negligible relative to the more intense resonance enhanced vibrations of the chlorin pigments.

In systems where both infrared absorption and Raman scattering spectroscopies can be utilized, the spectroscopist has the luxury of being able to obtain a relatively complete picture of the vibrational properties of the system being studied. Both of these

techniques

vibrational

transition

dipole moment

for Raman

elements of

contains the

transition

this symmetry

spectrum

infrared spectrum

spectrum

spectroscopy

picture of

A

for the study

displays the

Raman scattering

technique

where the

in cases in

transitions

techniques depend upon non-zero values of their respective transition integrals for a vibrational transition to be observable. The only difference between the respective transition integrals lies in the operators upon which the phenomena rely, namely, the dipole moment operator, $\hat{\mu}$, in the case of infrared, and the polarizability operator, $\hat{\alpha}$, for Raman spectroscopy. If the triple product of the symmetry of Ψ_1 , the symmetry elements of the dipole moment or polarizability operator, and the symmetry of Ψ_0 , contains the totally symmetric irreducible representation of the point group then the transition integral will have a non-zero value, and thus will be observable. As a result of this symmetry dependence, it is possible to obtain vibrational data from the Raman spectrum of a system that is not observable in the infrared spectrum. Likewise, the infrared spectrum frequently may contain data that are not observable in the Raman spectrum of the same molecule. Therefore, if it is possible to perform both forms of spectroscopy on a given system, the data obtained will usually present a more complete picture of the vibrations of the system than if one of the techniques is used exclusively.

A significant advantage that Raman spectroscopy has over infrared spectroscopy for the study of biological molecules relates to the water content of the samples. Water displays strong absorbances throughout the mid-infrared spectrum (Figure 1-1). The Raman scattering from water however is fairly weak, which makes Raman scattering the technique of choice for investigating the vibrational properties of biological systems where the presence of water is necessary to ensure biological activity and relevance. But in cases in which the vibrational signals of interest are not coupled to the electronic transitions of a highly absorbing chromophore, and such chromophores are in fact

present, infrared
are not limited
able to examine
from enzymes
challenges need

Fourier Tran

It was
specific function
infrared light
developed into
absorption spectra
and accuracy of
experiments
spectrometers
which separate
then sent through
time. The difference
absorbed as radiation
spectrum, the
continuous medium
it was not until

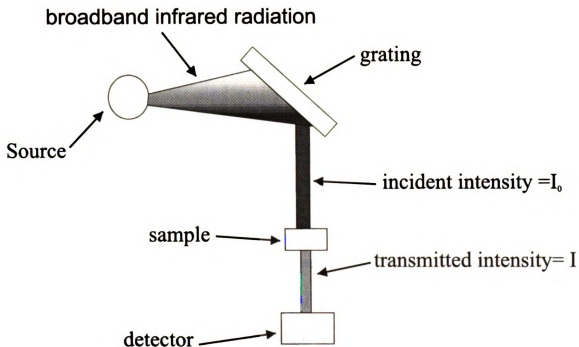
present, infrared spectroscopy must be the technique of choice. Infrared spectroscopists are not limited to samples that contain strongly absorbing chromophores, and thus are able to examine a wider range of enzymatic samples. However in order to gather data from enzymes with infrared spectroscopy, several daunting technical and biochemical challenges need to be addressed.

Fourier Transform Infrared (FTIR) Spectroscopy:

It was first reported in 1882 that a correlation existed between the presence of specific functional groups in a molecule and the absorption of specific frequencies of infrared light [3]. However, it was not until 1903 that modern IR spectroscopy was developed into the form in which it is currently used. W.W. Coblentz investigated the IR absorption spectrum of hundreds of inorganic and organic substances[4] and the precision and accuracy of his work allows many of these spectra to still be considered useful. These experiments and subsequent experiments until the mid 1960's relied on infrared spectrometers that consisted of a source of infrared radiation and a dispersive grating which separated the light into its constituent wavelengths (see Figure 1-2). This light is then sent through the sample and each wavelength is detected one resolution unit at a time. The difference between the incident and the transmitted light is the light that is absorbed as result of vibrational activity in the sample. In order to acquire the complete spectrum, the dispersive grating is scanned, changing the frequency of the light in a continuous manner, until the complete infrared absorption spectrum is obtained. However it was not until the advent of Fourier-Transform infrared spectroscopy that it was possible

broa

Source



$$\text{transmittance} = \frac{I}{I_0}$$

Figure 1-2: Schematic of scanning infrared spectrometer

to apply infrared spectroscopy to biological systems routinely. The inherent advantages offered by this technique allow spectra with sufficient signal-to-noise ratios to be acquired in an acceptably short amount of time.

FTIR spectroscopy is a technique that is based upon the principle of interferometry which allows a continuum of radiation to be convoluted in to a single signal that is detected instantaneously. This signal, which contains all of the spectral information, is then deconvoluted through the use of a Fourier transformation. This instantaneous detection of all of the frequency components lends certain distinct advantages in the signal-to-noise ratio of the acquired spectrum. Many FTIR spectrometers are based upon the Michelson interferometer (Figure 1-3). This is an interferometer that consists of a moving mirror and a fixed mirror that is held perpendicular to the displacement vector of the moving mirror. Bisecting the angle between the two mirrors is a beamsplitter which is assumed to be ideal, i.e. it transmits 50% of the incident light and reflects 50% of the incident light. To illustrate how this system works, we will first consider a beam of monochromatic radiation[5]. When the beam of radiation strikes the beamsplitter, 50% of this light is reflected to the stationary mirror and 50% of the light is transmitted to the moving mirror. If the center of the beamsplitter is designated point X, and the centers of the moving mirror and the fixed mirrors are points Y and Z respectively, then the difference between the distances that the beams of light must follow are $2(XY-XZ)$. This difference is called the *retardation*, δ . An assumption that is made in this treatment is that the incident radiation, while not

infrar
light fr
source

beams

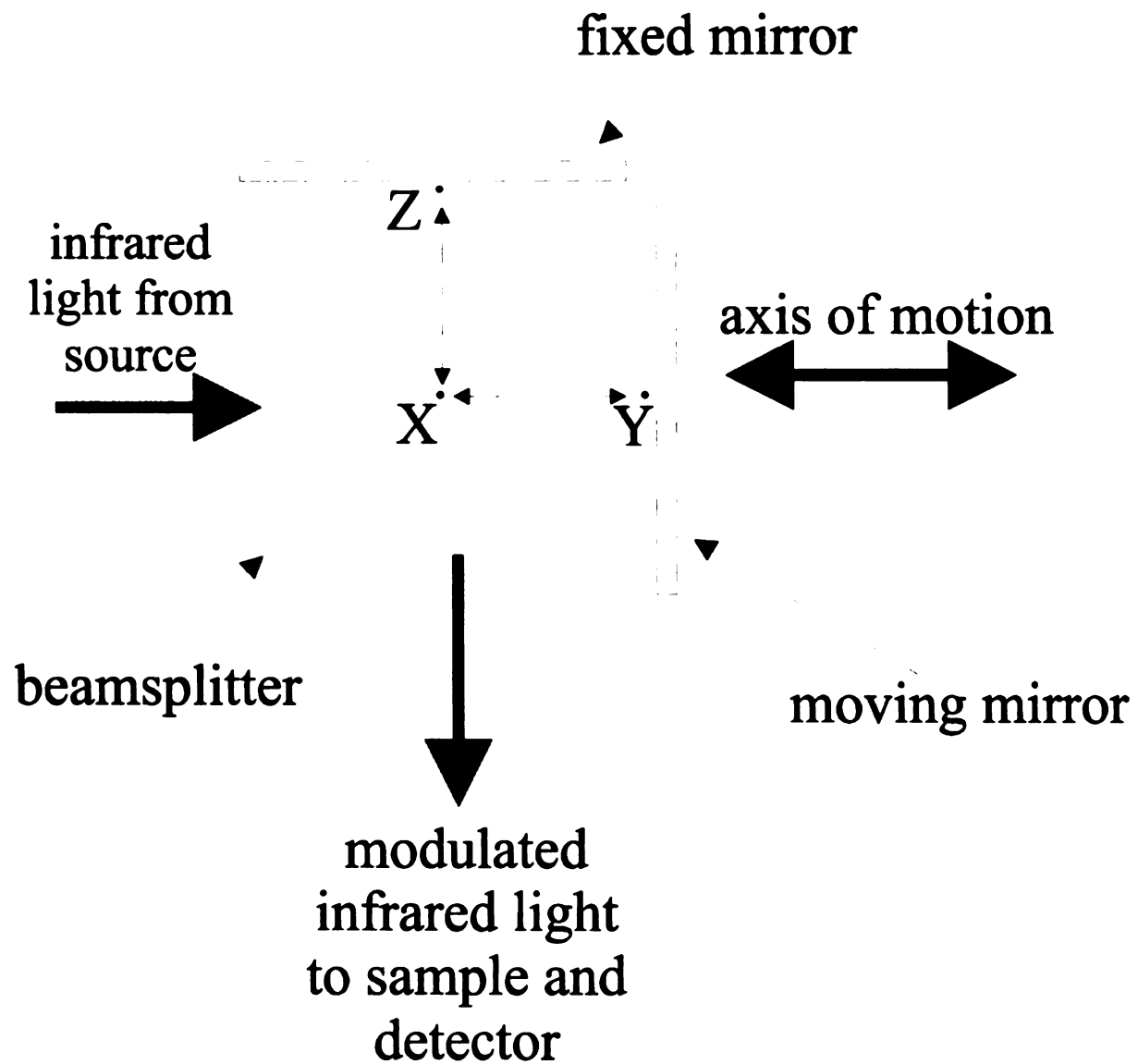


Figure 1-3: Schematic of Michelson Interferometer

necessarily in

mirrors are e

recombined w

incident ener

mirror is disp

radiation, whe

at the detecto

pathlength is

the detected e

energy equals

at zero displa

utilize a phot

moving mirro

velocity, the

signal being

that is an inte

At intermedia

$I'(\delta)$

This signal c

energy of the

It is this mo

necessarily infinitely narrow, is, at a minimum, collimated. When the fixed and moving mirrors are equidistant from the beamsplitter ($2(XY-XZ)=0$) then the radiation, once recombined will remain perfectly in phase and will constructively interfere. All of the incident energy will thus be passed through to the detector. However, if the moving mirror is displaced by a distance $\frac{1}{4}\lambda$, (hence the difference in pathlength is $\frac{1}{2}\lambda$) then the radiation, when recombined, will destructively interfere and no energy will be observed at the detector. If the moving mirror is displaced by $\frac{1}{2}\lambda$ then the total difference in pathlength is λ . The result is that the waves will once again constructively interfere, and the detected energy will be equal to the incident energy. In the case for which the incident energy equals the detected energy, it is not possible to determine if the moving mirror is at zero displacement or some multiple of $\frac{1}{2}\lambda$. In practice, however, FTIR instruments utilize a photoelectric sensor circuit to determine the starting and stopping point of the moving mirror, thus eliminating this problem. When the mirror is scanned at constant velocity, the detected signal will be seen to vary sinusoidally, with the maximum of this signal being detected each time the moving mirror passes through a displacement value that is an integral multiple of $\frac{1}{2}\lambda$ (so the total displacement δ is an integral multiple of λ). At intermediate values of δ , the intensity of the signal is given by

$$I'(\delta) = 0.5I(\bar{\nu}) \left\{ 1 + \cos 2\pi \frac{\delta}{\lambda} \right\} = 0.5I(\bar{\nu}) \{ 1 + \cos 2\pi \bar{\nu} \delta \}$$

This signal consists of two parts, a constant, steady-state component equal to one-half the energy of the incident radiation, and a modulated component equal to $0.5I(\bar{\nu})\cos 2\pi \bar{\nu} \delta$. It is this modulated component that is referred to as the *interferogram*. In reality, a

"perfect" beam

sensitive detector

necessary to

observed at the

$H(\bar{v})$ in the

$I(\delta)$

We can compare

beam spectrum

$I(\delta)$

Mathematical

calculated

the interference

$I(\delta)$

The other

E

The spectrum

more detailed

Signal-to

For

terms of

“perfect” beamsplitter is not possible. Additionally, perfectly reflecting optics, infinitely sensitive detectors and noise free electronics are also not feasible. With this in mind, it is necessary to incorporate these realities into the expression for the intensity of radiation observed at the detector. We must include a wavenumber dependent “reality” coefficient $H(\bar{\nu})$ in the expression for the signal intensity.

$$I(\delta) = 0.5I(\bar{\nu})H(\bar{\nu})\cos 2\pi \bar{\nu} \delta$$

We can combine the two terms $I(\bar{\nu})H(\bar{\nu})$ into one $B(\bar{\nu})$ which we will call the single beam spectral intensity function. With this, the expression for the interferogram becomes

$$I(\delta) = B(\bar{\nu})\cos 2\pi \bar{\nu} \delta$$

Mathematically, $I(\delta)$ is the cosine Fourier transform of $B(\bar{\nu})$ and the actual spectrum is calculated by cosine Fourier transforming $I(\delta)$. When a polychromatic source is utilized, the interferogram can be represented by an integral of the form

$$I(\delta) = \int_{-\infty}^{+\infty} B(\bar{\nu})\cos 2\pi \bar{\nu} \delta \cdot d\bar{\nu}$$

The other half of the Fourier transform pair is

$$B(\nu) = \int_{-\infty}^{+\infty} I(\delta)\cos 2\pi \bar{\nu} \delta \cdot d\delta$$

The spectrum is, as before, computed from this half of the Fourier-transform pair. For a more detailed description of the data treatment methods, see[5].

Signal-to-noise considerations in FTIR

Fourier transform infrared spectroscopy maintains several distinct advantages, in terms of signal-to-noise ratios, over conventional dispersive infrared experiments. These

adv.

tool

adv.

syst

Four

when

spe

when

the

of t

Bec

sam

adv.

of t

Four

whil

advantages are what has allowed biological infrared spectroscopy to become a promising tool for the investigation of enzymatic structure/function determination. The first of these advantages relates to the enhanced throughput achievable with interferometer based systems, and is known as Jacquinot's Advantage[5]. The maximum throughput of a Fourier spectrometer is

$$\Theta_I = 2\pi A^I \frac{\Delta \bar{\nu}}{\bar{\nu}_{\max}} \text{cm}^2 \text{sr}$$

where A^I is the area of the reflective surfaces. The analogous expression for grating spectrometers is

$$\Theta_G = \frac{h A^G \Delta \bar{\nu}}{f a \bar{\nu}^2} \text{cm}^2 \text{sr}$$

where A^G is the area of the grating, f is the focal length of the collimating mirrors, h is the slit height and a is the grating constant. If one compares the throughput advantages of the Fourier transform instrument relative to that of the grating instrument, one obtains

$$\frac{\Theta_I}{\Theta_G} = \frac{2\pi A^I f a \bar{\nu}^2}{A^G h \bar{\nu}_{\max}}$$

Because of the $\bar{\nu}^2$ (where $\bar{\nu}$ is the frequency of light being used to interrogate the sample) dependence it is clear that Fourier transform spectroscopies have large advantages in throughput over comparable grating spectrometer-based systems.

Another advantage of Fourier transform spectroscopies relates to the fact that all of the wavelength components of a given spectral range are examined simultaneously. Fourier spectrometers detect all of the wavelength components of light simultaneously, while conventional scanning spectrometers require the grating to be moved each time a

different wavelength of light is to be detected. Because this movement of the grating takes time, the Fourier instrument is able to acquire the complete spectrum in the same amount of time that the scanning instrument is able to scan a fraction of the same region of the spectrum. Because the signal-to-noise ratio of a spectrum is proportional to the square root of the time spent gathering the signal, this multiplexing allows much higher signal-to-noise ratios to be achieved in a given amount of time. This advantage, called the multiplex or Fellgett's advantage, is another key aspect of Fourier spectroscopies, and it is another reason that infrared spectroscopy has only recently become useful for studying samples of biological origin[5].

The first two chapters of this dissertation show how FTIR spectroscopy in conjunction with Raman spectroscopy can provide critical insight into the structure and function of two very different systems. The first system examined is a series of model compounds that represent the cyanide-ligated form of the oxidized binuclear center of the respiratory enzyme cytochrome *c* oxidase. FTIR spectroscopy was utilized in this study in a technically simple way, but when the infrared and Raman data were combined and analyzed by using sophisticated vibrational analysis techniques, key insights into how cyanide may be bound in the enzyme emerged. In chapter three, somewhat more technically challenging FTIR measurements were performed, again in conjunction with Raman spectroscopy, to analyze the binding mode of carbon monoxide to the enzyme soluble guanylate cyclase (sGC). In chapters four, five, and six we have extended FTIR spectroscopy to its technical limits in an effort to elucidate structural and mechanistic aspects of photosynthetic water oxidation. These studies introduce the concept of *reaction modulated* infrared difference spectroscopy and represent one of the most technically

challenging FTIR experiments currently being performed. We have developed new methods whereby we can examine the low frequency region of the infrared spectrum, where the vibrations of possible intermediates in the water oxidation process and where the vibrations of the manganese containing active site of the reaction center will be observed. This technique provides an entirely new genre of information regarding how plants and cyanobacteria oxidize water. The techniques developed here will allow us to also extend this type of spectroscopy to other enzymatic systems. Many other metalloproteins will exhibit vibrations in the low frequency region of their infrared spectrum. These vibrations, as in photosystem II, may contain information regarding substrate binding, active site structure, as well as information regarding the catalytic mechanism. With these techniques, this information is now accessible.

1. Ha
Yc
2. Sp
Sp
3. A
4. C
W
5. C
I

LIST OF REFERENCES

1. Harris, D.C. and Bertolucci, M.D., Symmetry and Spectroscopy. 1978, New York: Dover Publications.
2. Spiro, T.G., Biological Applications of Resonance Raman Spectroscopy, ed. T.G. Spiro. Vol. 3. 1988, New York: Wiley.
3. Abney, W.d.W. and Festing, E.R., Phil. Transactions, 1882. **172**: p. 887.
4. Coblentz, W.W., Investigations of Infrared Spectra, 1905, Carnegie Institute: Washington, D.C.
5. Griffiths, P.R. and de Haseth, J.A., Fourier Transform Infrared Spectrometry. 1986, New York: Wiley-Interscience.

Al

wh

res

spe

dep

mas

resp

assi

vibr

labe

of is

vibra

mode

reson

CHAPTER 2

VIBRATIONAL ANALYSIS OF A MOLECULAR HEME-COPPER ASSEMBLY WITH A NEARLY LINEAR Fe^{III}-CN-Cu^I BRIDGE: INSIGHT INTO CYANIDE BINDING TO FULLY OXIDIZED CYTOCHROME C OXIDASE

Abstract

The complete vibrational analysis of [(1-MeIm)Fe(OEP)-CN-Cu(Me₆tren)]²⁺ (1), which has been constructed as a model for the cyanide-ligated binuclear center in the respiratory protein cytochrome *c* oxidase, has been carried out. The resonance Raman spectra ($\lambda_{\text{exc}} = 647$ nm) and the mid-infrared spectra display three cyanide isotope dependent vibrational modes. Two vibrational frequencies decreased with increasing mass of the cyanide ligand (2182-2137-2146-2101 cm⁻¹ and 535-526-526-520 cm⁻¹, respectively, for the ¹²C¹⁴N-¹³C¹⁴N-¹²C¹⁵N-¹³C¹⁵N isotopomers), and could thus be assigned to the C≡N and Fe-CN-Cu stretching vibrations, respectively. The third vibration, detected with resonance Raman, exhibited frequencies more sensitive to ¹³C labeling of the cyanide ligand than with ¹⁵N labeling (495-487-493-485 cm⁻¹ with the set of isotopomers above). This pattern of isotopic dependence is characteristic of a bending vibration. Additionally, with the same laser excitation frequency, the C≡N stretching mode was observed, which is the first time that this vibration has been detected in the resonance Raman spectrum of a synthetic heme-cyanide complex. The normal coordinate

at

co

m

m

cy

co

lig

ar

lik

tra

In

tra

rec

pro

is n

cry

ins

dist

bac

spec

have

analysis showed marked differences between bridged and unbridged heme-cyanide complexes. Internal coordinates that are orthogonal in unbridged systems are significantly mixed in the bridged model, despite the overall linearity of the Fe-CN-Cu moiety. These measurements strengthen the proposal that cyanide bridges the two metal atoms in the cyanide-ligated, oxidized binuclear center of cytochrome *c* oxidase. A quantitative consideration of the vibrational characteristics of cyanide bound to the resting enzyme in light of our model compound results strongly suggests that the binuclear center is flexible and can undergo structural rearrangement to accommodate exogenous ligands. This is likely to be of mechanistic importance in both dioxygen reduction and proton translocation.

Introduction

Cytochrome *c* oxidase is the terminal electron acceptor in the respiratory electron transfer chain of prokaryotic and eukaryotic organisms. This membrane-bound enzyme reduces molecular oxygen to water and utilizes the resultant gain in free energy to pump protons across the cell membrane [1-6]. The active site of this enzyme, at which oxygen is reduced to water, consists of a binuclear Cu₂/heme *a*₃ center. The recent solution of the crystal structures[7, 8] of cytochrome *c* oxidase from two sources has provided new insight into the arrangement and structure of the binuclear center of the enzyme. The distance between the two metals is 4.5 Å in the resting bovine enzyme[7] and 5.2 Å in the bacterial system[8]. The close proximity of the two metals had been deduced from earlier spectroscopic, biochemical, and molecular biological studies and a number of models have been advanced for their function in both O₂ reduction and in the redox-coupled

translocation of protons. A central issue is the extent to which the partially reduced dioxygen substrate interacts with the two metals. At the peroxide level in the reaction sequence, for example, a range of structures, from a μ -peroxo fully covalent linkage to a terminal hydroperoxo (Fe-O-O-H) with minimal interaction between the Cu_B and the heme a₃ moiety, has been proposed[1-4].

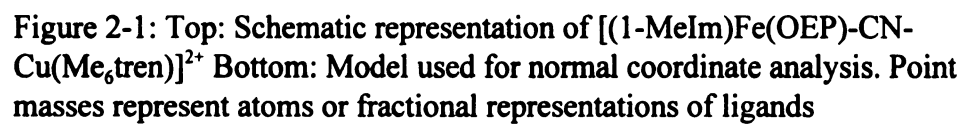
Cyanide, a potent inhibitor of oxidase activity, has often been used as an alternate ligand to the heme of the binuclear center[9-14] and can provide insight into the modes by which small molecules bind. The Soret band in the optical spectrum of heme a₃ shifts upon cyanide ligation as the heme iron undergoes a high-spin to low-spin transition. This shift in the optical and magnetic properties of the site has formed the basis for a variety of optical, electron paramagnetic resonance, magnetic-circular dichroism and magnetic susceptibility studies of the CN⁻ ligated enzyme[1-4]. A further useful spectroscopic probe is the C \equiv N stretching vibration[15], which is characterized by a strong, sharp absorption around 2030-2200cm⁻¹. This has allowed the use of infrared spectroscopy to study the interactions of bound CN⁻ in the binuclear center[9-14]. Although the prevailing view of the mode of cyanide binding in the fully oxidized enzyme invokes a bridging conformation[9], models have been advanced that postulate monodentate binding[10]. If cyanide does, in fact, bind in a bridging configuration, the vibrational behavior of the ligand in terms of its geometry remains to be elucidated. These are questions that can be addressed through careful vibrational spectroscopic analysis, isotopic labeling, normal coordinate analysis, and model compound studies.

A series of
been prepared
cytochrome c oxidase
Melm), L is a
coordinate Cu(II)
molecular bridge
characterized by
porphyrin (≤ 0.1)
invariant bond length
dependent on the
investigation of
Melm)Fe(OEP)-
Figure 2-1. The
from the closely
axial ligands is
which, with the
invariant over the
because of the presence
and the simplification
enzyme[19-21].
 $\text{Cu}(\text{Me}_6\text{tren})^{2+}$ to
bridging oxo[23].

A series of molecules of the general type [(N-base)Fe^{III}(OEP)-CN-Cu^{II}LL'] have been prepared as analogues of the cyanide-bound binuclear center of oxidized cytochrome *c* oxidases[16-18]. Here the N-base is pyridine or 1-methylimidazole (1-MeIm), L is a tridentate or tetradentate polyamine ligand bound to four- or five-coordinate Cu(II) and L' is a unidentate anion, when present. A number of these molecular bridged assemblies have been structurally defined by crystallography. They are characterized by a six-coordinate low-spin Fe(III) atom in the mean plane of the porphyrin (≤ 0.1 Å displacement), an essentially linear Fe-C \equiv N group (176-180°) of invariant bond lengths, variable Cu-N distances (1.88-2.17 Å), Cu-N-C angles (147-174°) dependent on ligand L, and Fe---Cu separations of 4.93-5.11 Å. For this initial investigation of the vibrational properties of Fe-CN-Cu bridges we have examined [(1-MeIm)Fe(OEP)-CN-Cu(Me₆tren)]²⁺ (**1**) [18], whose structure is presented schematically in Figure 2-1. The structure of this complex has not been determined; structural data are from the closely related molecule with a pyridine axial ligand[18]. This difference in axial ligands is expected to have a negligible effect on the Fe-CN-Cu bridge parameters which, with the exception of the Cu-N bond length and the Cu-N-C angle, are essentially invariant over some six structures. The imidazole-ligated bridge assembly was chosen because of the presence of a proximal imidazole at heme a₃ in the binuclear center[7, 8] and the simplifying feature of the nearly linear bridge. As in the cyanide-inhibited enzyme[19-21], the metal spins are ferromagnetically coupled in [(py)Fe(OEP)-CN-Cu(Me₆tren)]²⁺ to afford an integer spin ground state[22]. Analogous assemblies with bridging oxo[23, 24] and hydroxo[25] groups have been prepared and structurally

Im

Figure
Cu(Me
masses



characterized. The

enzyme. These

cyanide coordinat

of the binuclear

In the w

spectroscopies to

used the vibratio

metal ligand con

refined set of fo

well as possible

details of cyanic

Materials and

The co

from R.H. Hol

equimolar [Cu

[Fe(OEP)(OC

several volum

violet needles

Raman spectr

stream of col

with dry KBr

characterized. Their magnetic properties are similar to those of the oxidized resting enzyme. These bridged assemblies, being structurally proven examples of bidentate cyanide coordination of a type possible in the enzyme, can lend insight into the structure of the binuclear center of the cyanide-inhibited protein.

In the work reported here, we have applied resonance Raman and infrared spectroscopies to **1** and varied the isotopic composition of the cyanide ligand. We then used the vibrational data to carry out a normal coordinate analysis[26] of the binuclear metal/ligand core of the complex. The calculated potential energy distributions and the refined set of force constants give insight into the nature of the bonding interactions as well as possible non-bonding, or steric constraints. The results are used to probe the details of cyanide ligation to resting cytochrome *c* oxidase.

Materials and Methods

The compound $[(1\text{-MeIm})\text{Fe}(\text{OEP})\text{-CN-Cu}(\text{Me}_6\text{tren})](\text{ClO}_4)_2$ (**1**) was obtained from R.H. Holm and co-workers at Harvard University. It was prepared by the reaction of equimolar $[\text{Cu}(\text{Me}_6\text{tren})(\text{CN})](\text{ClO}_4)$ [18] (containing the desired cyanide isotopomer), $[\text{Fe}(\text{OEP})(\text{OClO}_3)]$, and 1-methylimidazole in acetone solution, followed by diffusion of several volume equivalents of ether over several days. The product separated as dark violet needles. $[(1\text{-MeIm})\text{Fe}(\text{OEP})\text{CN}]$ (**2**) was synthesized as described[18]. Resonance Raman spectra were obtained with solid state samples, cooled to -80 °C in a dewar by a stream of cold dinitrogen gas. The samples were prepared by grinding the compounds with dry KBr powder and pressing to form a pellet. To obtain Raman spectra, a Coherent

Kr laser

on to the

dispersed

cooled C

were acq

nitrogen

DTGS de

were coa

functions

N

formalism

modificat

vibration

(1) C

where **G**

of its inte

and nonb

is the free

is a non-

appropriat

In

kinetic and

Kr⁺ laser (Coherent K-90) was used for excitation at 647 nm. The laser light was focused on to the sample with an incident power of 30 mW. Resonance Raman scattering was dispersed with a Spex 1877 Triplemate spectrometer and detected by a liquid nitrogen cooled CCD detector (EG&G OMA 4, model 1530-CUV-1024S). Mid-infrared spectra were acquired on a Nicolet 520P FTIR spectrometer, equipped with a DTGS or liquid-nitrogen cooled MCT-B detector, or a Nicolet IR-40 FTIR spectrometer equipped with a DTGS detector. The samples were prepared as CsI pellets. Double sided interferograms were coadded at a resolution of 2 cm⁻¹ and apodized with Happ-Ganzel apodization functions.

Normal coordinate analysis was performed by using the Wilson GF matrix formalism[26]. All calculations were performed on VAX/VMS systems, using a modification of the Shimanouchi program[27]. The GF matrix method of interpreting vibrational spectra consists of constructing and solving the secular equation

$$(1) \quad |\mathbf{GF} - \mathbf{E}\lambda| = 0$$

where **G** is the matrix that describes the geometry of the molecule being studied in terms of its internal coordinates, **F** is the matrix of force constants used to represent the bonding and nonbonding interactions between the atoms of the system, **E** is the unit matrix and λ is the frequency of the vibration in question. The construction of such a secular equation is a non-trivial task that has been greatly facilitated by the use of computers and appropriate programs designed for just such a purpose.

In order to perform a normal coordinate analysis, one must calculate both the kinetic and potential energy functions for the molecule being studied[28]. In terms of the

norm

mole

(2)

(where

(3)

where

matrix

cartesi

system

energy

(4)

and

(5)

where T is

matrix of

force con

diatomic;

because the

and z axes

intuitively in

normal coordinates of a molecule we will define the kinetic and potential energies of a molecule as

$$(2) \quad 2T = \sum_i \dot{Q}_i^2 \quad \text{and} \quad 2V = \sum_i \lambda_i Q_i^2$$

(where $i = 1$ to $3N-6$). In matrix form, these expressions are

$$(3) \quad 2T = \underline{\dot{Q}}' \underline{\dot{Q}} \quad \text{and} \quad 2V = \underline{Q}' \underline{\lambda} \underline{Q}$$

where \underline{Q} is the column vector of the normal coordinates, $\dot{Q} = \frac{dQ_i}{dt}$, and $\underline{\lambda}$ is the diagonal matrix of λ values. It is more convenient, however, to construct a molecule within a cartesian coordinate system initially, as the atomic positions within this coordinate system are easy to interpret. In this case the expressions for the kinetic and potential energy functions of a molecule are quite simple and easily recognizable

$$(4) \quad 2T = \underline{\dot{X}}' \underline{M} \underline{\dot{X}}$$

and

$$(5) \quad 2V = \underline{X}' \underline{F^x} \underline{X}$$

where T is the kinetic energy of the system, V is the potential energy, \underline{M} is a diagonal matrix of the masses of the constituent atoms and $\underline{F^x}$ is a non-diagonal matrix of the force constants between the atoms. The molecule treated here is assumed to be a diatomic; expanding this treatment into three dimensions is straightforward. However, because the modes of vibration of a molecule are combinations of motions along the x , y , and z axes of the Cartesian coordinate system, this matrix of force constants is not as intuitively interpretable as if the molecule and its force constants were described in terms

v

2

m

t

me

(9)

of bond stretches and angular bending motions. To make the force constant matrix as intuitive as possible, it is necessary to convert from an external frame of reference to an internal description of the molecule. This is accomplished by developing a set of internal coordinates for the molecule such that

$$(6) \quad 2T = \underline{\dot{R}}' \underline{K} \underline{\dot{R}}$$

and

$$(7) \quad 2V = \underline{R}' \underline{F} \underline{R}$$

where \underline{R} is the column matrix of the internal coordinates and \underline{K} and \underline{F} are the kinetic and potential energy matrices respectively. Internal coordinates can be thought of as coordinates that are unaffected by rotational or translational motions of the entire molecule. These internal coordinates obey the relation

$$(8) \quad R_t = \sum_{i=1}^{3N} B_{ti} X_i \quad t = 1, 2, 3, \dots, 3N - 6$$

where the coefficients B_{ti} are determined by the geometry of the molecule. Both the \underline{K} and the \underline{F} matrices, in the context of the internal coordinates, are non-diagonal, but the \underline{F} matrix can now be thought of in terms of primary and interaction force constants. With this strategy in place, we merely need to evaluate the respective contributions of the kinetic and potential energies in terms of the internal coordinates in order to arrive at the solution to the vibrational problem.

The momentum of a diatomic molecule can be expressed in terms of a column matrix

$$(9) \quad \underline{P_x} = \underline{M} \underline{\dot{X}}$$

Likew

and m

(10)

Note

mome

transfo

(11)

where

coordin

(12)

and

(13) $\underline{\dot{R}}$

From equa

(14) \underline{M}

Solving for

(15) \underline{R}

Substituting

(16) $2T$

We can now

(17) $\underline{G} =$

Likewise, the kinetic energy of the molecule can be thought of as functions of the mass and momentum of the system

$$(10) \quad 2T = \underline{\underline{P'_x M^{-1} P_x}}$$

Note the similarity to the standard expression for kinetic energy $T = \frac{1}{2}mv^2$. The momentum matrix can be also expressed in terms of the internal coordinates, via the transformation matrix B

$$(11) \quad \underline{\underline{P_x}} = \underline{\underline{B' P}}$$

where the B matrix defines the internal coordinates, R, in terms of the cartesian coordinates of the system, or,

$$(12) \quad \underline{\underline{R}} = \underline{\underline{B X}}$$

and

$$(13) \quad \underline{\underline{\dot{R}}} = \underline{\underline{B \dot{X}}}$$

From equations (9) and (11), we get

$$(14) \quad \underline{\underline{M \dot{X}}} = \underline{\underline{B' P}}$$

Solving for \dot{X} , and inserting the result into (13) gives us

$$(15) \quad \underline{\underline{\dot{R}}} = \underline{\underline{B M^{-1} B' P}}$$

Substituting equation (11) into (10) we can rewrite the kinetic energy expression as

$$(16) \quad 2T = \underline{\underline{P' B M^{-1} B' P}}$$

We can now define the G matrix as

$$(17) \quad \underline{\underline{G}} = \underline{\underline{B M^{-1} B'}}$$

Using this we can

$$(18) \quad 2T = \underline{\underline{P'Q}}$$

Using equations

$$\dot{R} = \underline{\underline{GP}}$$

or

$$\underline{\underline{P}} = \underline{\underline{G^{-1}\dot{R}}}$$

Therefore we can

$$2T = \underline{\underline{P'Q}}$$

$$= \underline{\underline{(G^{-1}\dot{R})'Q}}$$

$$= \underline{\underline{\dot{R}'G^{-1}Q}}$$

When we compare

$$(19) \quad \underline{\underline{K}} = \underline{\underline{G^{-1}}}$$

This result shows

coordinates. In

the vibrational

must define a transformation

$$(18) \quad \underline{\underline{R}} = \underline{\underline{LQ}}$$

This allows us

this transformation

coordinates. Take

definition for the

$$(19) \quad 2V = \underline{\underline{R'Q}}$$

Using this we can rewrite (16) as

$$(18) \quad 2T = \underline{\underline{P'GP}}$$

Using equations (17) and (15), we can now write

$$\dot{R} = \underline{\underline{GP}}$$

or

$$\underline{\underline{P}} = \underline{\underline{G^{-1}\dot{R}}}$$

Therefore we can express the kinetic energy in these terms

$$\begin{aligned} 2T &= \underline{\underline{P'GP}} \\ &= (\underline{\underline{G^{-1}\dot{R}}})' \underline{\underline{G}} (\underline{\underline{G^{-1}\dot{R}}}) \\ &= \underline{\underline{\dot{R}'G^{-1}\dot{R}}} \end{aligned}$$

When we compare this last result to equation (6) we can see that

$$(19) \quad \underline{\underline{K}} = \underline{\underline{G^{-1}}}$$

This result shows that we can express the kinetic energy in terms of the internal coordinates. In order to derive the secular equation that we must solve in order to solve the vibrational problem, and thus determine the normal coordinates of the molecule, we must define a transformation matrix, $\underline{\underline{L}}$, such that

$$(18) \quad \underline{\underline{R}} = \underline{\underline{LQ}}$$

This allows us to relate the internal coordinates to the normal coordinate Q. As a result of this transformation, we can now define the potential energy in terms of these normal coordinates. Taking the previous expression for the potential energy, and inserting our definition for the normal coordinates we get

$$(19) \quad 2V = \underline{\underline{R'FR}} = (\underline{\underline{LQ}})' \underline{\underline{F}} (\underline{\underline{LQ}}) = \underline{\underline{Q'L'FLQ}}$$

By comparison with the potential energy expression in equation (3) it can be seen that

$$(20) \quad \underline{\underline{L'FL}} = \underline{\underline{\lambda}}$$

With equations (6) and (19), we can now rewrite the kinetic energy term.

$$(21) \quad 2T = \underline{\underline{\dot{R}'KR}} = \underline{\underline{\dot{R}'G^{-1}\dot{R}}} \\ = (\underline{\underline{L\dot{Q}}})' \underline{\underline{G^{-1}}} (\underline{\underline{L\dot{Q}}}) = \underline{\underline{Q'L'G^{-1}L\dot{Q}}}$$

Comparing this equation with the kinetic term in equation (3), one sees that

$$(22) \quad \underline{\underline{L'G^{-1}L}} = \underline{\underline{I}}$$

where I is the identity matrix. Using equation (20) we see

$$(23) \quad \underline{\underline{L'FL}} = \underline{\underline{I\lambda}} = \underline{\underline{L'G^{-1}L\lambda}}$$

Multiplying through on the left by $(\underline{\underline{L'}})^{-1}$ gives us

$$(24) \quad \underline{\underline{FL}} = \underline{\underline{G^{-1}L\lambda}}$$

Left multiplying by G, leaves

$$(25) \quad \underline{\underline{GFL}} = \underline{\underline{L\lambda}}$$

This is the secular equation must be solved for the vibrational problem. Diagonalization of the GF product will yields the diagonal matrix λ , whose diagonal elements are the frequencies of the normal modes of vibration.

The initial set of force constants was based upon the modified quadratic fields found in found in [12] and [29]. The dependence of the calculated vibrational frequencies were evaluated as a function of the various force constants employed. Those force constants that were found to have a negligible effect upon the calculated frequencies were not varied as part of the iterative process. Those force constants found to affect the

calcula

between

each of

Result

UV-Vis

The U

absorpt

absorpt

cyanide

include

absorpt

absorpt

show a

are sho

cyanide

Infrared

In

have fre

of these

frequenc

calculated frequencies were systematically adjusted to achieve the optimal agreement between the calculated frequencies and the experimentally determined frequencies of each of the isotopically labeled species.

Results

UV-Visible Spectroscopy:

The UV-visible spectrum of the title complex (Figure 2-2) is characterized by a Soret absorption maximum at 403 nm, visible bands at 526 and 553 nm and a near ultraviolet absorption at 345 nm. When compared to the absorption spectrum of the unbridged heme cyanide complex **2**, despite general similarity, several differences are notable. These include a small (3 nm) blueshift in the Soret maximum, a slight (3 nm) redshift of the UV absorption, and subtle bandshape differences of the visible peaks[18]. The visible absorption bands of both the bridged binuclear complex and the unbridged heme complex show a trailing edge and small features at approximately 650 nm. These absorption bands are shown below to be important in the context of resonance Raman detection of the cyanide stretching and bending modes of this molecule.

Infrared Spectroscopy:

Infrared and resonance Raman spectra of **1** display three vibrational modes that have frequencies sensitive to isotopic labeling of the cyanide moiety (Table 2-1). The first of these appears at 2182 cm⁻¹ in the mid-IR spectra of the molecule (Figure 2-3). From its frequency and relative intensity, this mode can be assigned to the C≡N stretching

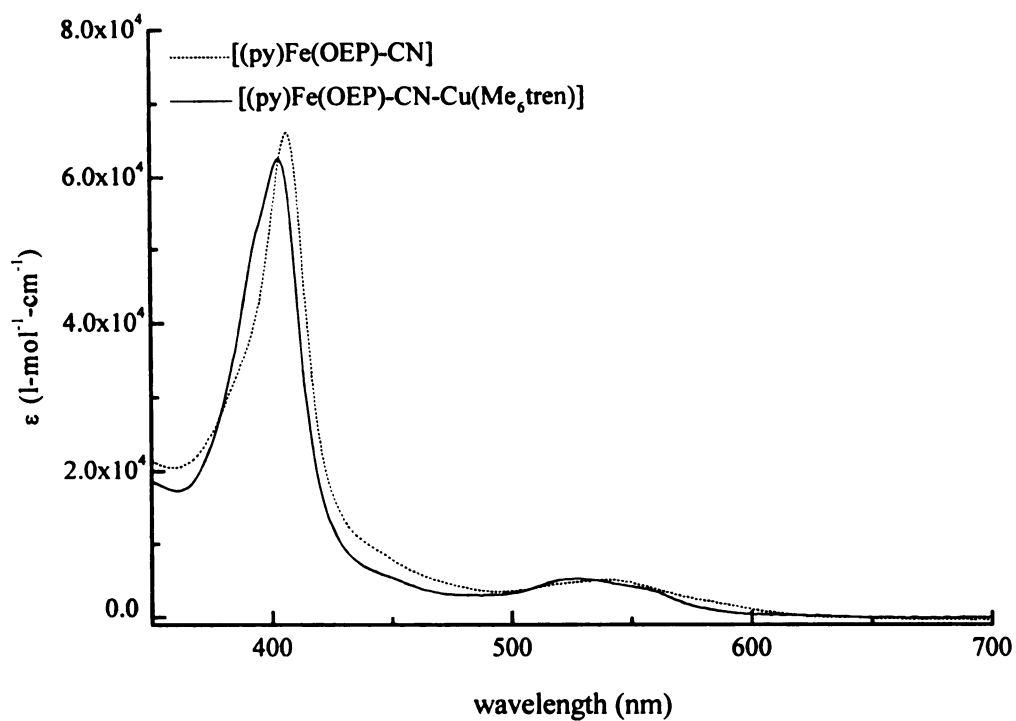


Figure 2-2: UV-Vis absorption spectra of “bridged”, [(py)Fe(OEP)-CN-Cu(Me₆tren)], and “unbridged”, [(py)Fe(OEP)-CN], complexes. Sample concentrations were 2.2 mM (bridged) and 1.9mM (unbridged). Spectra were dissolve in acetone and spectra were recorded in a CaF₂ cell, 50 μ M pathlength.

vibr

vibr

the

ligan

seco

spec

and

stretc

isotop

stretc

comp

the in

are co

compl

determ

eviden

solven

vibration of bound, bidentate cyanide. When the cyanide is substituted with $^{12}\text{C}^{15}\text{N}$ the vibration shifts to 2146 cm^{-1} ; with $^{13}\text{C}^{14}\text{N}$ it shifts to 2137 cm^{-1} and with $^{13}\text{C}^{15}\text{N}$ cyanide the mode appears at 2101 cm^{-1} . This frequency decrease with increasing mass of the ligand is expected for a $\text{C}\equiv\text{N}$ stretching vibration in simple heme-cyanide complexes. The second vibrational mode that displays an isotope dependence appears in the infrared spectrum at 535 cm^{-1} (Figure 2-4). With $^{13}\text{C}^{14}\text{N}$ or $^{12}\text{C}^{15}\text{N}$ the mode appears at 526 cm^{-1} , and with the doubly labeled cyanide the mode shifts to 520 cm^{-1} . As with the $\text{C}\equiv\text{N}$ stretching mode, this absorption displays a mass-dependent decrease in frequency upon isotopic labeling and is assigned to a stretching vibration of the $\text{Fe}-\text{C}\equiv\text{N}-\text{Cu}$ bridge unit.

The extinction coefficients for the infrared absorbances attributable to the $\text{C}\equiv\text{N}$ stretches of **1** and **2** were determined by dissolving known amounts of the crystalline compounds in acetone. Infrared absorption spectra of these solutions were acquired, and the integrated intensity of the cyanide stretching mode absorptions were calculated. These are collected in Table 2-2, along with relevant extinction coefficients from related complexes[30]. The effect of hydrogen bonding on the $\nu_{\text{C}\equiv\text{N}}$ stretching frequency was determined by dissolving **2** in neat methanol. A 3 cm^{-1} shift to higher frequency was evident in methanol, indicating a distal interaction between the hydrogen bond-donating solvent, and the nitrogen atom of the cyanide ligand (see Table 2-3).

Tab

VI

a
samm
region
inform

Table

Fe^{III}-C

Fe^{III}-C

Ru^{III}-C

Ru^{II}-C

Table 2-1 Isotopic Dependence of Vibrational Frequencies^a

VIBRATIONAL MODE	IR/RR DETECTED?	¹² C ¹⁴ N	¹³ C ¹⁴ N	¹² C ¹⁵ N	¹³ C ¹⁵ N
$\nu_{\text{C}\equiv\text{N}}$	IR/RR	2182	2137	2146	2101
ν	IR	535	526	526	520
δ	RR	495	487	493	485

^a samples in solid matrix. (CsI for IR and KBr for RR. CsI facilitated concurrent measurement of Far-IR region.) No isotope dependent modes were found between 200cm⁻¹ and 400 cm⁻¹. See individual spectra for information on specific experimental conditions.

Table 2-2 Extinction Coefficients of Various C≡N Stretches

	$\nu_{\text{C}\equiv\text{N}}(\text{cm}^{-1})$	$\epsilon (\text{M}^{-1} \text{cm}^{-1})$	reference
Fe ^{III} -C≡N	2129	17	this work
Fe ^{III} -C≡N-Cu ^{II}	2182	150	this work
Ru ^{III} -C≡N	2053	~2500	11
Ru ^{II} -C≡N-Ru ^{III}	2118	~50	11

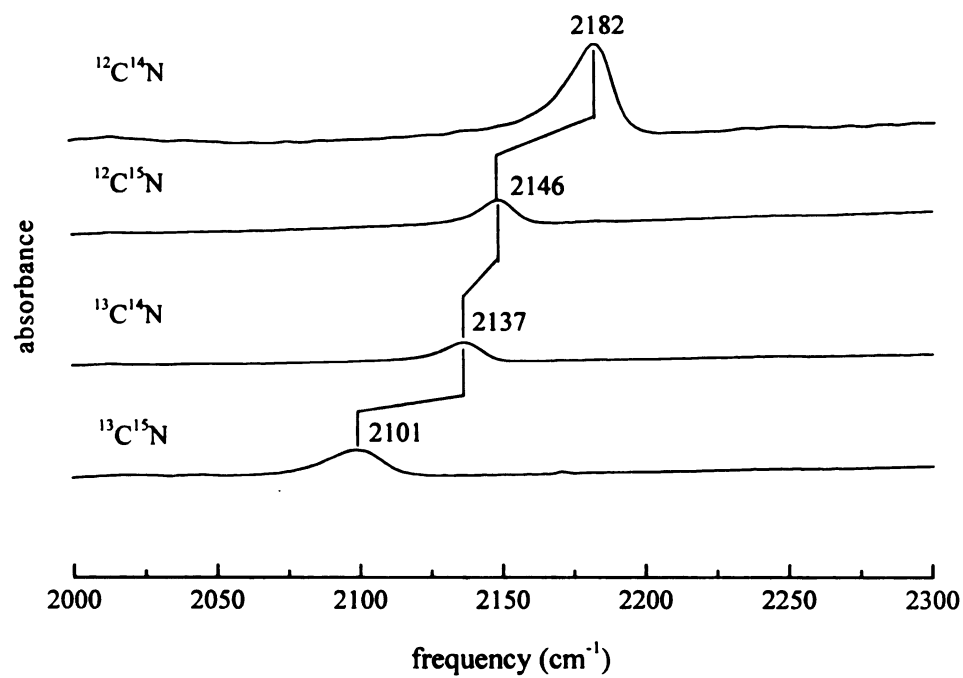


Figure 2-3: FTIR spectrum of $[(1\text{-MeIm})\text{Fe}(\text{OEP})\text{-CN-Cu}(\text{Me}_6\text{tren})]^{2+}$ and isotopomers. Spectral conditions described in Materials and Methods.

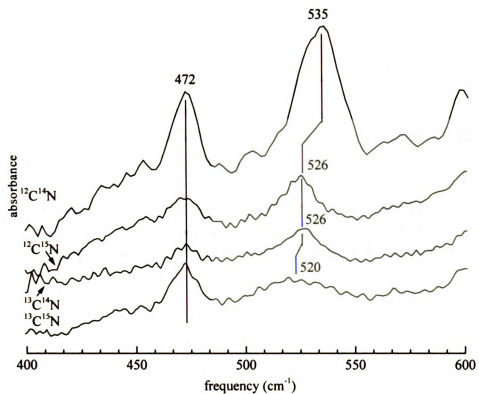


Figure 2-4: FTIR spectrum of $[(1\text{-MeIm})\text{Fe}(\text{OEP})\text{-CN-Cu}(\text{Me}_6\text{tren})]^{2+}$ and isotopomers. Spectral conditions described in Materials and Methods.

Table 2

CN geo

linear

bent

lin

be

^a $\theta = \arctan$

Table 2-3 Vibrational Frequencies for C≡N in Selected Structures

CN geometry/N-terminus interaction	example	ranges of ν_{CN} (cm^{-1})	reference
linear/none	[(1-MeIm)Fe(OEP)(CN)]	2129	this work
bent/none	SP-14 ("strapped-heme")	2118-2130	16
linear/hydrogen-bonded	oxidized HRP, 2 in methanol	2131, 2132	12, this work
bent/hydrogen-bonded	no published examples	-	-
linear/Cu-bonded	1 , Fe-CN-Cu	2140-2182	5, this work
bent/Cu-bonded	Fe-CN-Cu ($\theta < 140\text{-}170^\circ$) ^a	2120-2181	5, this work
-	oxidized cytochrome c oxidase	2146-2152	3

^a θ = angle defined by Cu-N≡C

Resonance

spectrum

Raman

cm^{-1} . W

cyanide

vibrational

ligated

29. 32]

systems

an isot

substitu

$\text{C}\equiv\text{N}$ s

inactive

has no

Vibrat

of 1 a

vibratic

The her

Resonance Raman Spectroscopy:

The third cyanide isotope sensitive vibration of **1** appears in its resonance Raman spectrum. When 647 nm excitation is used, a vibration is present at 495 cm^{-1} in the Raman spectrum (Figure 2-5). In the $^{13}\text{C}^{14}\text{N}$ labeled complex this vibration shifts to 487 cm^{-1} . With $^{12}\text{C}^{15}\text{N}$ the vibrational mode occurs at 493 cm^{-1} and with doubly labeled cyanide this mode shifts to 485 cm^{-1} . This isotopic dependence is diagnostic of a bending vibration of the $\text{Fe-C}\equiv\text{N}$ unit[31]. The observation of heme-ligated cyanide and heme-ligated CO bending modes in enzymatic systems is well preceded in the literature[1-4, 29, 32], however this vibration has not previously been observed in synthetic porphyrin systems[33, 34].

When higher frequency Raman scattering was examined with 647 nm excitation, an isotope sensitive mode was observed at 2182 cm^{-1} (Figure 2-6). Upon isotopic substitution, the shifts correlated with those observed in the infrared spectrum for the $\text{C}\equiv\text{N}$ stretching mode, allowing its assignment as the normally infrared active/Raman inactive $\text{C}\equiv\text{N}$ stretching mode. Resonance Raman detection of the $\text{C}\equiv\text{N}$ stretching mode has no precedent in cyanide-ligated heme systems.

Vibrational Analysis:

Normal coordinate analysis (NCA) was performed to assign the vibrational modes of **1** and to determine the contributions of individual internal coordinates to the vibrational modes of the complex. The model used to represent **1** is shown in Figure 2-1. The heme was represented by four point masses, arranged equatorially around a six-

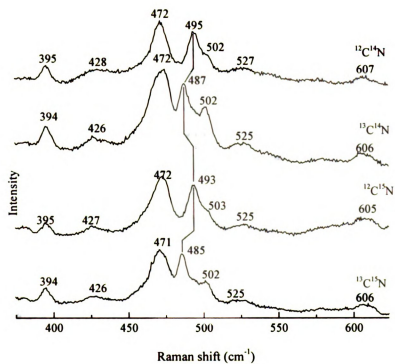


Figure 2-5: Resonance Raman spectrum of [(1-MeIm)Fe(OEP)-CN-Cu(Me₆tren)]²⁺ and isotopomers. Spectral conditions described in Materials and Methods.

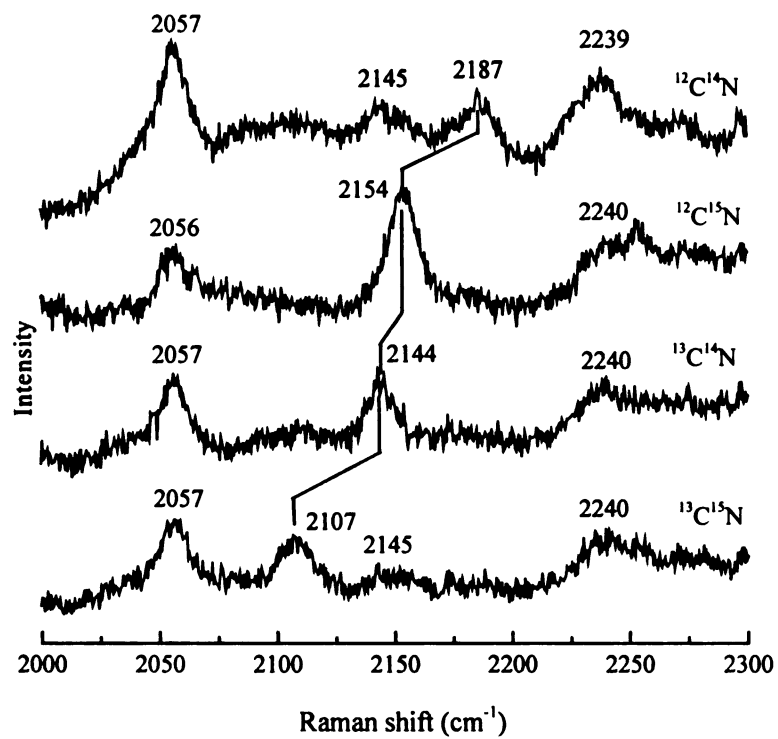


Figure 2-6: Resonance Raman spectrum of $[(1\text{-MeIm})\text{Fe}(\text{OEP})\text{-CN-Cu}(\text{Me}_6\text{tren})]^{2+}$ and isotopomers. Spectral conditions described in Materials and Methods.

coord

were

1-M

the l

obse

fit w

peak

expe

mod

Tab

that

obse

pote

four

of re

with

32-2

and

coordinate iron atom. The four non-cyano ligands to the five-coordinate copper atom were treated as point masses, with each weighing one-fourth of the total ligand mass. The 1-Me-imidazole was also approximated by a point mass representing the total weight of the ligand.

The NCA was performed to find the best set of force constants that duplicated the observed cyanide isotopic shifts of the vibrational frequencies in **1** (Table 2-1). The peaks fit were the infrared observed modes at 2182 cm^{-1} and 535 cm^{-1} , and the observed Raman peak at 495 cm^{-1} . The optimized force field for this molecule is listed in Table 2-4. The experimental and calculated vibrational frequencies for the cyanide isotope sensitive modes, along with the potential energy distributions for these modes, are collected in Table 2-5.

The potential energy distribution (PED) for the 2182 cm^{-1} band (Table 2-5) shows that this mode is comprised entirely of the $\text{C}\equiv\text{N}$ stretching coordinate. The shifts observed are duplicated by a simple, two body harmonic oscillator, further supporting the potential energy distribution calculated in the complete analysis. An interesting result is found for the potential energy distribution of the 535 cm^{-1} peak. This mode is comprised of roughly equal contributions of the Fe-C (35%) and Cu-N (30%) stretching coordinates, with smaller contributions from the $\text{Fe-C}_{\text{CN}}\equiv\text{N}_{\text{CN}}$ bending mode (16%). Earlier results[29, 32-34] indicate that when ligands are bound to hemes in a linear geometry, the stretching and bending modes are orthogonal to each other, with each mode contributing little to the

Tal

Prin

Stre

Fe-C

C₀

Imd

N₀

Fe-3

Cu-

Ben

Fe-C

Cu-

in-p

out-

in-p

out-

Table 2-4 Force Constants for NCA of Fe-CN-Cu system

Primary:		Off-Diagonal	
Stretches:	Value (mdyn/A)	Stretch-stretch:	Value (mdyn/A)
Fe-C _{CN}	1.69	Fe-C _{CN} /C _{CN} -N _{CN}	0.35
C _{CN} -N _{CN}	17.91	Fe-C _{CN} /Cu-N _{CN}	-0.19
Imd-Fe	1.55	Fe-C _{CN} /imd-Fe	0.1
N _{CN} -Cu	1.26	Cu-N _{CN} /C _{CN} -N _{CN}	0.1
Fe-N _{porph}	1.4	C _{CN} -N _{CN} /imd-Fe	0.09
Cu-N _{LIGAND}	1.0	Cu-N _{CN} /Cu-L _{ax}	0.1
Bends:	Value (mdyn-A/rad²)	Stretch-Bend:	Value (mdyn/rad)
Fe-C _{CN} -N _{CN}	0.705	Fe-C _{CN} /Fe-C _{CN} -N _{CN}	0.3
Cu-N _{CN} -C _{CN}	0.19	Fe-C _{CN} /Cu-N _{CN} -C _{CN}	-0.17
in-plane imd-Fe-C _{CN}	0.2	Cu-N _{CN} /Fe-C _{CN} -N _{CN}	0.07
out-plane imd-Fe-C _{CN}	0.2	Cu-N _{CN} /Cu-N _{CN} -C _{CN}	-0.55
in-plane Cu-N _{CN} -C _{CN}	0.2	Bend/Bend	Value (mdyn-A/rad²)
out-plane Cu-N _{CN} -C _{CN}	0.2	Fe-C _{CN} -N _{CN} /Cu-N _{CN} -C _{CN}	0.17

PED o

the str

contrib

constan

mdyn:

(Table

the Fe-

cm⁻¹

Table

exp.
2182
535

495

peak, th

bending

the Cu

on eith

vibration

PED of the other. For 1, however, despite the linear geometry, substantial contribution of the stretching coordinates to the bending modes was observed; conversely the bends contribute significantly to the predominantly stretching modes. The interaction force constant for coupling between the Fe-C stretch and the Cu-N stretch has a value of -0.19 mdyne/Å (Table 2-4). The potential energy distribution (PED) for the 495 cm⁻¹ peak (Table 2-5) shows that this mode is comprised of the Fe-C≡N bending coordinate, (68%), the Fe-C stretch (18%) and the Cu-N≡C (13%) bending mode. As in the case of the 535 cm⁻¹

Table 2-5 Experimental and Calculated Vibrational Frequencies (cm⁻¹)

¹² C ¹⁴ N		¹² C ¹⁵ N		¹³ C ¹⁴ N		¹³ C ¹⁵ N		PED
exp.	Calc.	exp.	Calc.	exp.	Calc.	exp.	Calc.	
2182	2182	2146	2148	2137	2136	2101	2102	99% C _{CN} -N _{CN} stretch
535	535	526	527	526	527	520	519	35% Fe-C _{CN} stretch, 30% N _{CN} -Cu stretch, 19% Fe-C _{CN} -N _{CN} bend
495	496	493	492	487	487	485	483	68% Fe-C _{CN} -N _{CN} bend, 18% Fe-C _{CN} stretch, 13% Cu-N _{CN} -C _{CN} bend

peak, there is an appreciable contribution of the stretching coordinate to what is overall a bending vibration. A series of control calculations demonstrated that substantially varying the Cu/non-cyanide ligand or the Fe/porphyrin force constants did not have a large effect on either the frequency or the potential energy distribution of the isotope sensitive vibrational modes

DISCUSSION

Electronic Structure and Vibrational Characteristics:

The vibrational properties of **1** were investigated with the use of isotopically labeled cyanide. To understand the bonding nature of cyanide, one must have a clear picture of the electronic structure of this ligand. When cyanide is bound to a metal porphyrin system, the cyanide ligand binds preferentially via the carbon end and acts as a σ -donor, lowering the electron density in its $5\sigma^*$ highest-occupied molecular orbital, which is antibonding[35]. Consequently a terminally bound cyanide moiety generally has a higher $\text{C}\equiv\text{N}$ stretching frequency than does free cyanide. This is in contrast to the isoelectronic example of carbon monoxide, which acts preferentially as a π -acceptor and is a poor σ -donor. When terminally bound, it readily accepts electron density into its $2\pi^*$ orbital, which lowers the $\text{C}\equiv\text{O}$ vibrational frequency relative to free CO.

When cyanide acts as a bidentate ligand, forming units of the type $\text{M}-\text{C}\equiv\text{N}-\text{M}'$, $\nu_{\text{C}\equiv\text{N}}$ will further increase, and the metal-ligand stretching frequency will decrease[35-37]. This can be rationalized with simple molecular orbital arguments. Introducing a bonding interaction at the nitrogen atom of the bound cyanide will deplete electron density in the molecular orbital carrying the electron density at that end of the molecule. This orbital is an overall σ^* antibonding orbital and depleting electron density leads to a higher overall $\text{C}\equiv\text{N}$ stretching force constant. Another prediction made by the molecular orbital argument is that the M-CN bond will be weaker in a bridging geometry. However, in the case of the bridged system presented here, the vibration attributed to the metal-cyanide stretching mode appears at a significantly *higher* frequency, 535 cm^{-1} , than that of the

corresp

observa

of the

for the

corresp

between

the unt

in stre

followi

Norma

compo

have i

vibrati

mode

ligand

cyanof

comple

howeve

angle),

coordin

corresponding unbridged system, 2, whose Fe-CN vibration appears at 450 cm^{-1} [33, 34]. This observation can be rationalized by examining the force constants and the resulting PED of the normal coordinate analysis (Tables 2-4 and 2-5). It is seen that the force constant for the Fe-C stretch is indeed lower (1.69 mdyn/\AA) than that found in studies of the corresponding unbridged system ($\sim 2.01\text{ mdyn/\AA}$)[33, 34], indicating a weaker interaction between the iron and the carbon end of the cyanide ligand in the bridged as compared to the unbridged systems. The basis for this paradoxical behavior, *i.e.* an observed increase in stretching frequency despite a lower stretching force constant, is discussed in the following section.

Normal Mode Composition:

Previous studies have undertaken careful analyses of the normal mode compositions of the vibrational frequencies of heme/cyanide complexes. These studies have identified characteristic interdependencies for certain bending and stretching vibrations. For example, there is little or no interaction between the Fe-C \equiv N bending mode and the orthogonal Fe-C stretching internal coordinate in systems in which the ligand binding is parallel to the normal of the heme plane. An example of this is cyanoferroc horseradish peroxidase[29] in which the cyanide binds linearly. For this complex, the stretch/bend (S/B) interaction force constant is small, 0.079 mdyn/rad . In 1, however, in which the ligand binds in an analogous, almost linear, fashion (179° Fe-C \equiv N angle), an appreciable interaction force constant (IFC) of 0.3 mdyn/rad between these two coordinates is necessary to maintain the relative ordering of the bending and stretching

m

or

va

th

ap

0.

str

ba

int

Va

the

po

ne

W

fun

ran

the

stre

val

diff

of

expe

modes. The effect of changing the value of this interaction force constant on the relative ordering of the bending and stretching vibrations is shown in Figure 2-7. At vanishing values of this interaction force constant, the stretching mode is higher in frequency than the bending mode. As the IFC value is increased, the bending and stretching modes approach each other, then cross at a value of ~ 0.42 mdyn/rad. At values for the IFC above 0.42 mdyn/rad the bending mode is predicted to be higher in frequency than the stretching mode. The value that best reproduces the observed bending and stretching bands at 495 cm^{-1} and 535 cm^{-1} respectively, is 0.30 mdyn/rad. The value of the interaction force constant also affects the mode composition of the two normal modes. Values for the IFC of approximately 0.3-0.6 mdyn/rad increase the amount of mixing of the Fe-C \equiv N bending coordinate with the Fe-C stretching coordinate. At values near the point where the ordering of the bending and stretching modes switch (0.42 mdyn/rad), neither mode exhibits the isotopic dependence characteristic of a bending vibration.

When the bending and stretching mode compositions and frequencies were examined as a function of the Cu-N/Cu-N \equiv C stretch/bend IFC, similar behavior at the limits of the range examined was observed (Figure 2-8). However, instead of the modes switching their ordering around a specific value for the IFC, they diverge, maintaining the stretching mode at a higher frequency than the bending mode. There are two possible values for this IFC, -0.55 mdyn/rad and -0.30 mdyn/rad, that give the observed frequency difference between the bending and stretching modes. Only with the more negative value of -0.55 mdyn/rad however, did the absolute frequencies for the two modes match the experimentally observed frequencies.

frequency (cm⁻¹)

580
560
540
520
500
480
460
440
420

Figur
Fe-C

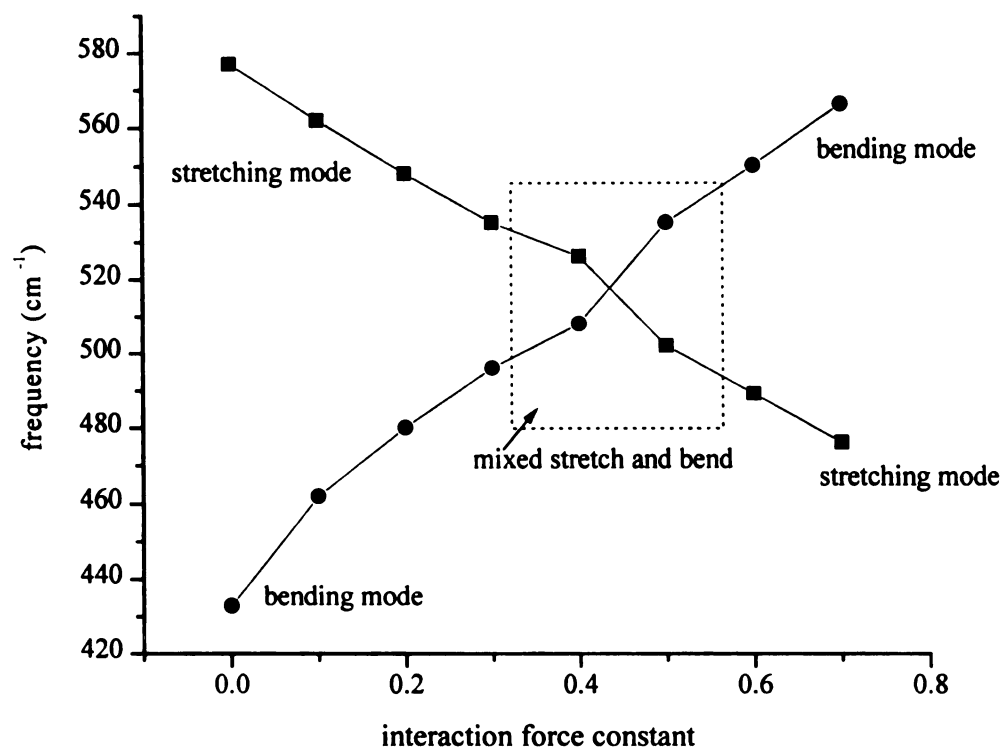
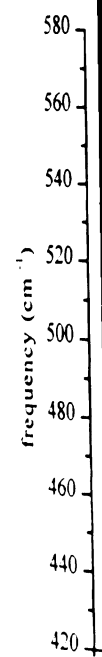


Figure 2-7: Plot of calculated vibrational frequencies versus Fe-C stretching/Fe-C-N bending interaction force constant.



Figur
Cu-N

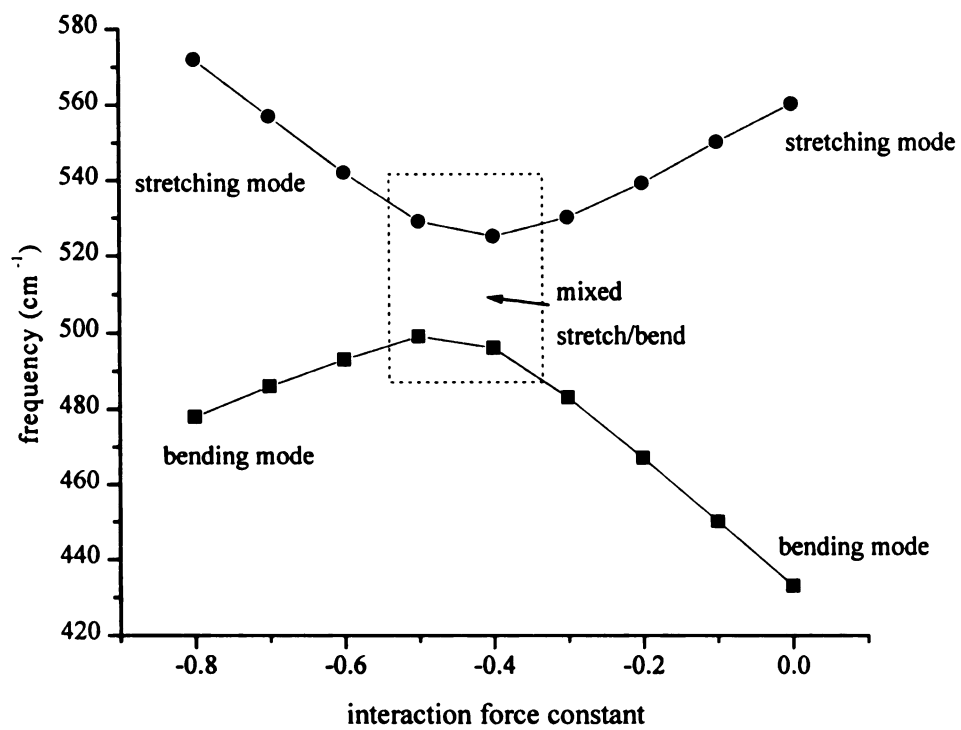


Figure 2-8: Plot of calculated vibrational frequencies versus Cu-N stretching/Cu-N-C bending interaction force constant

In cy
bending coord
constant. Addi
the relative lin
According to t
produce a stre
observed here
force constant.
constants are l

Resonance En

In this
the resonance
with laser exc
isotope-depen
have been sho
the $C\equiv N$ vibr
band with c
spectrum. Th
that an anal
absorption sj

In cyanoferroc myeloperoxidase[29], the ordering of the ν_1 stretching and the bending coordinates is strongly dependent upon the choice of the Fe-C stretching force constant. Additionally, the relative splitting of these modes was found to correlate with the relative linearity of the ligand. In **1**, the Fe-C \equiv N angle is approximately 179°[18]. According to the trends discussed in previous work[29, 32], this linear geometry would produce a stretching frequency higher than that of the bend, which is, in fact what is observed here for **1**. The higher stretching frequency is not due to an increased stretching force constant, but rather to a coupling of two stretches, where the two individual force constants are lower than those in unbridged complexes.

Resonance Enhancement Conditions

In this work, the normally infrared active C \equiv N stretching vibration is observed in the resonance Raman spectrum of this complex when $\lambda_{\text{ex}} = 647$ nm. Measurements made with laser excitation in resonance with the π, π^* transitions did not exhibit any cyanide isotope-dependent modes. In carbon monoxide bound systems, distal steric constraints have been shown to influence the Raman/IR activity of the C \equiv O stretch[31]. The fact that the C \equiv N vibration is observed with red excitation indicates the presence of an absorption band with charge transfer character in the red region of the electronic absorption spectrum. The failure to observe $\nu_{\text{C}\equiv\text{N}}$ in the red excitation Raman spectrum of **2** indicates *that* an analogous CT band is apparently not present in this wavelength range in the *absorption* spectrum of the unbridged complex. This suggests that copper in the model

complex and

significant rol

Relevance to

The q

the binuclear

possibility h

hydrogen-bo

neighboring

the ν_{C-N} of 2

and other lin

Cyan

feric heme

exhibited by

of steric on

correspond

Chang et al

geometry, t

The trend i

exhibited b

allowed to

horseradish

complex and, by implication, Cu_b in the heme/copper terminal oxidases, plays a significant role in defining the electronic structure of the binuclear center.

Relevance to Cytochrome c Oxidase

The question remains as to whether cyanide covalently bridges the two metals of the binuclear center in cyanide treated, fully-oxidized terminal oxidases. An alternative possibility has been raised by Caughey and coworkers[10] that invokes a strong hydrogen-bonding interaction between the N-terminus of the cyanide ligand and a neighboring amino acid residue in the distal pocket. These models are based partly upon the $\nu_{\text{C}\equiv\text{N}}$ of 2146-2151 cm⁻¹ observed in the cyanide inhibited enzyme[9, 10, 13, 14]. This and other lines of evidence need to be considered when evaluating these possibilities.

Cyanide, when not subject to steric or electronic perturbations, prefers to bind to ferric hemes in a linear fashion. An example of this situation is **2**. The $\nu_{\text{C}\equiv\text{N}}$ frequency exhibited by this linear system is 2129 cm⁻¹. When the cyanide ligand is forced, by virtue of steric or electronic constraints, to adopt a non-linear binding geometry, the $\nu_{\text{C}\equiv\text{N}}$ is correspondingly lower, as seen in the hindered, strapped heme system developed by Chang et al[38]. The $\nu_{\text{C}\equiv\text{N}}$ for these systems ranges from 2130 cm⁻¹ for a linear binding geometry, to 2118 cm⁻¹ for a CN ligand with a Fe-C≡N binding angle of 130° (Table 2-3). **The trend** is that linear cyanide groups have higher C≡N stretching frequencies than those **exhibited** by non-linear systems. When the terminal nitrogen of a linear cyanide group is **allowed** to interact with an electron acceptor, $\nu_{\text{C}\equiv\text{N}}$ increases. For example, in oxidized *horseradish* peroxidase, in which groups capable of donating hydrogen bonds are present

in the ligand binding pocket, $\nu_{\text{C}\equiv\text{N}}$ occurs at 2131 cm^{-1} (Table 2-3). When **2** is dissolved in methanol, a hydrogen bond donor, the $\nu_{\text{C}\equiv\text{N}}$ shows a small (3 cm^{-1}), but discernible, upshift in value (Table 2-3). This shift is attributed to a hydrogen bonding interaction between the solvent and the N-terminal end of the CN ligand. In complexes that are both non-linear *and* have the N-terminus interacting with an electron acceptor (such as a hydrogen bond donor or a copper ion), a range of $\nu_{\text{C}\equiv\text{N}}$ values is displayed. These frequencies are convolutions of both the specific binding angle and the N-terminus interaction.

As shown in Table 2-3, the only systems whose $\nu_{\text{C}\equiv\text{N}}$ values bracket that observed in cyanide-treated cytochrome *c* oxidase are those with a copper(II) ion coordinated to the N-terminus of the cyanide ligand. These models are characterized by a relatively linear Fe-C \equiv N geometry, and varying angles at which the Cu(II) ion is coordinated to the N-terminus of the cyanide ligand. The model complex studied here presents one example of essentially linear (176°) Fe-C \equiv N and C \equiv N-Cu (174°) binding angles. The $\nu_{\text{C}\equiv\text{N}}$ observed in this case is 2182 cm^{-1} . Clearly, the observed value of $\nu_{\text{C}\equiv\text{N}}$ in cyanide-treated cytochrome oxidase necessitates invoking more than a simple distal hydrogen bond *and* a relatively linear binding geometry to rationalize the relatively high observed frequency *for* this vibration in the enzyme. We conclude that the vibrational analysis presented here *provides* strong evidence for a bridging structure in the cyanide complex of oxidized **cytochrome** oxidase.

It has been suggested that the intensity of the C \equiv N stretch in bridging complexes *is significantly* lower than the C \equiv N stretch in unbridged systems[14]. Because of this

apparent trend

oxidase were t

weakened by t

in scope and c

the C≡N stre

solutions. It c

much lower

However, in t

stretch is sig

Therefore, arg

upon the inter

An in

has emerged

heme a_3 plan

distances for

structure to

138°. From

distance of

cytochrome

of ~2.1 Å a

displaced fr

which requi

apparent trend, it was argued that the $C\equiv N$ stretching bands observed in cytochrome *c* oxidase were far too intense to arise from a bridging geometry. However, this argument is weakened by the fact that the authors based their conclusions on studies that were narrow in scope and of questionable relevance. Table 2-2 presents the extinction coefficients of the $C\equiv N$ stretch of some previously reported complexes[30] and **1** and **2** in acetone solutions. It can be seen for the ruthenium systems that the bridged cyanide exhibits a much lower extinction coefficient than does the corresponding unbridged system. However, in the case of the models studied here, the extinction coefficient of the $C\equiv N$ stretch is significantly higher in the bridged case, relative to the unbridged case. Therefore, arguments for or against the bridging of cyanide in cytochrome oxidase based upon the intensity of the cyanide stretching vibrations are not well founded.

An interesting feature of the binuclear center in the bovine resting enzyme that has emerged in the crystal structure[7] is that Cu_b is positioned 1 Å off the normal of the heme a_3 plane (Figure 2-9). From simple geometric arguments (assuming reasonable distances for the Fe-C and $C\equiv N$ distances, and the 4.5 Å distance provided by the crystal structure to accommodate a linear Fe-C \equiv N angle), the $C\equiv N$ -Cu bond angle would be 138°. From the correlation published by Scott and Holm[17] this would lead to a Cu-N distance of ≈ 2.4 Å and $\nu_{C\equiv N} \approx 2120$ cm^{-1} . However, the $\nu_{C\equiv N}$ observed for cyanoferrocyanide is 2151 cm^{-1} [14]. This frequency correlates with a Cu-N distance of ~ 2.1 Å and a Cu-N \equiv C angle of ~ 155 -160°. This implies that the Cu_b ion must be *displaced* from the position seen in the crystal structure of the oxidized bovine enzyme[7] *which* requires a certain degree of structural flexibility in the protein structure near the

Fig
oxi

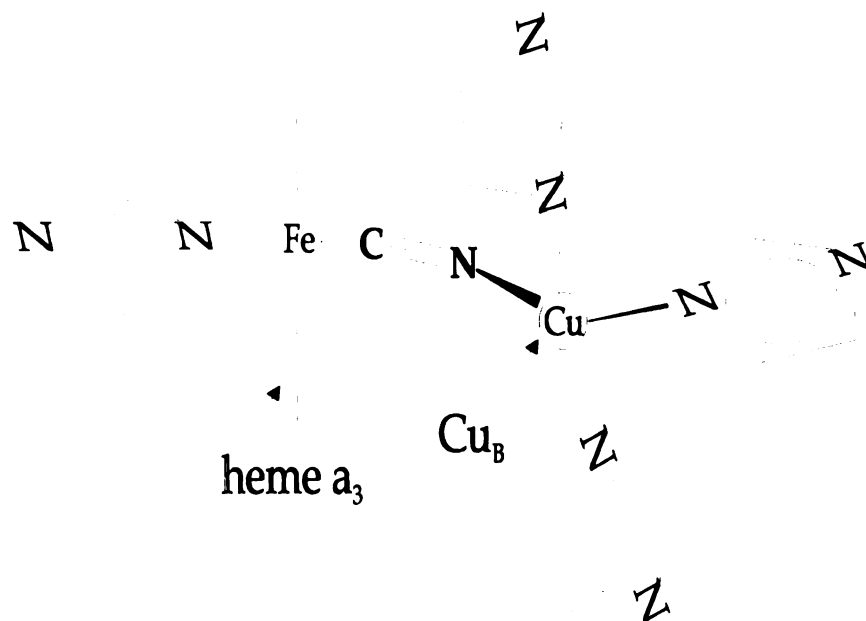


Figure 2-9: Representation of the binuclear center of oxidized cytochrome c oxidase.

binuclear cen

a Fe-Cu dista

detected betw

ligated solven

resting, oxidi

center has the

binuclear center of cytochrome c oxidase. Indeed, this is supported by the observation of a Fe-Cu distance of 5.2 Å in the azide-treated bacterial oxidase[8]. Electron density is detected between the two metals of the binuclear center, due either to the presence of a ligated solvent or azide molecule, while no intermetal electron density is detected in the resting, oxidized bovine system. This variable Fe-Cu distance indicates that the binuclear center has the ability to alter its geometry to accommodate exogenous ligand binding.

1. Malm
2. Babco
3. Einar
4. Rich.
5. Fergu
6. Kitig
7. Tsuki
Shinz
269; 1
8. Iwata
9. Palm
10. Caug
Bioer
11. Oertli
Wooc
12. Kim,
and O
13. Yoshi
3518.
14. Yoshi
1995.

LIST OF REFERENCES

1. Malmstrom, B.G., Acc. Chem. Res., 1993. **26**: p. 332.
2. Babcock, G.T. and Wikstrom, M., Nature, 1992. **356**: p. 301.
3. Einarsdottir, O., Biochim. Biophys. Acta, 1995. **1229**: p. 129.
4. Rich, P.R., J.Plant Physiol., 1995. **22**: p. 479.
5. Ferguson-Miller, S. and Babcock, G.T., Chem. Reviews, 1996. **96**: p. 2889.
6. Kitigawa, T. and Ogura, T., Prog. Inorg. Chem., 1996. **45**: p. 431.
7. Tsukihara, T., Aoyama, H., Yamashita, E., Tomizaki, T., yamaguchi, H., Shinzawa-Itoh, K., Nakashima, R., Yaono, R., and Yoshikawa, S., Science, 1995. **269**: p. 1069.
8. Iwata, S., Ostermeier, C., Ludwig, B., and Michel, H., Nature, 1995. **376**: p. 660.
9. Palmer, G., J. Bioenerg. Biomembr., 1993. **25**: p. 145.
10. Caughey, W.S., Dong, A., Sampath, V., Yoshikawa, S., and Zhao, X.-J., J. Bioenerg. Biomembr., 1993. **25**: p. 81.
11. Oertling, W.A., Surerus, K.K., Einarsdottir, O., Fee, J.A., Dyer, R.B., and Woodruff, W.H., Biochemistry, 1994. **33**: p. 3128.
12. Kim, Y., Babcock, G.T., Surerus, K.K., Fee, J.A., Dyer, R.B., Woodruff, W.H., and Oertling, W.A., Biospectroscopy, Submitted for publication.
13. Yoshikawa, S., O'Keefe, D.H., and Caughey, W.S., J. Biol. Chem., 1985. **260**: p. 3518.
14. Yoshikawa, S., Mochizuki, M., Zhao, X.-J., and Caughey, W.S., J. Biol. Chem., 1995. **270**: p. 4270.

15. Nakamoto, K., *Infrared and Raman Spectra of Inorganic and Coordination Compounds*. 1987, New York: Wiley-Interscience.
16. Lee, S.C., Scott, M.J., Kauffmann, K., Munck, E., and Holm, R.H., J. Am. Chem. Soc., 1994. **116**: p. 401.
17. Scott, M.J. and Holm, R.H., J. Am. Chem. Soc., 1994. **116**: p. 11357.
18. Scott, M.J., Lee, S.C., and Holm, R.H., Inorg. Chem., 1994. **33**: p. 4651.
19. Kent, T.A., Munck, E., Dunham, W.R., Filter, W.F., Findling, K.L., Yoshida, T., and Fee, J.A., J. Biol. Chem., 1982. **257**: p. 12489.
20. Kent, T.A., Young, L.J., Palmer, G., Fee, J.A., and Munck, E., J. Biol. Chem., 1983. **258**: p. 8543.
21. Barnes, Z., Babcock, G.T., and Dye, J.L., Biochemistry, 1991. **30**: p. 7597.
22. Kauffman, K.E., Doy, E.P., Munck, E., Lee, S.C., and Holm, R.H., Inorg. Chem. Submitted for publication.
23. Lee, S.C. and Holm, R.H., J. Am. Chem. Soc., 1993. **115**: p. 11789.
24. Karlin, K.D., Nanthakumar, A., Fox, S., Murthy, N.N., Ravi, N., Huynh, B.H., Orosz, R.D., and Day, E.P., J. Am. Chem. Soc., 1994. **116**: p. 4753.
25. Scott, M.J., Zhang, H.H., Lee, S.C., Hedman, B., Hodgson, K.O., and Holm, R.H., J. Am. Chem. Soc., 1995. **117**: p. 568.
26. Wilson, E.B., Decius, J.C., and Cross, P.C., *Molecular Vibrations*. 1955, New York: McGraw-Hill.
27. Shimanouchi, T., *Computer Programs for Normal Coordinate Treatment of Polyatomic Molecules*. 1969, Tokyo: Tokyo University.
28. McIntosh, D.F. and Michaelian, K.H., Canadian Journal of Spectroscopy, 1979. **24**: p. 1.
29. Lopez-Garriga, J.L., Oertling, W.A., Kean, R.T., Hoogland, H., Wever, R., and Babcock, G.T., Biochemistry, 1990. **29**: p. 9387.
30. Doorn, S.K., Dyer, R.B., Stoutland, P.O., and Woodruff, W.H., J. Am. Chem. Soc., 1993. **115**: p. 6398.

31. Spir
Spir
32. Yu.
81: p
33. Uno
3215
34. Kerr
35. Sanc
36. Dow
33.
37. Alva
123.
38. Tana

31. Spiro, T.G., *Biological Applications of Resonance Raman Spectroscopy*, ed. T.G. Spiro. Vol. 3. 1988, New York: Wiley.
32. Yu, N.-T., Benko, B., Kerr, E.A., and Gersonde, K., *Proc. Natl. Acad. Sci.*, 1984. **81**: p. 5106.
33. Uno, T., Hatano, K., Nishimura, Y., and Arata, Y., *Inorg. Chem.*, 1988. **27**: p. 3215.
34. Kerr, E.A., Mackin, H.C., and Yu, N.-T., *Biochemistry*, 1983. **22**: p. 4373.
35. Sano, M. and Yamatera, H., *Chem. Phys. Lett.*, 1979. **60**: p. 257.
36. Dows, D.A., Haim, A., and Wilmarth, W.K., *J. Inorg. Nucl. Chem.*, 1961. **22**: p. 33.
37. Alvarez, S., Lopez, C., and Bermejo, M.J., *Transition Met. Chem.*, 1984. **9**: p. 123.
38. Tanaka, T., Yu, N.-T., and Chang, C.K., *Biophys. J.*, 1987. **52**: p. 801.

CHAPTER 3

SMALL MOLECULE BINDING TO HEME PROTEINS: VIBRATIONAL SPECTROSCOPY OF THE LIGAND BINDING SITE IN THE .NO BINDING ENZYME SOLUBLE GUANYLATE CYCLASE

Abstract

Infrared spectroscopy is a useful technique to investigate the modes of binding of small molecules to heme proteins. Carbon monoxide and cyanide are two potential ligands to heme proteins that, due to their high molar absorptivity, are ideally suited to interrogation by infrared spectroscopy. These ligands also present very characteristic vibrational frequencies that depending upon the specific chemical environment in which they are located. In this chapter, a study is described whereby we investigated the infrared spectrum of carbon-monoxide bound soluble guanylate cyclase (sGC). Soluble guanylate cyclase is the only known physiological receptor for nitric oxide. This heme-containing enzyme also binds carbon monoxide, and to a much lesser extent, dioxygen. The $\text{C}\equiv\text{O}$ vibrational frequency for the CO bound form of sGC was found to be 1987 cm^{-1} , which is the highest reported frequency for a $\text{C}\equiv\text{O}$ stretching vibration in an enzymatic system. This vibration was conclusively identified through the use of isotopic labeling. These vibrational studies of CO bound sGC have elucidated specific details of the binding pocket of this enzyme[1] and subsequently provided information about the mechanism by which NO activates this enzyme.

Introduction

Hemes are porphyrin macrocycles that contain iron as their central atoms. Heme containing proteins play a large number of diverse roles in biological enzymatic processes. These proteins, of which there are hundreds, if not thousands of examples, perform roles in various organisms that range from very complex, such as biological metabolism of molecular oxygen or peroxidic species, to more simple roles such as the storage and transport of reducing equivalents that provide the electrons necessary for other enzymatic systems to carry out their tasks. Many heme proteins also have the ability to bind small molecules such as dioxygen, carbon monoxide, cyanide, nitric oxide or azide, reversibly. While only some of these ligands are physiologically relevant, they all offer unique spectroscopic signals that can provide insight into the modes and mechanisms of ligand binding to these enzymes.

The spectroscopy of small ligand/heme interactions has been studied extensively and reviewed over the last decades [2]. One of the principle tools for studying the interactions of small molecules with heme-proteins has been vibrational spectroscopy. Both infrared and resonance Raman spectroscopies provide opportunities to acquire information about how these small molecules bind to the heme macrocycle. When Raman and infrared spectroscopies are used in conjunction with one another, the complementary data they can determine, can provide a complete description of the vibrational properties of the heme-ligand complex.

There are three normal modes of vibration expected for an Fe-X-Y unit, as is found when a diatomic ligand binds to the iron of a heme macrocycle. These are the Fe-XY stretching mode, the Fe-X-Y bending mode and the X-Y stretching mode. The

vibrational frequency of each of these modes contains particular information about the geometry and environment of the Fe-X-Y unit. The technique that is best suited to observe the various vibrations depends upon the specific experimental conditions. Typically, infrared spectroscopy is utilized to observe the X-Y stretching mode. This is because the X-Y stretching vibration is not electronically coupled into the heme molecular orbital system, which results in a lack of adequate resonance enhancement in a Raman experiment. The Fe-XY stretching mode, and the Fe-X-Y bending mode, however, are usually resonance enhanced with excitation into the heme absorption bands, which, when combined with the chromophore-specificity of Raman spectroscopy, makes that a very potent tool for studying heme-ligand vibrational behaviors.

Infrared Spectroscopy of Heme Proteins

It is fortuitous that many of the small molecules that bind to hemes exhibit large molar absorptivities for infrared radiation. This allows the determination of the vibrational frequencies of these ligands without needing to utilize unreasonably large quantities of samples. Many studies have been published that use the well characterized vibrational frequencies of $\text{C}\equiv\text{O}$, or $\text{C}\equiv\text{N}$ as markers to provide information regarding various types of interactions that can be present in the heme binding pocket of the enzyme[3-13]. The vibrational frequencies of these ligands have been shown to be highly sensitive to various types of interactions that *in vivo* could play a significant role in the chemistry of these ligand-binding sites. Previously, we have shown that the vibrational frequency of a $\text{C}\equiv\text{N}$ ligand to a molecular heme-copper assembly can be used to support

the proposal that $\text{C}\equiv\text{N}$ exists in a bridging conformation in the oxidized, cyanide ligated form of the respiratory enzyme cytochrome c oxidase[5]. Likewise, the isoelectronic $\text{C}\equiv\text{O}$ molecule also exhibits $\text{C}\equiv\text{O}$ stretching frequencies that are highly dependent upon the interactions with the surrounding protein or solvent environment. Thus, accurately determining these vibrational frequencies can aid in parameterizing the molecular interactions in a ligand-heme complex.

It has been shown that, when there is a distal interaction present in a heme binding pocket, the vibrational frequency of a bound cyanide molecule is shifted to significantly higher frequency (see previous chapter and references therein) when compared to the $\text{C}\equiv\text{N}$ stretching frequency of an unperturbed heme-cyanide complex, or to the frequency of free cyanide ion. An example of the type of distal interaction that may be encountered in the heme pocket of an enzyme is hydrogen bonding to the distal end of the ligand molecule. In the case of cyanide, which is primarily a σ -donating ligand, this distal interaction will remove electron density from the slightly antibonding HOMO of the cyanide ion, effectively increasing the $\text{C}\equiv\text{N}$ force constant, and thus the vibrational frequency. Carbon monoxide, when subjected to the same hydrogen bond, however, will exhibit a relative *redshift* in the vibrational frequency of the $\text{C}\equiv\text{O}$ stretching mode of vibration. The reason for the opposite response of CO to the presence of the distal interaction originates in the different electronic configuration of CO versus CN. This different configuration results in CO acting as a π -acid, rather than a σ -donor. When CO is ligated to a Fe atom, the ligand accepts electron density in to its antibonding LUMO, which reduces the carbon-oxygen force constant. The result is that CO exhibits a lower

C-O stretching frequency when it is ligated to a heme, than when it is unbound. If an additional interaction, such as a hydrogen bond, is introduced at the distal end of a heme-ligated CO molecule, the effect will be a further increase in the electron density in the π^* -orbital, which will result in a further decrease in the C \equiv O stretching frequency[14, 15]. The presence (or lack) of a hydrogen bonding interaction, therefore, will be reflected in the observed vibrational frequency of the bound ligand. As a result, by comparing the frequencies of bound ligands to those of unbound ligands, one can draw some detailed conclusions about interactions between the heme molecule, the ligand, and the surrounding protein matrix in which the heme resides.

Infrared spectroscopy is typically hampered by the presence of water in the sample. However, when cyanide or carbon monoxide is the ligand, their primary stretching vibration is observed in a region of the infrared spectrum where water has minimal absorbances (Figure 3-1). This fact, coupled with the large extinction coefficient for the primary X-Y stretching mode, allows the use of a cell with a relatively long pathlength ($\sim 50 \mu\text{m}$), which, in conjunction with moderately concentrated samples ($> 50 \mu\text{M}$) and highly sensitive MCT-type infrared detectors, allows for relatively facile collection of data.

Resonance Raman of Heme Ligand Interactions

Resonance Raman spectroscopy is a technique that is ideally suited for the study of heme containing systems. Because hemes exhibit very strong absorbances in the

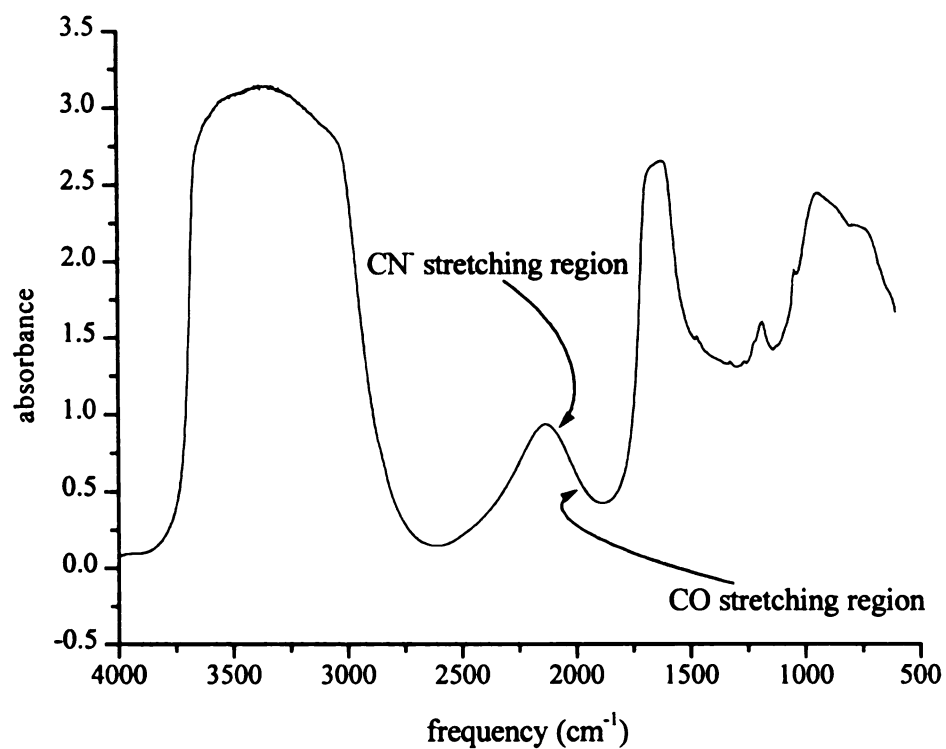


Figure 3-1: Infrared absorption spectrum of water, CaF₂ cell, 50μm pathlength, 25 °C. Approximate frequencies of X-Y stretches of heme-ligated XY diatomic ligands are shown (XY = C≡N or C≡O)

visible region of the electromagnetic spectrum, there are many opportunities to utilize the resonance enhancement effect of Raman spectroscopy. Additionally, Raman spectroscopy is not subjected to the same limitations with respect to water content of the samples, as is infrared spectroscopy.

The vibrational modes of the axial ligands of heme macrocycles are typically observed with Raman spectroscopy using excitation frequencies that correspond to the so-called B and Q electronic transitions of the porphyrin moiety (Figure 3-2). These absorptions in the optical spectrum are characteristic for heme containing systems. The observed absorptions are primarily the result of π - π^* transitions, and it has been seen that the excitation profiles of heme-ligand modes (when the ligand is a π -acid such as CO, NO or O₂) correspond directly to these electronic transitions.

Much effort has been expended in detecting the various normal modes of vibration for heme-ligand systems. Vibrational measurements on CO-bound heme systems are particularly useful to infer the status of the proximal ligand and the environment of the distal pocket because the correlation between the fundamental stretching frequencies, $\nu(\text{Fe-C})$ and $\nu(\text{C}\equiv\text{O})$, is well established in both model porphyrin and heme-protein systems[16]. This correlation is understood by considering that as the metal d_π backbonding to the $\text{C}\equiv\text{O}$ ligand increases, the Fe-C bond strength increases. However, as a result of this, the electron density in the $\text{C}\equiv\text{O}$ π^* orbital also increases, lowering the bond order, and thus the $\text{C}\equiv\text{O}$ vibrational frequency. This correlation can be seen clearly in Figure 3-3, where the Fe-C vibrational frequencies from a number of heme-protein and model compounds are plotted against the $\text{C}\equiv\text{O}$ vibrational frequencies

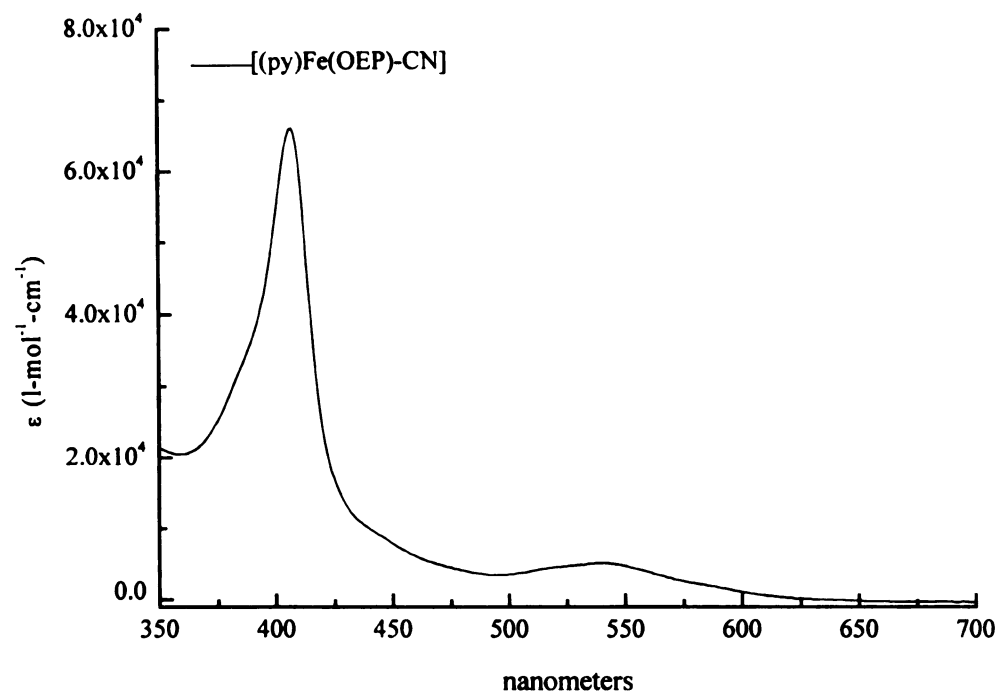


Figure 3-2: UV-Vis spectrum of heme-ligand complex ($[(py)Fe(OEP)-CN]$). Sample concentration = 2.2 mM, in acetone. Spectrum acquired in 50 μm CaF_2 cell, room temperature.

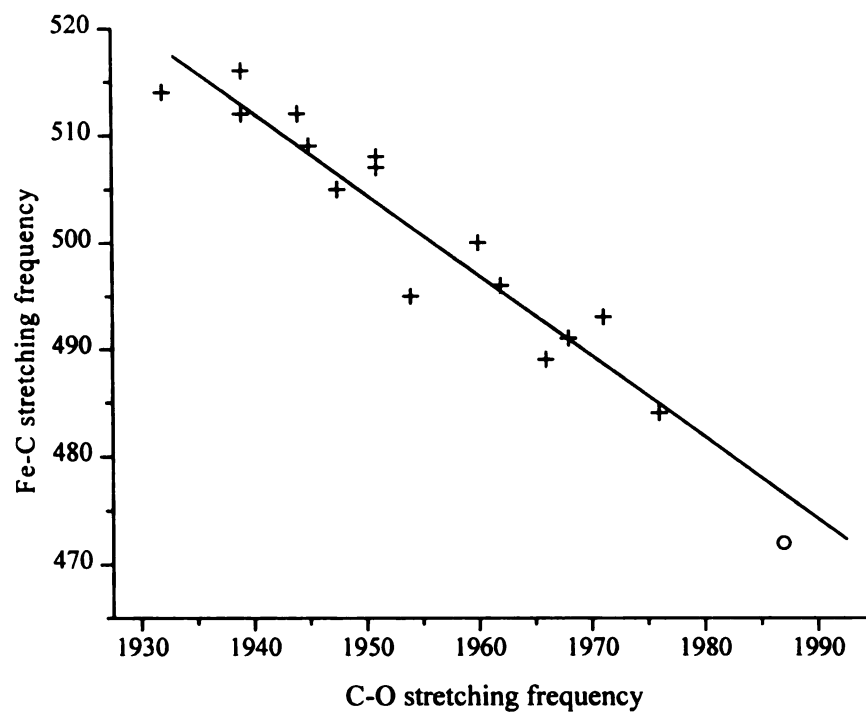


Figure 3-3: Correlation between Fe-C stretching frequencies and C-O stretching frequencies for a variety of histidine ligated carbonmonoxy heme complexes. Adapted from [16].

from the same systems. When the *trans*-ligand is constant, in this case histidine, there is a distinct inverse linear relationship between the vibrational frequencies.

The Fe-C≡O bending vibration is typically observed in the Raman spectra of hemoproteins at around 575 cm⁻¹, while the Fe-C≡N bending mode typically occurs in the range of 400 cm⁻¹ to 450 cm⁻¹. An interesting observation is that the Fe-C≡O bending mode has not been observed in a synthetic heme-ligand system where the C≡O ligand binds parallel to the normal of the heme plane. With CN⁻ as the ligand, the bending mode has also been detected in a relatively limited number of cases. It has been successfully resonance enhanced, however, in hindered systems, such as the strapped heme systems developed by Chang and co-workers [17]. This mode of vibration has also been detected in numerous heme-protein systems where there is the possibility of a distal interaction arising from the protein matrix or where the protein may have forced the ligand to adopt a nonlinear binding geometry.

The Fe-CO stretching vibration, on the other hand, is typically detectable with all heme-ligand systems as is the Fe-CN stretching mode. This difference between the relative enhancements of the bending versus the stretching modes has been attributed to the geometry of binding in a number of different studies [2]. The argument states that when the ligand is forced to adopt a bent configuration, its empty π^* orbitals can more easily interact with the electron density at the pyrrole nitrogens in the porphyrin π^* orbital. It is this interaction that gives rise to the porphyrin-to-ligand charge transfer that is responsible for the observed resonance enhancement. However, there is a case in which the ligand is bound in a strictly linear fashion, yet resonance enhancement of the bending

mode is observed[5]. In this case, the resonance enhancement may be attributed to the presence of a ligand-to-metal charge transfer transition in the 650 nm region of the electronic absorption spectrum. The precise mechanism by which bending modes of heme-ligand modes are resonance enhanced, however, requires further study in order to be understood fully.

Soluble guanylate cyclase is the only known physiological receptor for the intercellular signaling agent nitric oxide ($\bullet\text{NO}$). When $\bullet\text{NO}$ is bound to the enzyme, sGC catalyzes the conversion of GTP to cGMP, which has been implicated as a factor in many important physiological events such as vascular smooth muscle relaxation, platelet aggregation and neuronal communication. The rate of GTP to cGMP conversion by sGC increases by 400-fold over the basal level of activity upon $\bullet\text{NO}$ binding. sGC is a heterodimer, and each unit contains one protoporphyrin IX type heme which is the target for $\bullet\text{NO}$ binding. The heme Fe^{II} is 5-coordinate high-spin with histidine as the axial ligand. However, unlike other 5-coordinate high-spin heme proteins, sGC shows unusual behavior toward small ligands such as O_2 , CO, nitrosomethane, and $\bullet\text{NO}$. The affinity for O_2 is so low that in air-saturated buffer the heme Fe remains 5-coordinate. This is physiologically important because most hemes will rapidly bind oxygen, and then react with $\bullet\text{NO}$. CO binds to the heme of sGC, but the affinity is much lower than for typical 5-coordinate ferrous imidazole-ligated heme proteins such as hemoglobin and myoglobin. This reduced affinity for sGC is primarily due to an increased off rate (3.5 s^{-1}). $\bullet\text{NO}$ binds to the heme Fe of sGC to form a transient 6-coordinate heme. In this complex, however, the Fe-His bond is unstable and the breakage of this bond is believed to be linked to the activation of the enzyme. While the binding of $\bullet\text{NO}$ to heme is virtually irreversible in

both model systems and heme proteins, dissociation of •NO from heme of sGC appears to be fast, as hypothesized from whole organ studies[18]. Recent kinetic studies with purified sGC provide molecular evidence to support this speculation. A similar ligand, nitrosomethane (CH_3NO) which typically binds irreversibly to high-spin ferrous heme proteins to form a 6-coordinate complex, also binds to the heme of sGC but in a reversible manner due to a fast off rate[19]. The observations for all of these ligands deviate from what is commonly observed for heme-proteins and indicate that the heme environment in sGC is distinct from that of other heme-containing proteins. Vibrational spectroscopy can provide insight into how the heme-binding site of the enzyme affects the ligand binding properties of this enzyme, and can thus shed light upon the mechanism of •NO activation.

Recently, Deinum *et. al.* reported resonance Raman data for the CO and •NO ligated form of sGC [20]. These data are presented in Figure 3-4 and are tabulated in Table 3-1. The Raman results show the Fe-CO stretching frequency at 472 cm^{-1} , which is the lowest frequency yet observed for a CO-bound heme complex. It is assigned as the Fe-CO stretching mode due to the fact that, as the mass of the ligand is increased through the use of isotopically labeled ligand, the observed frequency decreases. There is also a vibrational mode observed at 562 cm^{-1} that exhibits isotope dependent frequencies. Because the stretching mode is conclusively assigned through the use of isotopes, this mode, by default, is assigned to the Fe-C \equiv O bending vibration. A mode was observed at 204 cm^{-1} that was assigned to a proximal histidine residue, present in the 6-coordinate CO-species. This is particularly low for a Fe-His bond. On the basis of the *trans*-effect

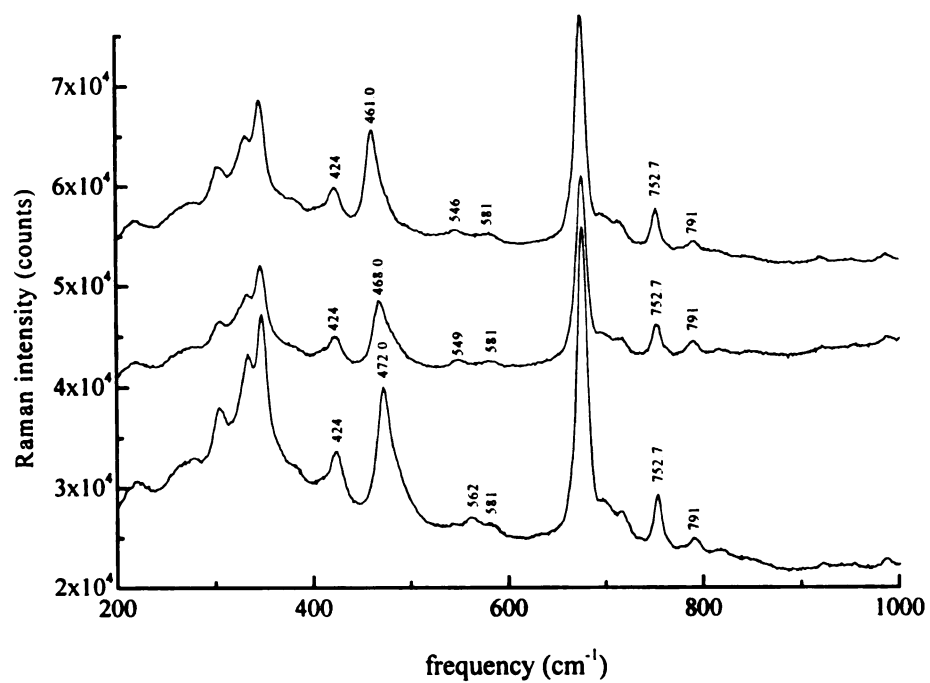


Figure 3-4: Resonance Raman spectrum of isotopomers of carbonmonoxy-soluble guanylate cyclase. Laser excitation $\lambda=423$ nm[20].

Table 3-1 Vibrational Frequencies of Various CO-adducts of Heme-enzymes

	$\nu(\text{Fe-CO})$ (cm^{-1})	$\delta(\text{Fe-C}\equiv\text{O})$ (cm^{-1})	$\nu(\text{C}\equiv\text{O})$ (cm^{-1})	ref
CO-sGC	472	562	1987	this work
CO-Mb	512	577	1944	[21, 22]
CO-Hb A	507	578	1951	[22]

described above, a weak Fe-proximal ligand bond will lead to a strong Fe-C bond. However, exactly the opposite is observed which , in addition to the distinct ligand binding properties of sGC, implicates distal effects as playing a major role in defining the ligand binding properties of sGC.

By comparison to the data correlating Fe-C and C \equiv O stretching frequencies (Figure 3-3), predictions about the vibrational properties of sGC become clear. From the data obtained from the Raman spectra regarding the Fe-C stretching frequency, the C \equiv O stretching frequency is predicted to occur close to 2000 cm^{-1} , which would be the highest ever observed for a heme-CO system with a proximal histidine ligand. This prediction, due to the unanticipated nature of the results regarding the low frequencies of both the Fe-C and the Fe-His bonds, warrants testing. The results of these experiments are described here.

Materials and Methods

All enzyme samples were isolated in the laboratory of Professor Michael Marletta, University of Michigan, Ann Arbor. Soluble guanylate cyclase was isolated from bovine lung as described by Stone and Marletta[23] except that the last desalting step was done with 25mM TEA, 5mM DTT, 50mM NaCl, pH 7.4 and that no glycerol was added to the sample. The heme content of this preparation was determined to be 1.5 hemes per heterodimer.

FTIR spectra were acquired on a Nicolet 740 FTIR spectrometer equipped with a MCT detector. CO was bound to the sGC sample by exposing it to a positive pressure of CO. The sample was then placed in a CaF_2 cell (50 μM pathlength). CO binding was confirmed by monitoring the shift in the Soret band from 431nm to 423nm. The cell was then thermostated at 3°C in a homebuilt cryostat system equipped with AgCl and Ge windows. Double-sided interferograms were collected at 4 cm^{-1} resolution and apodized by using a Happ-Ganzel apodization function. 20,000, 11,000 and 20,000 scans were averaged for the $^{12}\text{C}^{16}\text{O}$, $^{13}\text{C}^{16}\text{O}$, and $^{13}\text{C}^{18}\text{O}$ isotopically labeled samples, respectively. Smooth polynomial functions were subtracted from the data to baseline correct the data.

Results and Discussion

Figure 3-5 shows FTIR spectra of CO-bound sGC in the 1800-2050 cm^{-1} range. With natural isotopic abundance $\text{C}\equiv\text{O}$, a single peak is observed at 1987 cm^{-1} . This mode shifts to 1943 cm^{-1} with $^{13}\text{C}^{16}\text{O}$ and to 1895 cm^{-1} with $^{13}\text{C}^{18}\text{O}$. The observed isotope shifts are as expected for a $\text{C}\equiv\text{O}$ harmonic oscillator, and therefore, the peak can be

unambiguously assigned to the C≡O stretching mode of a heme-C≡O complex. When this result is examined in the context of the Fe-C/C≡O correlation published by Ray *et al.*[16], it can be seen that the C≡O stretching frequency is indeed higher than has ever been seen for a heme-C≡O complex with a proximal histidine. In addition to this, the fact that this data point clearly falls on the same line as for other proximal histidine/heme-C≡O systems lends support to the proposal that the heme in sGC is, in fact, ligated proximally by a histidine residue.

That a histidine proximally ligates the heme in sGC has previously been inferred from absorption data[24] and the mode observed in the Raman spectrum at 204 cm⁻¹ which had been assigned to the Fe-His stretch[20]. This is consistent with the previous interpretations that the histidine is neither anionic nor hydrogen bonded, because, in these cases, the $\nu(\text{FeC})/\nu(\text{C}\equiv\text{O})$ points fall below the imidazole correlation curve due to the weakened Fe-C σ bond, as shown in a model compound and in horseradish peroxidase at high pH[25]. The position along the correlation curve is mainly determined by the polarity of the distal pocket[16]. sGC falls on this curve at the lowest point thus far observed. The protein nearest to sGC on the curve is the porcine myoglobin mutant [H64V-V68T], in which back-bonding is inhibited due to the negative polarity of the distal pocket in the absence of the hydrogen bonding donor (His 64)[26, 27]. Since sGC falls on this same backbonding curve we infer that there is negative polarity in the distal pocket of sGC. Introducing negative polarity increases not only the stretching frequency of C≡O bound to the heme but also the off-rate of both O₂ and CO binding, as has been

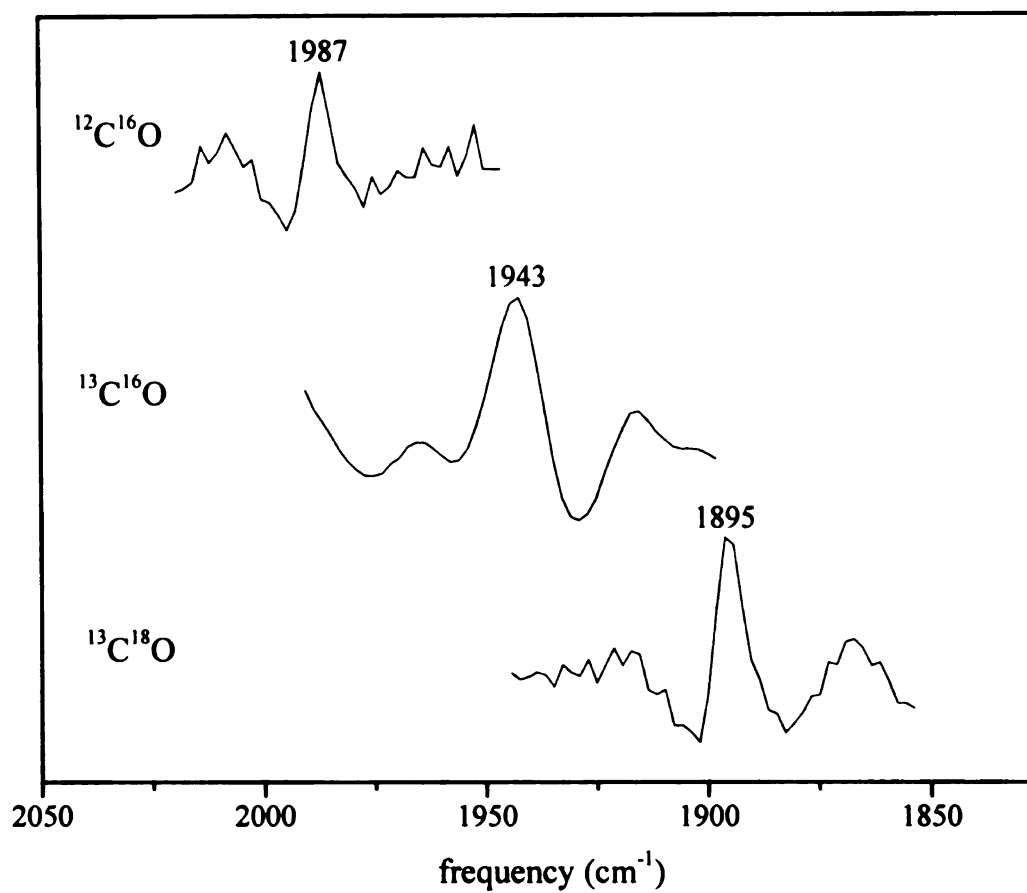


Figure 3-5: FTIR spectrum of isotopomers of carbonmonoxy-soluble guanylate cyclase. Spectral conditions given in Materials and Methods.

shown in the mutant porcine myoglobin samples[26, 27]. The general trend in sGC is the same, showing an increased $\nu(\text{C}\equiv\text{O})$ and a very high off rate for CO (3.5 s^{-1})[19], which further supports the idea that there is negative polarity in the distal pocket of the heme in sGC and that it is a major determinant for the ligand binding properties of sGC.

In general, ligand binding affinity to hemes increases when going from O_2 to CO and to NO. For sGC, a strong decrease for O_2 binding, an increased dissociation rate for CO, and the apparent relative ease for NO dissociation are observed, indicating an apparent overall decreased affinity for these small ligands;. It is very likely that sGC uses the negative polarity to achieve the reduced O_2 binding and the relative ease of NO dissociation. Both of these are necessary for proper functioning of the enzyme.

LIST OF REFERENCES

1. Kim, S., Deinum, G., Gardner, M.T., Marletta, M.A., and Babcock, G.T., *J. Am. Chem. Soc.*, 1996. **118**: p. 8769.
2. Spiro, T.G., *Biological Applications of Resonance Raman Spectroscopy*, ed. T.G. Spiro. Vol. 3. 1988, New York: Wiley.
3. Bogumil, R., Hunter, C.L., Maurus, R., Tang, H.-L., Lee, H., Lloyd, E., Brayer, G.D., Smith, M., and Mauk, A.G., *Biochemistry*, 1994. **33**: p. 7600.
4. Caughey, W.S., Dong, A., Sampath, V., Yoshikawa, S., and Zhao, X.-J., *J. Bioenerg. Biomembr.*, 1993. **25**: p. 81.
5. Gardner, M.T., Deinum, G., Kim, Y., Babcock, G.T., Scott, M.J., and Holm, R.H., *Inorg. Chem.*, 1996. **35**: p. 6878.
6. Hill, J., Goswitz, V.C., Calhoun, M., Garcia-Horsman, J.A., Lemieux, L., Alben, J.O., and Gennis, R.B., *Biochemistry*, 1992. **31**: p. 11435.
7. Palmer, G., *J. Bioenerg. Biomembr.*, 1993. **25**: p. 145.
8. Tsubaki, M. and Yoshikawa, S., *Biochemistry*, 1993. **32**: p. 174.
9. Tsubaki, M. and Yoshikawa, S., *Biochemistry*, 1993. **32**: p. 164.
10. Tsubaki, M., Mogi, T., Hori, H., Sato-Watanabe, M., and Anraku, Y., *J. Biol. Chem.*, 1996. **271**: p. 4017.
11. Yoshikawa, S., O'Keefe, D.H., and Caughey, W.S., *J. Biol. Chem.*, 1985. **260**: p. 3518.
12. Yoshikawa, S. and Caughey, W.S., *J. Biol. Chem.*, 1990. **265**: p. 7945.
13. Yoshikawa, S., Mochizuki, M., Zhao, X.-J., and Caughey, W.S., *J. Biol. Chem.*, 1995. **270**: p. 4270.

14. Nakamoto, K., *Infrared and Raman Spectra of Inorganic and Coordination Compounds*. 1987, New York: Wiley-Interscience.
15. Lopez-Garriga, J.J., Hanton, S., Babcock, G.T., and Harrison, J.F., J. Am. Chem. Soc., 1986. **108**: p. 7251.
16. Ray, G.B., Li, X., -Y., Ibers, J.A., Sessler, J.L., and Spiro, T.G., J. Am. Chem. Soc., 1994. **116**: p. 162.
17. Tanaka, T., Yu, N.-T., and Chang, C.K., Biophys. J., 1987. **52**: p. 801.
18. Palmer, R.M.J., Ferrige, A.G., and Moncada, S., Nature, 1987. **327**: p. 524.
19. Stone, J.R. and Marletta, M.A., Biochemistry, 1995. **34**: p. 16397.
20. Deinum, G., Stone, J.R., Babcock, G.T., and Marletta, M.A., Biochemistry, 1996.
21. Rimai, L., Salmeen, I., and Petering, D.H., Biochemistry, 1975. **14**: p. 378.
22. Tsubaki, M., Srivastava, R.B., and Yu, N.-T., Biochemistry, 1982. **21**: p. 1132.
23. Stone, J.R. and Marletta, M.A., Biochemistry, 1995. **34**: p. 14668.
24. Stone, J.R. and Marletta, M.A., Biochemistry, 1994. **33**: p. 5636.
25. Evangelista-Kirkup, R., Smulevich, G., and Spiro, T.G., Biochemistry, 1986. **25**: p. 4420.
26. Li, T., Quillin, M.L., Phillips, J., G.N., and Olson, J.S., Biochemistry, 1994. **33**: p. 1433.
27. Cameron, A.D., Smerdon, S.J., and Wilkonson, A.J., Biochemistry, 1993. **32**: p. 13061.

CHAPTER 4

PROBING LOW-FREQUENCY VIBRATIONS IN METALLOPROTEINS USING LIGHT INDUCED INFRARED DIFFERENCE SPECTROSCOPY: CHALLENGES AND SOLUTIONS

Abstract

Several critical issues surrounding the successful acquisition of vibrational information in the low frequency region of the infrared spectrum of biological molecules are discussed. These issues include the development of methods to overcome the presence of highly-absorbing water in the sample, the design of systems to control the temperature of the sample within close tolerances and the choice of detectors and window materials that will provide the best opportunity to detect the signals of interest. In the following chapter, data is presented from experiments where these methods were utilized to acquire data possibly originating from the manganese cluster of the photosynthetic enzyme, photosystem II.

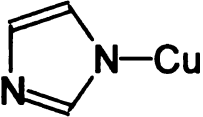
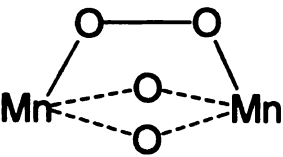
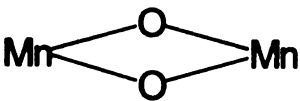
Introduction

Spectroscopists have long recognized the utility of vibrational information when seeking to answer structural or mechanistic questions about metalloproteins. In particular, when studying an enzymatic system, it is desirable to acquire information about low frequency ($<1000\text{ cm}^{-1}$) vibrations, as they may contain a wealth of information directly

related to bonding interactions between the metal site and ligands to the metal site whether the ligands are substrate derived or protein derived. Information about these vibrations could provide direct insight into the structure and, possibly, the specific molecular steps that occur in the catalytic cycle of a metalloenzyme. Table 4-1 shows some examples of structures that are present (or proposed to be present) in certain metallo-enzymes along with their estimated vibrational frequencies. Close examination of the normal mode compositions of these vibrations shows that they will also display very characteristic isotopic dependencies upon isotopic substitution. It has been shown in numerous studies that isotopic labeling allows for the unequivocal assignment of vibrational modes. The usefulness of vibrational information is clear. If low frequency vibrational information can be acquired from the enzymatic systems, then specific questions regarding the mechanistic details of these systems can be addressed.

Until recently, the experimental techniques available to gain access to the low-frequency vibrations were primarily limited to forms of resonance Raman spectroscopy. Although a powerful technique for studying some systems, namely those that contain highly absorbing chromophores, resonance Raman spectroscopy is certainly not capable of addressing all of the needs of the biological vibrational spectroscopist. The other primary technique for gathering vibrational spectra is infrared (IR) spectroscopy. This technique, which relies upon detecting absorbances of IR radiation, is not *a priori* suited for studying biological systems, let alone the low frequency vibrational modes exhibited by these systems. This is due to the fact that proteins, in their native environment, are solvated by a large molar excess of water. Because water exhibits very strong absorbances at several characteristic regions through out the infrared spectrum, its

Table 4-1 Vibrational Frequencies of Protein and Metal-Ligand Structures

Structure	Approximate Vibrational Frequency (cm ⁻¹)
Protein Backbone Modes	
Amide V (NH _{ob} , CN _l) [*]	725
Amide IV (C _{ob} , CC _s , CNC _d)	625
Amide VI (CO _{ob} , CN _l)	600
Amide VII (NH _{ob} , CN _t , CO _{ob})	200
Metal-Ligand Modes	
Fe—CO	450
Cu—CO	400
 N—Cu	250-350
Ni—CO	450-500
Mn=O	750
Mn—OH	400-500
 Mn—O—Mn	600-800
 Mn—O—Mn	600-700
Mn—Cl	300-400

- s, stretch; d, deformation; t, torsion; ib, in-plane-bend; ob, out-of-plane-bend

presence could obscure the detection of signals originating from solute molecules. In this chapter, we will describe methods we have developed by using reaction-modulated infrared difference spectroscopy (particularly *light-induced* FTIR difference spectroscopy) whereby solvent subtraction is handled automatically and that also allow the acquisition of vibrational information, in the low frequency ($<1000\text{ cm}^{-1}$) region of the infrared spectrum.

Aside from the issues surrounding solvent water absorbances, there are a number of other technical challenges that need to be addressed in order to s interrogate sample successfully, and obtain reliable information regarding low frequency modes of vibration. These challenges include detector sensitivity, the choice of suitable sample substrate materials, and the necessity for precise sample temperature control. These challenges and some solutions to them, are addressed in the following chapter.

What Will be Found in the Low Frequency Region?

The low frequency infrared spectra of proteins are an under-investigated spectroscopic region. While much work has been done to assign vibrational modes in the region above 1000 cm^{-1} , very little foundation has been laid for the assignment of modes below 1000 cm^{-1} . From studies of N-methyl acetamide, some predictions can be made about the vibrational modes that polypeptides may exhibit in their infrared absorbance spectra[Arrondo, 1993 #78]. These are summarized in Table 4-1. This table predicts that proteins should display several vibrations, in the low frequency region, that arise from primarily out-of-plane vibrations of the peptide backbone.

Aside from modes having their origin in the protein backbone, there are other vibrations that should appear in the low frequency region of the spectrum. Metal ligand complexes, in proteins and synthetic model compounds, also will display vibrations in the low frequency region of the spectrum. Some of these are also listed in table 4-1. It has been shown previously [1] that heme-ligand complexes exhibit low frequency IR-detectable modes. Metal-oxygen species, such as those proposed to exist in the catalytic cycles of cytochrome c oxidase, or photosystem II will exhibit infrared absorptions, that, when substituted with the appropriate isotope, will show very characteristic frequency shifts. This technique of using isotopes to shift the vibrational frequency of a mode to aid in its assignment, plays a critical role in biological vibrational spectroscopy. This is especially true when there are a large number of peaks in a spectrum, and it is desired to assign one or several of them to a specific molecular species. From Table 4-1, it is clear that developing methods whereby one can detect low frequency vibrational modes in enzymatic systems will be of great use in helping to elucidate mechanistic details of their catalytic cycles.

FTIR of Aqueous Systems: The Low-Frequency Challenge

The primary issue facing the biological infrared spectroscopist pertains to water content of the samples. Water, the ubiquitous solvent for biological systems, hampers typical infrared spectroscopy due to the fact that it exhibits strong absorbances in several different regions throughout the mid infrared spectrum and completely obscures the region below 1000 cm^{-1} (Figure 4-1). The strong absorbance centered at approximately 3400 cm^{-1} is due to the O-H stretching modes of water, the peak at $\sim 1650\text{ cm}^{-1}$ is

attributed to the H-O-H bending mode, and the intense, broad feature below 1000 cm^{-1} is attributed to the strongly coupled lattice vibrations of aggregates of water molecules. In order that one may observe vibrational modes of the enzyme that overlap any of the water absorbances, ways must be found to either eliminate these absorbances entirely, reduce them to levels where they can be accurately subtracted out of the spectrum, finesse the issue by using reaction modulated difference spectroscopies, or use some combination of the above strategies so that the signals of interest become detectable. In particular, we are interested in finding methodologies by which we can observe modes of vibration below 1000 cm^{-1} in the infrared spectrum of enzymatic systems.

The extinction coefficients of the various water absorbances have been well characterized[2, 3]. Table 4-2 lists these vibrational modes, and the associated extinction coefficients. With this information, it is possible to perform a simple Beers Law type calculation to determine the pathlength necessary to return a water absorbance that is reproducible within the technical limitations of the instrumentation. Various detectors and instruments will have different limitations with respect to the linearity of their response to a given absorbance. The generally accepted rule-of-thumb states that in order for a solvent spectrum to be accurately subtracted from a protein sample, the overall absorbance of a given peak must be less than one absorbance unit (a.u.)[5]. With this limitation for the absorbance of the sample, the pathlength of an aqueous solution must not exceed $10\mu\text{m}$, if we are considering the extinction due to the water bending vibration centered at 1645 cm^{-1} . This method of using simple Beers Law calculations to address the water absorbance problem has been successfully applied in numerous different infrared

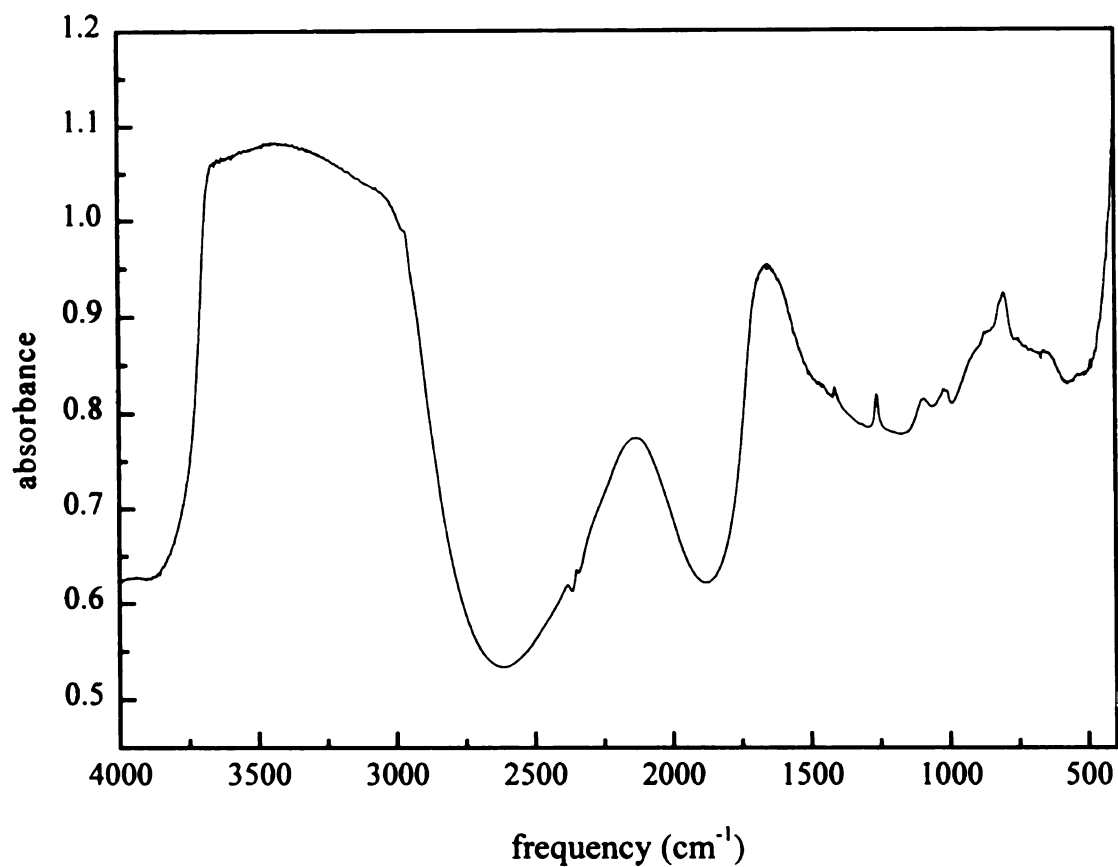


Figure 4-1: Infrared absorption spectrum of water. Spectrum acquired in an AgCl cell, room temperature, 32 scans, $\sim 5\mu\text{m}$ pathlength.

Table 4-2 Infrared Absorbances of H₂O and D₂O[4]

Vibration	H ₂ O (cm ⁻¹)	ε(M ⁻¹ cm ⁻¹)	D ₂ O(cm ⁻¹)	ε(M ⁻¹ cm ⁻¹)
O-X stretch	3920	0.83	2900	0.60
	3490	62.7	2540	59.8
	3280	54.5	2450	55.2
Association	2125	3.23	1555	1.74
X-O-X bending	1645	20.8	1215	16.1
Libration	Broad absorbance below 1000 cm ⁻¹			

studies. By using a combination of highly concentrated samples that reduced the effective water concentration from 55M, and a short optical pathlength, infrared spectra have been acquired that showed very satisfactory subtraction of the interfering water signals[6]. However, these studies have been limited to the region above 1000 cm⁻¹. This method is not applicable, if one wishes to acquire information below 1000 cm⁻¹. This is due to the fact that the large water lattice vibrations below 1000cm⁻¹, even when measured with pathlengths as short as 5μm, do not show adequate subtraction characteristics. The bands are so exquisitely sensitive to minute changes in pathlength, or sampling conditions (temperature, ionic strength, etc.)[3], that large subtraction artifacts remain even after careful subtraction (Figure 4-2)

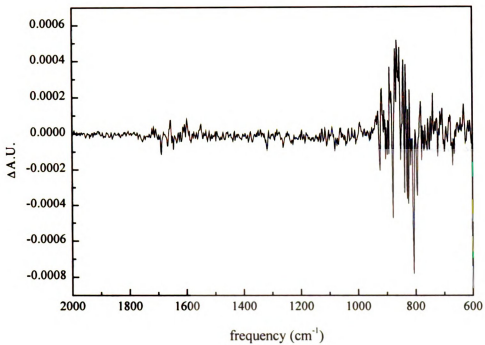


Figure 4-2: Difference spectrum of water sample showing poor subtraction characteristics below 1000 cm⁻¹. 5 μ m pathlength, 200K, AgCl sample cell.

A technique that elegantly addresses the issues of solvent subtraction is *reaction modulated* FTIR spectroscopy[7]. This technique consists of interrogating a sample and digitally storing the spectrum from that sample. Then, exactly the same sample, through some method, is induced to undergo some reaction (light is the reaction-inducing agent in this set of studies, but other reaction modulating techniques have been used, such as exposure to an electric field) and another spectrum is acquired from the same sample in this new state. The pre-reaction and post-reaction spectra are then subtracted, and the resulting *difference* spectrum reflects the vibrational changes that have taken place as a result of the chemistry that has occurred in the sample.

This technique allows the issue of solvent subtraction to be finessed, in that exactly the same sample is interrogated for each of the spectra. While there will be (hopefully!) slight vibrational differences that arise from the reaction that was induced, there will be no gross perturbation of the solvent concentration, ionic strength or pathlength. Thus the large scale baseline distortions that are common in solvent subtracted data are eliminated. In addition, this technique allows for the examination of very small signals, superimposed upon very large background absorbances. It is common for samples to exhibit an infrared absorbance spectrum that approaches one absorbance unit in intensity. However, the slight perturbations that result from the reaction of interest, may affect only a few amino acids, or just the substrate molecule. Therefore the absorbance changes arising from these perturbations may constitute a fraction of a percent of the overall signal. With sufficient signal to noise ratios, it is not uncommon, using this technique, to be able to observe difference signals with intensities of approximately 10^{-5} a.u. These small signals, which may reflect changes in the enzyme

that are directly related to the catalytic cycle, are the type of information we are seeking to acquire. Using modern instrumentation (including detection schemes), it is possible to detect changes in single amino acid residues in enzymes with molecular weights approaching one *million* daltons.

This reaction modulated difference technique provides a very detailed look at the changes that occur as an enzyme system undergoes its catalytic cycle. In Figure 4-3, the theoretical construction of such a difference spectrum is presented. The Figure shows a possible step in the catalytic cycle of Photosystem II, the enzyme in plants responsible for oxidizing water, to molecular oxygen. In the initial state (4-3a), the substrate water, in the form of a hydroxide molecule, is bound to the enzyme active site, but no chemistry (bond breaking/bond making) has occurred with regards to the substrate. An infrared spectrum of the enzyme in this "prereaction" state is acquired and stored digitally. This spectrum contains the vibrational information from the enzyme and the substrate molecule (including, for example, the absorbance due to the μ -oxo bridges of the manganese cluster, and the Mn-OH bond). Then, the enzyme is induced to perform a step (or multiple steps) of the catalytic cycle. When the enzyme has reached a new point in the catalytic cycle (the "stopping point" depends upon the thermodynamic, kinetic, and biochemical control that the investigator can exert over the sample), another spectrum is acquired (4-3b). This spectrum contains the vibrational information indicating the presence of the new species (the Mn-oxo species). This second spectrum is then

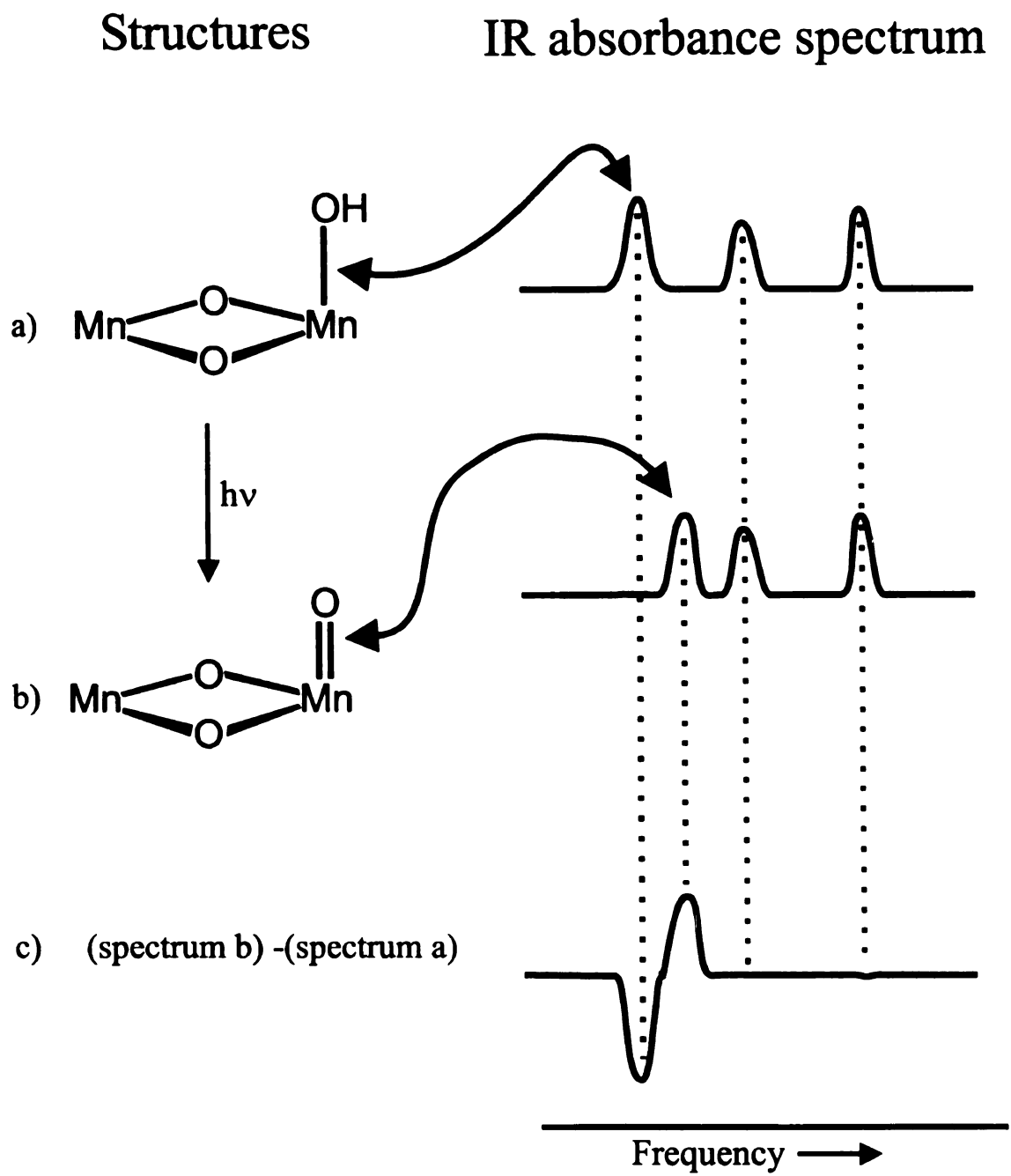


Figure 4-3: Construction of a theoretical light-induced difference spectrum.

subtracted from the first spectrum. The difference spectrum (4-3c) displays both positive and negative peaks that correspond, in the case of the positive going-modes, to oscillators that appear after the enzyme acts on the substrate, and the negative-going modes correspond to vibrational modes that disappear as the substrate is reacted. Any vibrational modes that are remote from the active sight, including the vast majority of solvent molecules, will be unaffected by the distant reactions, and thus will display exactly the same vibrational frequency before and after the enzyme-substrate reaction. They will be subtracted out, leaving a flat baseline. Any vibrational modes that are slightly perturbed (an amino acid residue gaining or losing a hydrogen bonding interaction, a solvent molecule that is in the active site of the enzyme, or something less dramatic such as a vibration whose normal mode composition changes subtly) will appear as difference peaks.

With the advent of reaction modulated difference spectroscopy, the issue of solvent subtraction was addressed in a very elegant manner. However, in order for solvent subtraction to be successful, it is necessary to have samples that do not absorb the infrared radiation too highly, or else the detectors will measure absorbances at levels at which their responses cannot be considered linear and therefore reliable. Any difference spectra acquired under these highly absorbing conditions will contain systemic errors. Short pathlengths is one method that can be used to ensure that fully hydrated samples do not exhibit absorbances that exceed the limits of the instrumentation. This method has been used in several studies of photosystem II, the enzyme responsible for the oxidation of water to molecular oxygen in plants and cyanobacteria,[8-16] and the bacterial reaction center[7] where highly concentrated pellets of the reaction centers were pressed between

the sampling windows to produce both a short pathlength, and an extremely high concentration of sample. The resulting difference spectra were of high quality in the high frequency regions. However, this technique is not sufficient, due to the non-linearities of the water absorbances below 1000 cm^{-1} , to observe signals in the low frequency region of the spectrum. As a result of this, other methods of handling water absorbances need to be considered.

An obvious solution, and one with which we have had good success, consists of physically removing the majority of the bulk solvent water from the sample. This method has been used previously to obtain high quality light-induced infrared difference spectra of bacteriorhodopsin[17-21], the photosynthetic bacterial reaction center[22] and photosystem II[23-27]. However, drying biological samples raises some very legitimate biochemical questions regarding physiological relevance. Careful control experiments must be performed to ensure that the samples retain their biochemical integrity after water removal. These control experiments may consist of UV-visible measurements, electron paramagnetic resonance, or any other technique that has been used to characterize the enzyme system in its fully hydrated state. If the samples maintain their activity after partial drying, then this technique allows spectroscopic access to the entire mid-infrared region of the spectrum, including, in particular, the region of metal-ligand vibrations below 1000 cm^{-1} . There are several different ways that controlled partial dehydration of protein samples can be accomplished.

The easiest method to achieve partial dehydration of samples consists of depositing the sample on to a suitable substrate material (the choice of suitable substrate materials will be covered in a subsequent section), and then drying it under a stream of

dry nitrogen gas. In buffers that contain no hygroscopic materials such as sucrose, glycerol, or ethylene glycol (common components of biochemical buffering systems), almost complete dryness can be obtained this way (see Figure 4-4), based upon the relative intensities of the O-H stretching mode at 3400 cm^{-1} and the so-called amide I protein backbone mode at 1650 cm^{-1} . However, many enzymes, when desiccated, undergo extensive structural perturbations[6], which may effect their catalytic chemistry. If control experiments show that the samples cannot handle arbitrary levels of dehydration, then it may be necessary to remove the water in the sample in a highly controlled manner, so that a balance can be achieved between enough dehydration to ensure spectroscopic utility, while maintaining a high enough level of hydration to ensure biochemical integrity.

We have found that if a small amount of hygroscopic materials (such as those named above) are present in the sample, then the samples can usually be dried to a point where the infrared spectra are spectroscopically acceptable, yet the proteins retain enough water whereby they exhibit native biological activity (Figure 4-4). In our experiments it has been found that 150mM sucrose in the drying buffer, allows enough water to be removed to reduce the water absorptions to an acceptable level, yet, as is shown in the next chapter, control EPR experiments exhibit all of the characteristic signals associated with an intact reaction center. It is important to determine a set of quantitative benchmarks that can be used to evaluate sets of samples with regard to their levels of hydration in order to ensure that the spectra acquired show high levels of reproducibility. In the case of bacteriorhodopsin, it was determined[28] that the integrated area of the

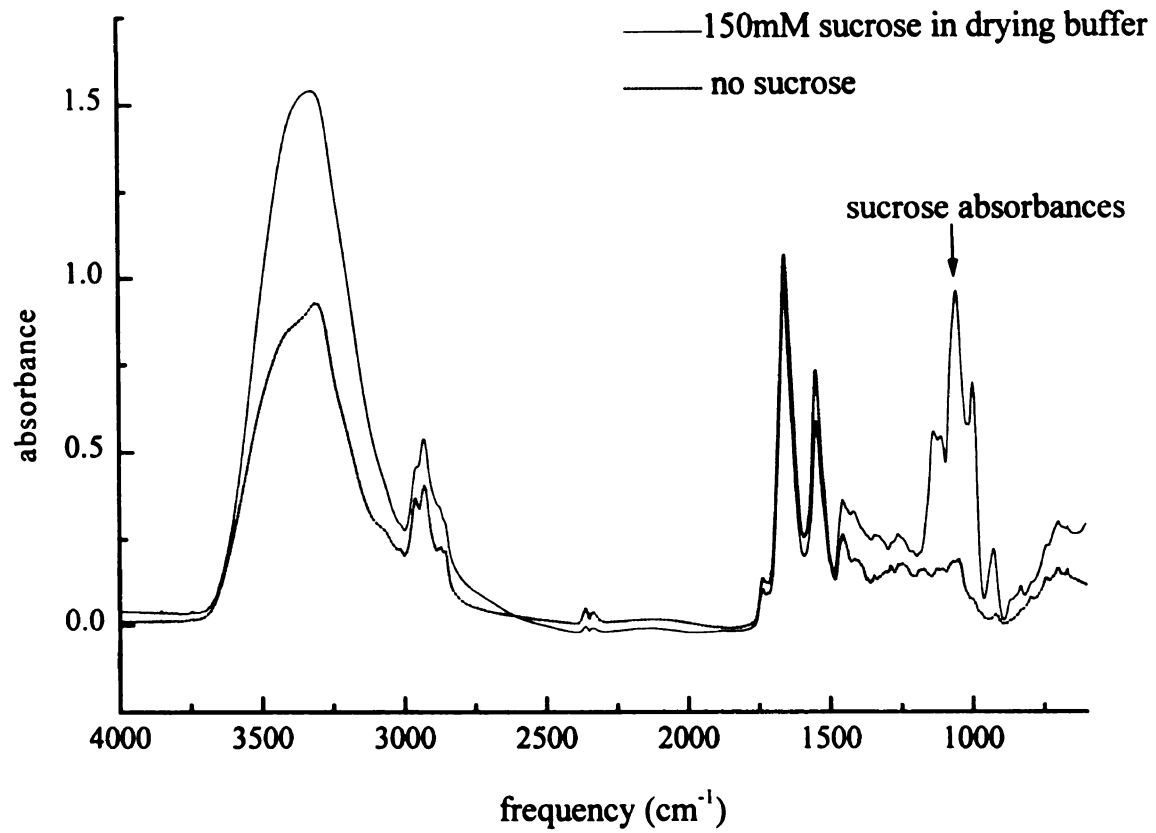


Figure 4-4: Partially hydrated films of PSII samples, with and without sucrose in the drying medium. Sample temperature: 25 °C.

water peak at 3300 cm^{-1} should be at least 6 times the integrated area of the amide I protein mode at 1650 cm^{-1} in order for the protein to be fully competent to undergo a photochemical reaction. In our case, we routinely achieve a 10:1 ratio of the integrated area of the same peaks. Under these conditions, the water absorbances are well within the linear range of the detector, and thus we are able to acquire high-quality, light induced difference spectra of Photosystem II across the entire mid-infrared range.

Detectors

A critical issue that must be addressed when performing FTIR spectroscopy on biological systems concerns the choice of detectors. This is particularly true when one is interested in detecting low frequency vibrations. There are a wide variety of infrared-sensitive detectors available, and with the development of semiconductor detectors, namely the mercury-cadmium-telluride (MCT) detectors, it is possible for investigators to acquire data across the entire infrared spectrum with great sensitivity. Additionally, with sufficient signal averaging, random noise can be reduced to levels where the small signals from the enzyme system can be observed.

Infrared detectors are commonly evaluated in terms of their specific detectivity, or, D^* values[5]. The sensitivity of a given infrared detector is usually expressed in terms of the noise-equivalent power (NEP)

$$\text{NEP} = \frac{V_n}{R_v} W \cdot \text{Hz}^{-\frac{1}{2}}$$

In this expression V_n is the root mean square (rms) of the detector noise voltage in volts- $\text{Hz}^{-1/2}$, and R_v is the voltage responsivity of the detector to signals in volts/watt. The specific detectivity, or D^* , of a detector is given by

$$D^* = \frac{(A_D)^{\frac{1}{2}}}{NEP} \text{ cm} \cdot \text{Hz}^{\frac{1}{2}} \cdot \text{W}^{-1}$$

where A_D is the area of the detector element. This expression factors into the overall expression for the signal to noise ratio (SNR) of the FTIR instrument which is

$$\begin{aligned} SNR &= \frac{U_{\bar{\nu}}(T) \cdot \Theta \cdot \Delta\bar{\nu} \cdot t^{\frac{1}{2}} \cdot \xi}{NEP} \\ &= \frac{U_{\bar{\nu}}(T) \cdot \Theta \cdot \Delta\bar{\nu} \cdot t^{\frac{1}{2}} \cdot \xi \cdot D^*}{A_D^{\frac{1}{2}}} \end{aligned}$$

where $U_{\bar{\nu}}(T)$ is the spectral energy density, Θ is the throughput of the system, $\Delta\bar{\nu}$ is the resolution, t is the time, and ξ is an instrumental efficiency factor. This expression clearly shows that the signal-to-noise ratio of a given spectrum depends linearly upon the D^* value of the detector, the resolution, $\Delta\bar{\nu}$, and the throughput, Θ . It is, therefore, in the best interest of the spectroscopist to optimize these values as much as is possible in order to acquire the highest quality spectra in the shortest amount of time.

There are several types of detectors available for FTIR measurements. The most common type of detector with the most linear response function are the “thermal” type detectors. These detectors operate by sensing the change in temperature of an absorbing material as more (or less) infrared radiation impinges upon it. The most common class of this type of detector is called a pyroelectric bolometer. This type of detector utilizes a

material for its sensing element that exhibits a change in its electrical polarization when its temperature changes. Deuterated triglycine sulfate (DTGS) is one of the more common materials used in this type of detector. These detectors have the advantage that they can be operated at room temperature, and that they display highly linear responses to varying intensities of incident radiation. However, for biological spectroscopy, these detectors are of limited utility because they are not highly sensitive ($D^* = \sim 10^7 - 10^8$), thus making the detection of small experimental signals over large background signals difficult.

Biological infrared spectroscopy underwent a renaissance with the advent of semiconductor-type quantum detectors. This class of highly sensitive detectors allowed for the detection of minute signals, in otherwise highly absorbing samples. These detectors, of which the mercury-cadmium-telluride (MCT) detectors are the most popular, have D^* values ranging from 10^9 to 10^{11} and higher. These detectors operate by using a ternary semiconductor detector element whose bandgap corresponds to the energies present in infrared radiation. Because of the large background of infrared radiation present at room temperature, these detectors must be cooled, usually to liquid nitrogen temperatures (77K), to eliminate thermal background contributions to the detected signals. The wavelengths to which these detectors respond depends upon the specific stoichiometric ratio of the constituent elements. However, an MCT detector optimized for low frequencies (peak response at $\sim 500\text{cm}^{-1}$) exhibits a D^* value approximately an order of magnitude lower than an MCT detector that is optimized for higher frequency responses.

Another choice for low frequency IR detection is the liquid helium cooled quantum detector. This technology relies upon a germanium or a doped germanium detector element, and operates by the same principles as the MCT type detector. A key difference is the need for a cooling system that is able to maintain the detector element at a temperature below that readily attainable with liquid nitrogen as the coolant. This necessitates the use of liquid helium and the associated hardware necessary for a helium refrigeration system. Because of this, this type of detector is considerably more expensive than the simpler nitrogen cooled MCT type detectors. Because investigations of low frequency modes in the infrared spectra of biomolecules is still in its infancy, these detectors have not been tested for their usefulness for these studies. However, they do have comparable D^* values to MCT detectors, and the fact that they respond to radiation further into the far-IR than any MCT detector, shows their potential utility for these types of studies.

Window/Substrate Materials

A question that needs to be addressed when performing any type of spectroscopy regards the types of window materials through which the interrogating radiation must pass. The material must not only be transparent to the radiation, but must also pass enough of the radiation to ensure that a high enough optical throughput is attained to achieve suitable signal-to-noise ratios in the resulting spectra. There are numerous window materials available to the infrared spectroscopist. However, when the spectroscopist is interested in utilizing samples that contain water *and* is interested in observing the low frequency region of the spectrum, then the list of candidate

materials that meet this criteria becomes limited. Additionally, because there is a lot of useful information in the high-frequency region of infrared difference spectra, it would be beneficial to use a material that has a clear window of transmission from 2000 cm^{-1} down to a low frequency cutoff that will ensure that all of the vibrational modes of interest are detectable.

A list of the common infrared window materials, the frequencies of radiation that they pass, and their water solubility characteristics are listed in table 4-3. From this table there are several materials that fit the criteria for transmitting radiation below 1000 cm^{-1} , as well as showing limited or no solubility in water. Silver halide salts are a class of materials that have been used successfully in several different IR experiments. The two most common materials are silver chloride and silver bromide. These materials transmit radiation from the visible region of the electromagnetic spectrum to 435 cm^{-1} and 285 cm^{-1} respectively. They both have a tendency to cold flow (physically distort), and they are also prone to photoreduce upon exposure to UV light, so their transmission properties tend to degrade over time. This photoreduction process needs to be considered when samples are deposited upon the surface of one of these materials. The reduction potential of Ag^+ is such that some reactive intermediates in certain enzymatic processes may react with the silver ions in the substrate rather than reacting in their normal physiologically relevant manner. Proper control experiments must be performed to ensure that this is not an issue. If these side reactions are, in fact, found to not play a role in the experiment, then the silver halide salts are good materials for these types of experiments. Their IR transmission properties coupled with the visible light they can transmit (for light induced experiments) make them very useful for light induced FTIR experiments. Zinc selenide

Table 4-3 Properties of Infrared Window Materials

Material	Water Solubility (g /100g H ₂ O, 20°C)	Transmission Range (cm ⁻¹)
NaCl	36.0	40,000-625
KBr	65.2	40,000-400
AgCl	0.00015	25,000-435
AgBr	0.000012	20,000-285
ZnSe	insoluble	10,000-500
CdTe	insoluble	5,000-320
Ge	insoluble	5,000-600
Polyethylene	insoluble	625-30
Diamond	insoluble	1,700-33

and cadmium telluride are two materials that have not enjoyed widespread use for biological FTIR experiments, due in part to their higher cost and the availability of cheaper materials that show similar transmission properties. Germanium is a material that is suitable for some studies, yet its high index of refraction leads to greatly attenuated throughput of the IR radiation. It has served the light-modulated difference spectroscopy field well in that it passes IR radiation (albeit at levels too low for some purposes), yet it completely blocks visible light. Most FTIR spectrometers have as part of their design, a helium-neon laser that is coaxial with the IR beam. This laser light, which is used to provide an internal frequency standard to the instrument, must be prevented from impinging upon the sample if the reaction that is to be studied is going to be induced by a controlled source of visible light. Germanium is often the material of choice to perform as a visible light filter since it still passes the IR radiation. One serious shortcoming of germanium is that it does not transmit IR radiation below 600cm^{-1} . Many metal-ligand vibrations fall below this cutoff, thus making germanium a liability for these studies.

Polyethylene and silicon are two materials that appear attractive for low-frequency work, yet they are restricted in their utility due to their limited transmission range and, in the case of silicon, the high index of refraction.

Temperature Control

Once the sample conditions are under control it is crucial to evaluate the method by which the temperature of the sample will be controlled. It has been shown that infrared spectra of aqueous systems display large baseline distortions when the temperature is not maintained at a constant value[3]. Additionally when two spectra, of the same partially

dehydrated protein film, taken immediately consecutively to one another, experience temperature drifts of as little as 0.3°C , large differential signals appear in the difference spectrum (see Figure 4-5). Care must be taken when evaluating data, as these “thermal bands” can easily be mistaken for real peaks.

There are several technologies available to achieve a high level of temperature control with a sampling system. Closed-cycle helium refrigeration systems allow samples to be cooled to 1-2K. These systems display very stable temperatures, yet they do not allow for easy sample switching. These cryostat systems place the sample into a high-vacuum environment to reduce or eliminate thermal contact with the ambient temperatures. Each time a sample is removed this vacuum must be broken, and reestablished before a new set of data, with a new sample, can be acquired. This greatly increases the amount of time necessary to achieve a given signal-to-noise ratio in a final spectrum. It is not uncommon for spectra from multiple samples to be averaged together, thus a system whereby one can change samples easily and quickly is desirable. In addition to this, the windows on the refrigeration unit must be able to not only pass infrared radiation, but also have the mechanical strength necessary to withstand the great pressure differential between the high vacuum that surrounds the sample and the atmospheric pressure outside of the apparatus. Typically more brittle materials, such as calcium fluoride, are used, but, because of their IR transmission properties, they are not of any use for studies of low-frequency modes of vibration. The materials that are capable of transmitting the lower frequencies are typically softer, and thus very thick windows are

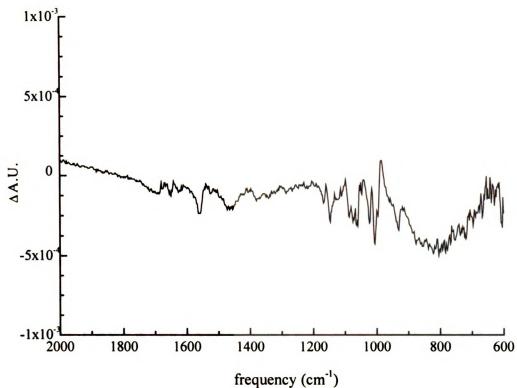


Figure 4-5: Difference bands induced by temperature fluctuation of partially hydrated film of photosystem II. The spectrum was acquired by cooling the sample to 200K, acquiring one spectrum (500 scans), raising the temperature 0.2 °C, and acquiring a second spectrum (500 scans). The ratio of the two spectra resulted in the displayed difference spectrum.

necessary to meet the mechanical specifications. Thicker windows reduces the overall throughput on a system, thereby also degrading the signal-to-noise ratio of the acquired data.

A system that we have designed to accommodate our experimental needs is presented in Figure 4-6. It maintains a high level of temperature stability, yet allows for facile sample changing, while also allowing for high optical throughput. The system is based upon the simple concept of flowing a stream of gas at a precisely controlled temperature around the sample. In our system, nitrogen gas, at room temperature, is passed through two heat exchangers to cool the gas to a temperature below the desired target temperature. The first heat exchanger uses an acetone/dry ice bath, the second uses liquid nitrogen. The gas is then passed through a glass dewar transfer arm, that contains a nichrome heating element that is used to heat the gas to the desired temperature in a controlled manner. The gas, now at the desired temperature, then flows into the sampling chamber that is located in the sample compartment of the FTIR spectrometer. The sampling chamber is a simple aluminum box, with windows to allow the IR radiation to pass (Figure 4-7). The first window is a bandpass filter (either germanium or a custom dielectric-layer bandpass filter discussed later) that acts to block the coaxial helium-neon laser beam, while still transmitting the IR radiation in the frequency range of interest. The second window is made of silver chloride. Care is taken to place the actual enzyme sample at the focal point of the IR radiation. The sample, a partially-dehydrated film of protein, is on a silver chloride window, that is sealed with another silver chloride window. Incorporated into the sample window holder is a thermocouple used to monitor

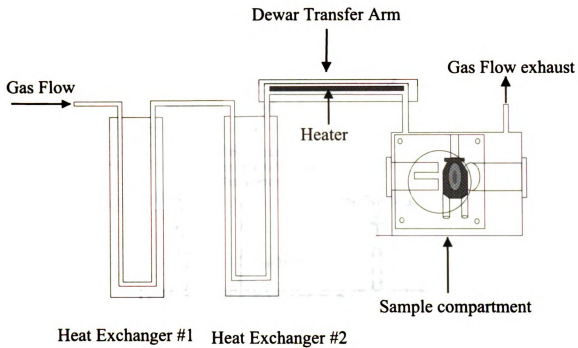


Figure 4-6: Temperature control system for low temperature FTIR experiments.

TOP VIEW

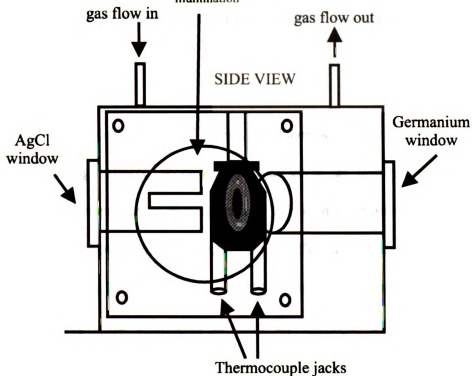
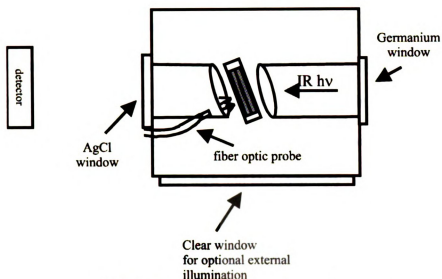


Figure 4-7: Sample compartment for low-temperature FTIR experiments.

the temperature of the sample. The temperature is controlled controlled to $\pm 0.1^{\circ}\text{C}$ by a LakeShore Cryogenics Model 321 temperature control unit. With this level of control, the thermal contributions to the difference spectra are eliminated, and the design of the system allows large numbers of samples to be investigated in a relatively short period of time. Most importantly, there is no limit upon the choice of window materials used on the sampling chamber. Therefore, the high and low frequency cutoffs of the acquired data are not limited by the temperature control system. In order to induce the reaction with actinic light, a fiber optic probe is positioned next to the sample holder. A 150W halogen bulb, filtered to remove IR components, can provide 20mW of visible light to the sample.

Conclusions

With the systems described above, we have developed ways whereby we can acquire data using infrared spectroscopy, that gives us information about the low frequency vibrations present in photosystem II. This is the first time that information such as this has been reported, and the techniques developed here show great potential for application not only to photosystem II, but to metalloenzymes in general. We are currently adapting these techniques to study the binuclear iron-copper center of the respiratory protein cytochrome c oxidase. Other systems for which this technique may be useful include methane monooxygenase, ribonucleotide reductase, and the manganese catalase systems. Studies of these systems have been limited, until now, to relatively indirect methods of spectroscopy. The information acquired here is direct, in that it can

confirm the presence or lack of certain specific chemical bonds during the various steps of the catalytic cycles of the enzymes.

LIST OF REFERENCES

1. Gardner, M.T., Deinum, G., Kim, Y., Babcock, G.T., Scott, M.J., and Holm, R.H., *Inorg. Chem.*, 1996. **35**: p. 6878.
2. Arrondo, J.L.R., Muga, A., Castresana, J., and Goni, F.M., *Prog. Biophys. Molec. Biol.*, 1993. **59**: p. 23.
3. Rahmelow, K. and Hubner, W., *Appl. Spec.*, 1997. **51**: p. 160.
4. Fringeli, U.P. and Gunthard, H.H., in *Membrane Spectroscopy*, E. Grell, Editor. 1981, Springer: Berlin. p. 270.
5. Griffiths, P.R. and de Haseth, J.A., *Fourier Transform Infrared Spectrometry*. 1986, New York: Wiley-Interscience.
6. Koenig, J.L. and Tabb, D.L., *Infrared Spectra of Globular Proteins in Aqueous Solution*, in *Analytical Applications of FT-IR to Molecular and Biological Systems*, J.R. Durig, Editor. 1980, D. Reidel Publishing Co. p. 241.
7. Mantele, W., *Infrared Vibrational Spectroscopy of the Photosynthetic Reaction Center*, in *The Photosynthetic Reaction Center*, J. Deisenhofer and J.R. Norris, Editors. 1993, Academic Press: New York. p. 239.
8. Navedryk, E., Andrianambinintsoa, S., Berger, G., Leonhard, M., Mantele, W., and Breton, J., *Biochim. Biophys. Acta*, 1990. **1016**: p. 49.
9. Navedryk, E., Leonhard, M., Mantele, W., and Breton, J., *Biochemistry*, 1990. **29**: p. 3242.
10. Noguchi, T., Ono, T., and Inoue, Y., *Biochim. Biophys. Acta*, 1995. **1228**: p. 189.
11. Noguchi, T. and Inoue, Y., *FEBS Letters*, 1995. **370**: p. 241.
12. Noguchi, T. and Inoue, Y., *J. Biochem.*, 1995. **118**: p. 9.

13. Steenhuis, J.J. and Barry, B.A., *J. Am. Chem. Soc.*, 1996. **118**: p. 11927.
14. Hienerwadel, R., Boussac, A., Breton, J., and Berthomieu, C., *Biochemistry*, 1996. **35**: p. 15447.
15. Hienerwadel, R. and Berthomieu, C., *Biochemistry*, 1995. **34**: p. 16288.
16. Berthomieu, C. and Boussac, A., *Biochemistry*, 1995. **34**: p. 1541.
17. Maeda, A., Sasaki, J., Shichida, Y., Yoshizawa, T., Chang, M., Ni, B., Needleman, R., and Lanyi, J.K., *Biochemistry*, 1992. **31**: p. 4684.
18. Rothschild, K.J., He, Y.-W., Sonar, S., Marti, T., and Khorana, H.G., *J. Biol. Chem.*, 1992. **267**: p. 1615.
19. Bousche, O., Braiman, M., He, Y.-W., Marti, T., Khorana, H.G., and Rothschild, K.J., *J. Biol. Chem.*, 1991. **266**: p. 11063.
20. Braiman, M., Mogi, T., Stern, L., Hackett, N.R., Chao, B.H., Khorana, H.G., and Rothschild, K.J., *Proteins: Struct. Func. Gen.*, 1988. **3**: p. 219.
21. Engelhard, M., Gerwert, K., Hess, B., Kreutz, W., and Siebert, F., *Biochemistry*, 1985. **24**: p. 400.
22. Mantele, W., Navedryk, E., Tavitian, B.A., Kreutz, W., and Breton, J., *FEBS Letters*, 1985. **187**: p. 227.
23. MacDonald, G.M. and Barry, B.A., *Biochemistry*, 1992. **31**: p. 9848.
24. MacDonald, G.M., Bixby, K.A., and Barry, B.A., *Proc. Natl. Acad. Sci.*, 1993. **90**: p. 11024.
25. MacDonald, G.M., Steenhuis, J.J., and Barry, B.A., *J. Biol. Chem.*, 1995. **270**: p. 8420.
26. Bernard, M.T., MacDonald, G.M., Nguyen, A.P., Debus, R.J., and Barry, B.A., *J. Biol. Chem.*, 1995. **270**: p. 1589.
27. Tavitian, B.A., Navedryk, E., Mantele, W., and Breton, J., *FEBS Letters*, 1986. **201**: p. 151.
28. Roepe, P., Ahl, P.L., Gupta, S.K.D., Herzfeld, J., and Rothschild, K.J., *Biochemistry*, 1987. **26**: p. 6696.

Chapter 5

LOW FREQUENCY MODES IN THE LIGHT-INDUCED FTIR DIFFERENCE SPECTRUM OF PHOTOSYSTEM II

Abstract

We report the first light-induced FTIR difference spectra of photosystem II which include data from the low frequency ($600\text{-}1000\text{ cm}^{-1}$) region of the spectrum. This is the region where metal-ligand vibrations and metal-substrate vibrations are expected to be observed. These spectra, which show the vibrational differences as the enzyme is advanced from the S_1Q_A state to the $S_2Q_A^-$ state, display a multitude of vibrational modes that are attributable to 1) amino acid vibrations that are perturbed by the advancement of the redox state of the enzyme, 2) protein backbone modes, and 3) metal-ligand species whose bonding interactions are altered upon advancing the manganese cluster from the S_1 state to the S_2 state. Both sub-chloroplast BBY-type particles and highly-refined reaction center core preparations were utilized for these studies. Upon manganese depletion of the samples, the difference spectra showed reproducible changes in the $\sim 630\text{ cm}^{-1}$ region of the spectrum where manganese-substrate bonds are expected to appear. Additionally, when the samples were induced to oxidize water, in the presence of ^{18}O -labelled water, reproducible changes of the $\sim 632\text{ cm}^{-1}$ peak were observed. The frequency to which the vibration is expected to shift, based upon model compound studies, is currently below the range of our instrumental capabilities. Modifications are planned to extend the low-

frequency capability of the instrumentation, which will allow the observation of modes down to 350 cm^{-1} . Additionally, photosystem II samples which display the $g=4.1$ EPR signal of the S_2 state of the enzyme were studied. Vibrational differences in the low frequency region of the spectrum were observed, which is consistent with the occurrence of a structural rearrangement of the manganese cluster under the conditions in which the $g=4.1$ EPR signal is exhibited.

Introduction

Photosynthesis is the process whereby higher plants, cyanobacteria, and some bacteria harvest light, and use that energy to separate charges across cellular membranes. Ultimately the energy is used to drive metabolic processes. The infrastructure that all photosynthetic organisms utilize to generate this initial charge separation is universal. Energy, in the form of light, is harvested and used to create a charge separated state between a dimer of chlorophyll molecules (the “special pair”), and a quinone molecule, Q_A . The mechanism by which the positively charged “hole” on the special pair of chlorophyll molecules is filled differentiates non-oxygen evolving photosynthetic bacteria, from those organisms that evolve oxygen, such as cyanobacteria and higher plants. In the non-oxygen evolving systems, where the photosynthetic enzyme is called the bacterial reaction center, the hole on the special pair of chlorophyll molecules is filled by reducing equivalents from cytochrome *c* molecules. In cyanobacteria and higher plants, the enzyme that performs the initial steps of photosynthesis is known as Photosystem II (PSII). In PSII, the hole on the chlorophyll dimer (called P680), is filled

by an electron which originates from the oxidation of a solvent water molecule. This oxidation of water results in the production of molecular oxygen (see Figure 5-1).

In 1937, it was determined that the element manganese was intimately involved in the water oxidation process[1]. In these studies it was shown that, if manganese were removed from the growth media of plants and algae, the organisms were no longer capable of oxygen evolution. If the manganese was replaced, oxygen evolution was rapidly restored. Over time, the debate regarding the stoichiometry of manganese in PSII has converged, and it is widely agreed upon that there are four manganese atoms per photosystem II reaction center. In addition to the four manganese ions, it is known that Ca^{2+} and Cl^- are essential cofactors; their absence abolishes oxygen evolution.(For a comprehensive review of PSII, see [2-4]). A cartoon that depicts the primary photochemical events of PSII is shown in Figure 5-2. Upon photoexcitation, an electron is ejected from the special pair of chlorophyll molecules called P680. This electron travels through a pheophytin molecule, to the primary plastoquinone molecule Q_A , and then to a second plastoquinone molecule Q_B , which can accommodate two electrons. Q_B , once doubly reduced, dissociates to the stromal side of the chloroplast membrane. The reducing equivalents on this quinone molecule are ultimately used in the reduction of NADP^+ to NADPH. P680^+ is one of the strongest oxidants known in biological systems ($\sim 1.1\text{eV}$). Once oxidized, it is immediately reduced by an electron from a redox active tyrosine residue of the protein backbone, Y_Z , to give a neutral tyrosine radical, $\text{Y}_\text{Z}^\bullet$. This radical is then reduced by electrons derived from a substrate water molecule that is interacting with the manganese cluster.

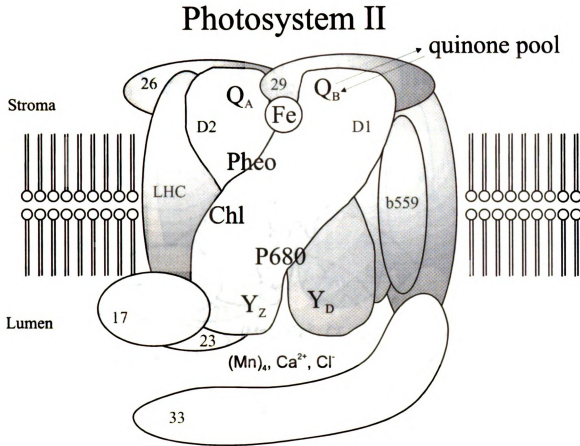


Figure 5-1: Schematic of the Photosystem II reaction center. Numbers are approximate molecular weights of the constituent polypeptides. See text for description of components.

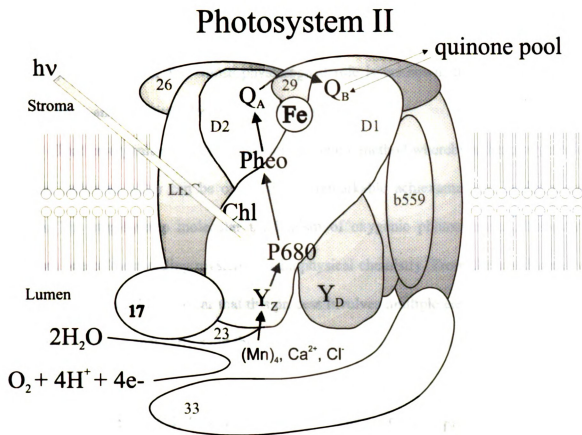


Figure 5-2: Schematic depicting the primary photochemical events in photosystem II.

After four

released a

active tyr

radical fo

TH

sink as s

action. T

remains c

of water

require th

(1) 2

this proc

substrate

currently

S

played b

oxygen

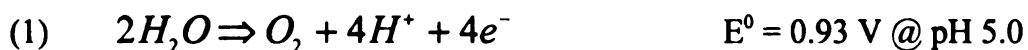
subjecte

oxygen

on ever

After four electrons are removed from the manganese cluster, molecular oxygen is released and the manganese cluster is reduced back to the S_0 state. There is another redox active tyrosine residue, Y_D , whose physiological role is unknown, that is stable in the radical form, and exhibits a dark stable EPR signal.

That an organism has developed an enzymatic method whereby a thermodynamic sink as stable as water can be oxidized is a remarkable achievement of evolutionary action. The step-by-step molecular mechanism of oxygenic photosynthesis, however, remains one of the puzzling mysteries of biophysical chemistry. From the stoichiometry of water oxidation (1) it is clear that this process involves multiple electrons, which must require the enzyme that carries out this



this process to exert considerable biochemical and physiological control. Whether the substrate water is oxidized in a sequential, step-wise fashion, or in one concerted step, is currently the subject of much debate.

Several key experiments have provided critical insight into the specific role played by manganese ions in the water oxidation process. In 1969 an experiment where oxygen evolution from chloroplasts of plants was measured as the samples were subjected to short, saturating flashes of light[5]. It was noted that there was a burst of oxygen released upon the third flash given to the dark-adapted samples, and subsequently on every fourth flash thereafter. This observation led Bessel Kok, to propose the Kok

cycle for C

there are

These state

the most r

samples. p

state is rea

process. g

thinking r

specific, r

manganese

over the o

An

occurred i

dark adap

evolution,

This behav

"multiline

gauss, and

manganese

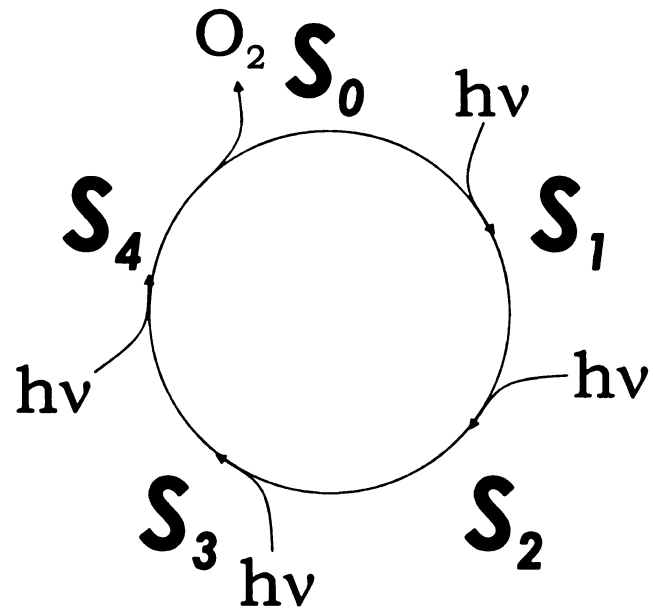
line broad

interaction

cluster. I

cycle for oxygen evolution [6](Figure 5-3). This model for the “S-states” proposes that there are five distinct oxidation levels involved in photosynthetic oxygen evolution. These states, labeled S_0 - S_4 , represent different redox levels of the enzyme, with S_0 being the most reduced form of the enzyme, and S_4 being the most oxidized. Dark adapted samples, primarily in the S_1 state, are consecutively oxidized by one electron until the S_4 state is reached. At this point water is oxidized to dioxygen in a concerted four electron process, giving back the S_0 state with the release of O_2 . The Kok model inspired much thinking regarding the exact mechanism of oxygen evolution. However, with a lack of specific, molecular-level information regarding the structure and geometry of the manganese cluster, little evidence was available to prove the feasibility of any one model over the others.

Another significant advance in the study of oxygen evolution in photosystem II, occurred in 1981 when Dismukes and co-workers reported observing an EPR signal from dark adapted PSII samples given a single flash of saturating light [7]. As with oxygen evolution, the amplitude of this signal also exhibited a periodic four flash dependence. This behavior is indicative of the EPR signal arising from the S_2 state of the enzyme. This “multiline” signal ($g=1.98$ @ 9 GHz) consists of 18-22 lines, each separated by 75-90 gauss, and was assigned to a mixed-valence cluster of at least two exchange coupled manganese atoms (Figure 5-4). When ^{17}O -labeled water was used as the substrate, slight line broadening in the multiline signal was observed[8] which was attributed to the interaction between the $S=5/2$ ^{17}O nucleus and the $S=1/2$ spin state of the manganese cluster. In PSII samples treated with the substrate analog NH_3 , the multiline signal was



Kok Cycle

Figure 5-3: Kok model for oxygen evolution.

$\frac{dx''}{dx}$

Figure
temper
illumin
Micro

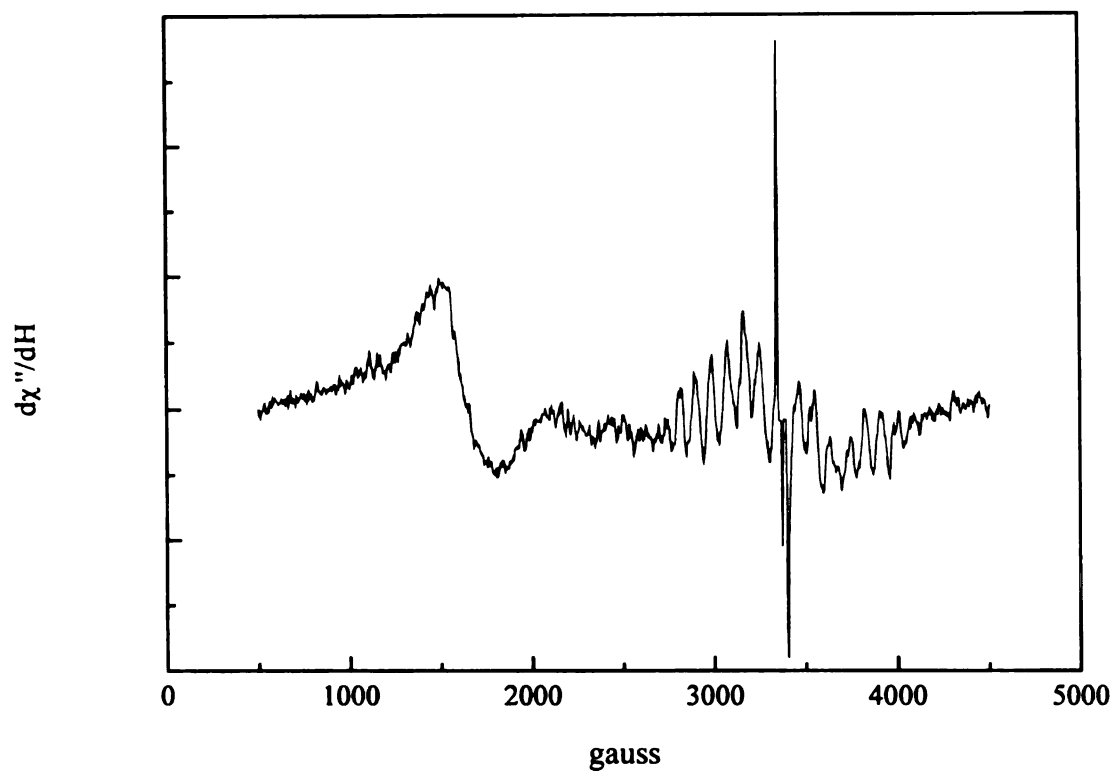


Figure 5-4: Multiline EPR spectrum of BBY particles, 200K illumination. 8K sample temperature. Spectrum is the difference between a EPR spectrum acquired after illumination at 200K, and the EPR spectrum of the sample before illumination. Microwave power: 2 mW, 20 gauss modulation amplitude, gain = 1×10^5 .

alterec

manga

being

oxidati

manga

g=4.1.

signal.

which

switch

widely

(III.IV

the org

OEC) (

ray Ab

Structu

provide

ion[11

vigoro

reache

second

or a N

altered, which suggests a direct interaction between the ammonia molecule, and the manganese cluster[9, 10]. Both of these studies implicate the manganese ensemble as being both the site of substrate binding as well as the site of subsequent substrate oxidation.

Under conditions of Cl^- depletion, or substitution with F^- , NH_3 or Sr^{2+} , the manganese cluster exhibits an EPR signal attributed to the S_2 state that is observed at $g=4.1$. The intensity of this signal appears at the expense of intensity of the S_2 multiline signal. The g -value at which it appears is consistent with an $\text{S}=3/2$ or $\text{S}=5/2$ spin state, which implies that a magnetic reorganization must occur for the manganese cluster to switch between displaying the $\text{S}=1/2$ multiline signal and the $g=4.1$ signal. Because it is widely agreed that the oxidation states of the individual manganese ions in the S_2 state are (III,IV,IV,IV), the $g=4.1$ signal most likely arises from a $\text{S}=5/2$ state.

Other techniques that have contributed to the advancement in the understanding of the organization of the manganese cluster (also called the Oxygen-Evolving Complex, or OEC) of photosystem II are the various X-ray absorption spectroscopies, particularly X-ray Absorption Near Edge Spectroscopy (XANES) and Extended X-ray Absorption Fine Structure spectroscopy (EXAFS). EXAFS, when applied properly, has the potential to provide information regarding the structure and coordination environment of a metal ion[11-15]. While the validity of the various experiments that have been performed are vigorously debated within the EXAFS community, one point of agreement that has been reached is the existence in the manganese cluster of a metal-metal distance of 2.7\AA and a second distance vector 3.3\AA in length. Whether this 3.3\AA distance is a Mn-Mn distance or a Mn- Ca^{2+} distance is not known. The 2.7\AA distance, when compared to data acquired

from

ator

the

that

man

(to a

samp

respe

states

eject

set fr

about

from model compound studies, is diagnostic of a Mn_2O_2 structure, where the two oxygen atoms form a bridge between the two manganese atoms in a di- μ -oxo arrangement. On the basis of these measurements and the EPR results, a model for the OEC was proposed that consisted of two di- μ -oxo dimers (the so-called “dimer of dimers” model) of manganese atoms (to accommodate the 2.7 Å distance), linked by a mono- μ -oxo bridge (to accommodate the 3.3 Å distance)[16]. Further experiments on layered, oriented PSII samples, showed evidence for an open “C” geometry of the two di- μ -oxo cores with respect to one another (Figure 5-5) [17].

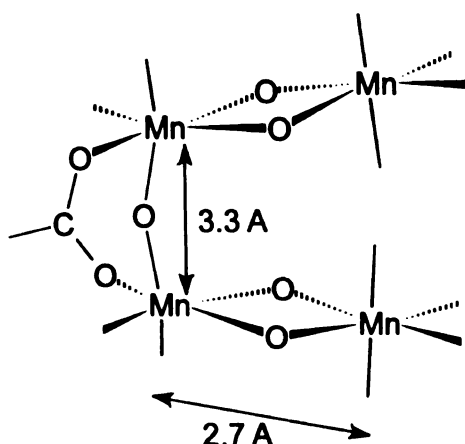


Figure 5-5: Open “C” model for the manganese cluster of Photosystem II

XANES is a technique that can be used in the determination of the oxidation states of metal atoms[18, 19]. By examining the energy of the X-ray photon necessary to eject an inner-shell electron from a metal atom, and then comparing that energy to a data set from model compounds of known oxidation level, it is possible to draw conclusions about the oxidation states of metal centers in proteins. While these experiments also are

not

man

spec

ques

som

som

oxid

Figure
water

the su

disap

not without controversy, there are several points regarding the oxidation levels of the manganese cluster in the various S-states that are agreed upon by a majority of the X-ray spectroscopy practitioners[20]. These oxidation schemes are depicted in Figure 5-6. A question remains as to whether manganese is oxidized on the S_2 to S_3 transition, or if some organic cofactor is oxidized to generate an organic radical. Manganese XANES, in some studies, does not show the characteristic small edge shift associated with metal oxidation[20]. However, the data acquired from these experiments, and more particularly,

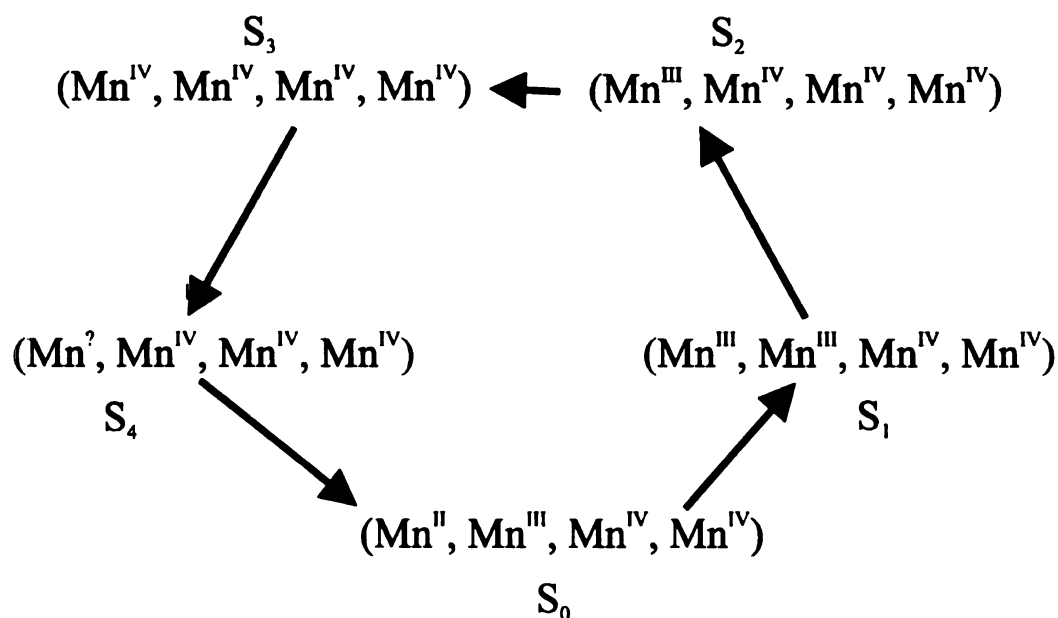


Figure 5-6: Scheme of oxidation states of manganese cluster during the catalytic cycle of water oxidation.

the subsequent treatment of these data, is subjective, and small subtle shifts can appear or disappear depending upon the specific data treatment method utilized[21]. Under certain

non-oxyg

observed

fluoride[2

the S₂ to

effective

that this

induced

A

OEC ha

incorpor

compre

Figure 1

a hydro

four m

acts up

result i

and th

other

anoth

level.

dime

of S=

of S=

non-oxygen evolving conditions, a 90-180 gauss EPR signal centered at $g=2$ can be observed in PSII samples that have been calcium depleted, or substituted with fluoride[22-24]. Some have attributed this signal to a histidine residue that is oxidized on the S_2 to S_3 transition in lieu of manganese [25, 26]. However, this assignment has been effectively challenged by Britt and co-workers who, using pulsed EPR methods, showed that this 90-180 gauss radical can be assigned to tyrosine Z in an altered environment, induced by the removal of calcium[27].

All of the information regarding the possible structure and oxidation states of the OEC have been assimilated in a model for oxygen evolution[28]. This model attempts to incorporate the available structural and chemical information regarding the OEC, into one comprehensive mechanism for water oxidation. A schematic of the model is presented in Figure 5-7. A key aspect of the model is that the redox active tyrosine residue, Y_Z , acts as a hydrogen atom abstractor. In the S_0 state, substrate water is bound to the OEC, whose four manganese atoms are at the (II,III,IV,IV) or (III,III,III,IV) oxidation level. Y_Z then acts upon the substrate water, abstracting a hydrogen atom from the bound water. The result is the S_1 state, in which the manganese cluster has been oxidized by one electron, and the substrate now consists of a bound hydroxide ligand oriented cofacially to the other substrate water molecule. Upon the next oxidation, which results in the S_2 state, another hydrogen atom is abstracted, leaving the manganese in a (III,IV,IV,IV) oxidation level. This is the state that gives rise to the multiline EPR signal. A manganese (III, IV) dimer in which the two manganese are antiferromagnetically coupled, has an overall spin of $S=1/2$. An antiferromagnetically coupled (IV,IV) dimer of manganese atoms has a spin of $S=0$. Coupling these two spin states gives an overall spin state of $S=1/2$, which is the

spin sta

observe

reorgan

dimer c

an oxo

of the

necessi

on the

the tyro

pair, w

the din

the ope

oxo/hy

sponta

formal

The ro

ferryin

Sr^{2+} is

while

This

PSII

spin state attributed to the manganese ensemble when the multiline EPR signal is observed[20]. An interesting proposal in this model is that, in order to avoid large reorganization energies, Y_Z must only abstract hydrogen atoms from the top half of the dimer of dimers cluster. Upon initial formation of the S_2 state, a species that is formally an oxo species is generated, while there is still a bound water molecule on the bottom half of the dimer. However, due to the basicity of this terminal oxo group, or due to the necessity for the cluster to remain charge balanced, a proton from the substrate molecule on the bottom dimer moves to the oxo moiety on the top half of the dimer. This allows the tyrosine residue to continue abstracting hydrogen atoms from the top half of the dimer pair, which obviates radical motion to reach the substrate molecule on the bottom half of the dimer. The result, in the S_2 state, is two hydroxide ligands cofacially oriented across the open "C" end of the manganese cluster. Further oxidation to the S_3 state results in an oxo/hydroxo substrate configuration, and the S_4 state transiently forms cofacial oxos, that spontaneously condense to give dioxygen, while the four electrons from the oxos (still formally at the oxidation level of water) reduce the manganese cluster back to the S_0 state. The role of calcium in this model is not clear, however, it could act as a substrate handler, ferrying new substrate molecules into the active site of the enzyme. It is known that if Sr^{2+} is substituted for Ca^{2+} , oxygen evolution is supported, albeit at reduced rates (~40%), while other divalent or univalent cations are ineffective at supporting O_2 evolution[29]. This observation demands further experimentation before divalent cation activation of PSII becomes well understood.

Th

pieces of

mangane

substrate

hyperfin

phenolic

perform

this, the

freedom

cofacto

amino

reducta

found

kcal/m

hydro

mang

mang

hydro

now

of th

This hydrogen abstraction model for oxygen evolution is supported by many key pieces of evidence. Electron spin echo modulation studies place Y_Z within 3.5-5 Å of the manganese ensemble, well within range for Y_Z to act directly upon manganese bound substrate molecules[27, 30]. It was determined by examining the line widths of the hyperfine couplings of the unpaired spin of the tyrosine Z radical to the β -protons of the phenolic side chain that Y_Z has significant rotational mobility, which implies that it performs a role more complex than that of a simple electron transfer cofactor. Contrary to this, the other redox active tyrosine residue in PSII, Y_D does not enjoy the rotational freedom of Y_Z , indicating it is more likely to play the role of a pure electron transfer cofactor[31]. There are several O_2 dependent metalloradical enzymes that utilize an amino acid radical as a hydrogen-atom abstraction agent. These include ribonucleotide reductase, galactose oxidase, and prostaglandin synthase[32, 33].

The bond dissociation energy (BDE) of the phenolic O-H group on Y_Z has been found to be approximately 86-87 kcal/mol. This value, when compared to the ~120 kcal/mol BDE for water would indicate the incompetence of tyrosine to perform hydrogen abstraction upon substrate water. However, the BDE of water ligated to manganese falls to ~82-94 kcal/mol, and to ~82-83 kcal/mol for hydroxide bound to manganese. These values indicate that, indeed, Y_Z could be competent in performing hydrogen atom abstraction on substrate water or hydroxide molecules[34-37].

While the Hoganson model incorporates much of the experimental information now known about PSII, it is not widely accepted as the “correct” answer to the question of the mechanism of photosynthetic water oxidation. In fact, several other mechanisms

have been

been prop

the mang

form dic

oxidation

a clear,

outright

contain

frequen

obtain

in phot

lack of

II. An

utilize

protein

exper

regar

chlor

rende

man

have been proposed that disagree with the mechanism described above. One model has been proposed that utilizes two oxyl radicals in a di- μ -oxyl bridging geometry in one of the manganese dimers[20] as the species present in S_4 . The oxyl radicals then condense to form dioxygen. Despite the differing theories for the precise mechanism of water oxidation, it is clear that the various models that have been proposed need to be tested in a clear, conclusive manner so that they may be fine tuned, overhauled, or rejected outright. One aspect of the new series of models is that the S-states are predicted to contain molecular structures that will present unique and characteristic signals in the low frequency region of their vibrational spectra.

It has been a goal of ours to develop experimental methodologies whereby we can obtain information about the low frequency vibrations exhibited by the manganese cluster in photosystem II, and thus contribute specific information regarding the presence of (or lack of) specific chemical species at certain points in the catalytic cycle of photosystem II. An example of the utility of this type of information comes from the experiments that utilized time resolved resonance Raman spectroscopy to investigate the respiratory protein cytochrome *c* oxidase, which catalyzes the reduction of O_2 to water[38, 39]. These experiments provided vibrational data that facilitated the formulation of proposals regarding dioxygen reduction in the cytochrome *c* oxidase. However, the presence of chlorophyll molecules in PSII obscures any signals arising from the manganese, and renders a resonance Raman approach ineffective.

Because Raman spectroscopy is not a viable option for the study of the manganese cluster in PSII, an obvious alternative is infrared spectroscopy. However, as

was discu

is not inf

reaction-r

challengi

high-qua

differenc

spectra.

specific

Hogans

water b

two lig

II sam

advanc

electro

occur[

one to

bound

differ

vibra

the S

ener

orig

was discussed in chapter 4, low-frequency information in the infrared spectra of proteins is not information that is easily obtained. But, as we have found, the judicious use of reaction-modulated infrared difference spectroscopy, can give us a foothold into this challenging area of spectroscopy. We have developed methods whereby we can obtain high-quality Light-Induced FTIR difference (LI-FTIR) spectra that reflect the vibrational differences between the S_1 and the S_2 state of the OEC. Within the vibrational difference spectra, we intend to find information that will provide direct evidence of the existence of specific molecular structures in the reaction center.

As an example of the type of information we plan to obtain, consider the model of Hoganson et al presented in Figure 5-7. In the S_1 state, it is postulated that there will be a water bound to one manganese, and a hydroxide bound to the second manganese. These two ligands to manganese will have characteristic vibrational frequencies. If photosystem II samples are illuminated at 200K the S_1 state will advance to the S_2 state. Further advancement to the higher S-states is not possible due to the fact that at 200K or lower, electron transfer from Q_A to Q_B is inhibited and thus only a single charge separation can occur[40]. In the S_2 state it is theorized that there are two hydroxide molecules bound, one to a Mn(IV) ion, and one to a Mn(III) ion. In S_1 , there was postulated a hydroxide ion bound to a Mn(III) ion, and a water bound to another Mn(III) ion. In an infrared difference spectrum of the S_2 state minus the S_1 state, negative modes will correspond to vibrations that disappeared upon formation of the S_2 state, *i.e.* those that corresponded to the S_1 state. Assuming that the Mn(III)-OH bond in S_1 , and the Mn(III)-OH bond in S_2 are energetically degenerate, then the difference spectrum will show a positive mode originating from the Mn(IV)-OH and a negative mode from the loss of the Mn(III)-H₂O;

the M

the id

$Mn=C$

vibrat

where

neces

in ord

(EPR

their

result

Mate

to the

consi

and

μm

ME

this

Gh

det

the Mn(III)-OH modes cancel each other out. With the use of isotopically labeled water, the identification of these modes should be straightforward, as a Mn-H₂O, Mn-OH, or Mn=O structure will each present a unique and identifiable isotope dependence in its vibrational frequency.

In order to gain access to the low frequency region of the infrared spectrum, where these intermediates in the water oxidation process will vibrate, it has been necessary to devise techniques to remove most of the bulk solvent water from the samples in order that the low frequency vibrational modes are not obscured. Control experiments, (EPR and oxygen evolution) have been performed to ensure that the samples retained their biological integrity, and are thus fully competent to perform water oxidation. The results of these experiments are described here.

Materials and Methods

Photosystem II enriched subchloroplast particles (BBYs) were prepared according to the methods of Berthold *et al* [41]. The samples were suspended in SMN buffer which consisted of 0.4M sucrose, 50mM 2-(N-Morpholino)ethanesulfonic acid (MES) (pH 6.0), and 10mM NaCl. The particles exhibited oxygen evolution rates of 600-700 $\mu\text{moles/O}_2/\text{mg chl/hour}$. For FTIR measurements, the samples were resuspended in 5mM MES, 5mM CaCl₂, 5mM NaCl. The samples exhibited no decline in oxygen evolution in this medium. Reaction center cores (RCCs) were prepared according to the methods of Ghanotakis *et al* [42, 43]. Briefly, BBY particles were solubilized with the non-ionic detergent octylthioglucoside. The solubilization served to strip away membrane

fragments.

The RCC

for FTIR

(FTIR bu

incubatio

M

the pres

EDTA

the pre

manga

remain

evolu

with

0.4M

kDa

SrC

buf

dia

gi

ba

fragments, and the light harvesting proteins, leaving an oxygen evolving core preparation. The RCCs exhibited O_2 evolution rates of 1400-1600 $\mu\text{moles } O_2/\text{mg chl/hour}$. Samples for FTIR were resuspended in 150mM sucrose, 5 mM MES, 5mM NaCl, 5mM CaCl_2 (FTIR buffer). Oxygen rates were not affected by resuspension in such a medium, nor by incubation in the dark, at 0°C , for ~24.

Manganese depleted samples were prepared by 1) incubating BBYs or RCCs in the presence of 0.8M Tris(hydroxy-methyl)aminomethane (pH 8.0) ("tris"), 1.00 mM EDTA for 30 minutes under room light at 0°C [44], or 2) by incubating BBYs or RCCs in the presence of 10mM NH_2OH , for 30 minutes, at 0°C , in the dark [45, 46]. After manganese depletion, samples were washed twice in FTIR buffer to remove any Mn^{2+} remaining after manganese depletion. Samples so treated exhibited no detectable oxygen evolution.

For the $g=4.1$ studies, samples were prepared by either substitution with Sr^{2+} or with ammonia. The Sr^{2+} samples were prepared by washing the reaction center cores in 0.4M sucrose, 50mM MES (pH 6.0), 2 M NaCl. This treatment removes the 17 and 23 kDa polypeptides. The samples were then resuspended in FTIR buffer containing 40mM SrCl_2 . Ammonia treated samples were prepared by resuspending the samples into FTIR buffer and adding 100mM NH_4Cl .

FTIR samples were prepared by depositing an aliquot of PSII's onto 25mm diameter AgCl IR windows (Wilmad). The amount of sample deposited was calculated to give a total quantity of chlorophyll of 30 μg , or $\sim 10^{-10}$ moles of reaction center cores, based upon 250 chlorophyll molecules per BBY particle, and 75 chlorophyll molecules

per reaction

of 1.3 cm

for 15-20

integrated

routinely

mode at

C

partially

FTIR sa

Oxford

control

beams

1.00)

(see

abso

sam

tem

for

con

ap

sp

per reaction center core particle. The samples were deposited to give a sample “spot size” of 1.3 cm in diameter. The samples were then dried under a stream of dry nitrogen gas, for 15-20 minutes, until no liquid water was visible under visual examination. The integrated intensity of the infrared water absorption band centered at $\sim 3500\text{ cm}^{-1}$ was routinely 8-10 times that of the integrated intensity of the Amide I protein absorption mode at 1650 cm^{-1} .

Control EPR experiments were performed on either fully aqueous samples, or on partially hydrated samples deposited on to mylar, and dried in the same manner as the FTIR samples. EPR spectra were run on a Bruker ER-300 Spectrometer equipped with an Oxford Systems Liquid Helium cryostat for cryogenic studies, or at 200K for FTIR control studies.

FTIR experiments were performed with a Nicolet 740 spectrometer with a KBr beamsplitter and a Graseby Infrared MCT detector (Graseby Infrared Model MCT-16-1.00). The sample was cooled to 200K by using a home-built nitrogen gas flow cryostat (see chapter 4 for a description of the sample temperature system). The absolute absorbance of the amide I band of the sample did not exceed 1.0 absorbance unit. The sample temperature was controlled to $\pm 0.1^\circ\text{C}$ with a LakeShore Cryogenics Model 321 temperature controller for the experiments using reaction center cores. The temperature for the experiments with BBYs was controlled with an Omega model 76000 temperature controller to $\pm 0.2^\circ\text{C}$. Double sided interferograms were collected at 4 cm^{-1} resolution, and apodized using a Happ-Ganzel apodization function. 500 scans were averaged for each spectrum. Sample illumination was carried out with a 150W halogen bulb. Infrared

component

copper sul

fiber optic

sampling

spectra w

directly i

the "dar

polynon

offset t

specific

Flat ba

the sar

peaks

electr

for B

Res

dev

ref

ch

components of the actinic light were removed by using two thick glass filters, 1 cm of 5% copper sulfate solution, and a low frequency filter that passes visible light $\lambda > 650\text{nm}$. A fiber optic probe positioned next to the sample window transmitted the light into the sampling chamber. 20mW of light was incident upon the sample. $S_2Q_A^-/S_1Q_A$ difference spectra were obtained by collecting a dark spectrum at 200K, illuminating the sample directly in the cryostat, then collecting a spectrum of the illuminated sample. The ratio of the “dark” to the “light” provided the $S_2Q_A^-/S_1Q_A$ difference spectrum. A smooth polynomial function was subtracted from each light-minus-dark pair to correct for an offset to the baseline. Multiple spectra (6-15 individual spectra, depending upon the specific spectrum) were then averaged together to produce the final difference spectra. Flat baselines were verified by ratioing two “dark” spectra together prior to illuminating the sample. These “dark/dark” spectra were collected and examined and no reproducible peaks were found in the region below 1000 cm^{-1} (for example, see Figure 5-16).

Oxygen evolution measurements were performed with a Clark-type Oxygen electrode. 100 μM or 1mM 2,6 dichlorobenzoquinone was used as an electron acceptor for BBYs, and RCCs respectively.

Results

Spectroscopic investigations of photosystem II rapidly progressed with the development of refined preparations of photosystem II. Until 1981, the most highly refined preparation consisted of plant chloroplasts where the membranes of the chloroplast had been mechanically or biochemically broken. In 1981, however, Berthold

and cow

of the c

100. T

bioche

Photos

memb

molec

chloro

prepa

would

EPR

signa

meth

retai

thes

stud

diag

nec

par

Y_D

(m

sa

ty

and coworkers[41] reported a preparation of photosystem II in which a large percentage of the chloroplast membrane had been digested away by using the detergent Triton X-100. The remaining membranes were highly enriched in photosystem II. This biochemical breakthrough gave spectroscopists access to samples in which the Photosystem II concentration was double what was previously attainable in thylakoid membrane preparations. Thylakoid membranes typically contain 400 chlorophyll molecules per reaction center, whereas BBY particles contain 220-250 chlorophylls/reaction center[41]. More importantly, however, is the fact that these BBY preparations contain minimal photosystem I contamination, which, under illumination, would contribute to any light induced difference spectra.

EPR Control Experiments-BBYs: Because we are ultimately interested in observing FTIR signals from the low frequency region of the infrared spectrum, it is necessary to devise methods whereby we can remove the bulk of the solvent water from the sample, yet still retain the biochemical activity of the samples. To establish the biological relevance of these samples, it is critical to verify their biochemical integrity. Photosystem II has been studied extensively by EPR[2]. Thus, we can use the well-characterized EPR signals as diagnostic benchmarks to establish that our samples can withstand the partial dehydration necessary for the infrared experiment. Figure 5-8a shows an EPR spectrum of BBY particles in solution. The signal observed shows the dark stable radical signal attributed to Y_D , a redox active tyrosine residue in photosystem II[47]. Figure 5-8b shows Tris-treated (manganese depleted) BBY particles, in solution, at room temperature. In Tris treated samples it can be seen that under illumination, there is a light induced increase of the tyrosine signal because there is no longer a reductant immediately available to reduce the

radical

from

There

samp

oxyg

the n

succ

Figur

parti

illun

S₂ s

belo

man

gene

sign

the

resu

deb

exp

inc

w

radical generated at Y_Z . Thus the radical signal from Y_Z is added to the tyrosine signal from the Y_D . Y_D exhibits a highly stable EPR signal in O_2 evolving samples of BBYs. Therefore it can be used as an intensity standard against which other signals from the samples can be referenced. As discussed above, it is well known that the S_2 state of the oxygen evolving cluster of photosystem II exhibits an EPR multiline signal. Therefore, the multiline signal is an excellent control signal to verify that the S_2 state can be successfully generated in the partially dehydrated samples needed for FTIR spectroscopy. Figure 5-4 shows the multiline EPR signal generated in an aqueous sample of BBY particles by illumination of the sample at 200K. It has been shown that continuous illumination of PSII samples at 200K advances the S-state of the manganese cluster to the S_2 state, but no further due to the fact that electron transfer from Q_A to Q_B is inhibited below this temperature[40]. Because Q_A can only accommodate one electron, the manganese cluster is limited to a single turnover. Figure 5-9 shows the S_2 multiline signal generated in BBYs, by 200K illumination, in partially dehydrated samples. The multiline signal generated in the partially dehydrated samples is equal in amplitude (normalized to the amplitude of Y_D) and appearance as that generated in fully hydrated samples. The results of this EPR experiment show that we can successfully generate the S_2 state in dehydrated samples of BBY particles.

Because we will generate the S_2 state by illumination at 200 K, in the FTIR experiment, it is important that we also characterize the formation of any other light induced species formed in the dried samples under these conditions. This will ensure that we are fully aware of the species present when making assignments in the FTIR

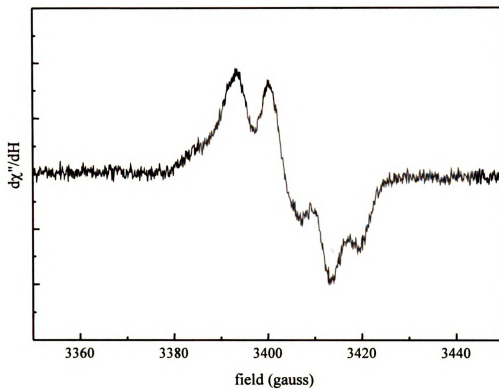


Figure 5-8a: Dark stable EPR signal from Y_D in BBY particles. Microwave power 1mW, 2.5 gauss modulation amplitude, 2 minute scan, room temperature.

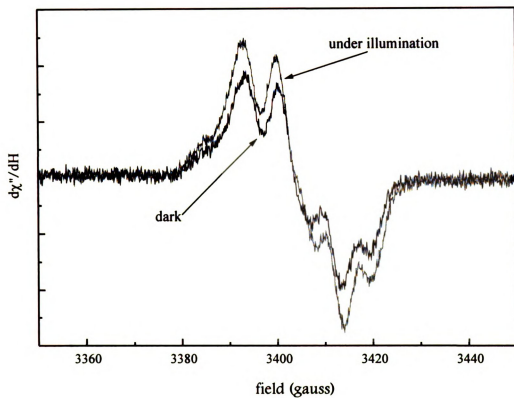


Figure 5-8b: Tris-washed BBY particles, before, and under illumination. Same spectral conditions as Figure 5-8a.

Figure
parti
gain

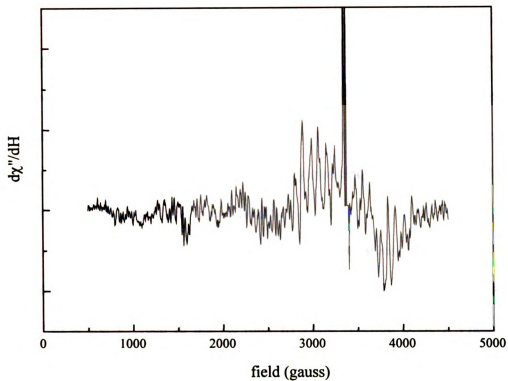


Figure 5-9: S_2 -multiline signal from partially dehydrated film of O_2 evolving BBY particles illuminated at 200K. 2mW microwave power, 20 gauss modulation amplitude, gain= 1×10^5 .

differe

10a) in

a smal

amour

signal.

light i

washe

induce

approx

FTIR

partial

presen

shows

and 10

at 200

two m

record

against

sample

spectr

state a

difference spectra. When the dark stable tyrosine signal is examined at 200K (Figure 5-10a) in partially dehydrated, O₂ evolving BBYs, it is clear that under illumination there is a small change in the signal. This change can be attributed to the generation of a small amount of chlorophyll radical, based upon the linewidth and g value of the light induced signal. Integration of the signal before and under illumination allows quantification of the light induced radical, and shows that it is present in 10-15% of the reaction centers. Tris washed, manganese depleted, BBY samples illuminated at 200K show a very large light induced increase of the signal, indicative of the generation of chlorophyll radicals in approximately 70% of the centers (Figure 5-10b).

FTIR Spectra of BBY Particles: We have developed conditions under which we can partially dehydrate BBY samples and still retain biological integrity as evidenced by the presence of EPR signals seen in native, fully hydrated reaction centers. Figure 5-11a shows a LI-FTIR difference spectrum of oxygen evolving BBY particles between 1800 and 1000 cm⁻¹. The spectrum was collected by recording the dark spectrum of the samples at 200 K, illuminating the sample for 10 seconds, allowing the sample to dark adapt for two minutes to allow any unstable, transiently formed, chlorophyll radical to decay, then recording a light spectrum. The ratio of the dark and light spectra was taken directly against each other to obtain the final difference spectrum. Difference spectra from 18 samples were then averaged together to generate the final difference spectrum. This spectrum, the S₂Q_A-/S₁Q_A difference spectrum show vibrations attributable to the S₂Q_A-state as positive modes, and vibrations attributable to the S₁Q_A state as negative modes. In

Figur
wash
modu

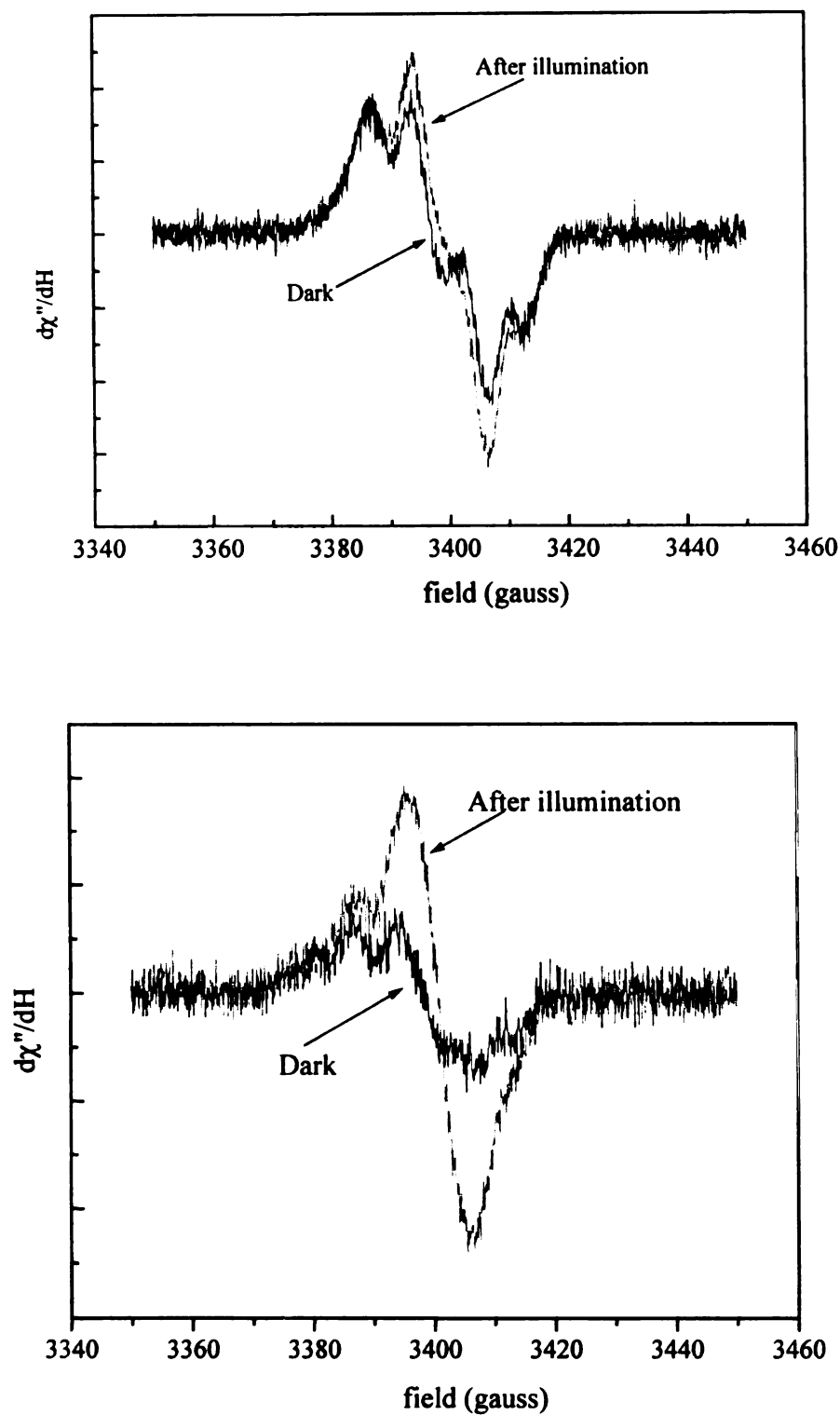


Figure 5-10a) (top) EPR spectrum, 200K, partially hydrated BBY particles, b) tris-washed BBY particles before and after illumination. Microwave power = 0.2mW, 4 gauss modulation amplitude, gain = 1×10^5

red is shown the average of the “dark/dark” spectra taken before illumination, which gives an indication of the noise levels and any systematic fluctuations in the experiment.

In Figure 5-11b is shown the lower frequency range (1000cm^{-1} - 600 cm^{-1}) of the same sample as Figure 5-11a. The technical advances described in the previous chapter have allowed us to acquire and present data from the low frequency region for the first time. A readily apparent feature of this spectrum is the presence of numerous difference bands. This fact is encouraging in that it generates confidence that we are capable of detecting absorptions in the low frequency region of the infrared spectrum and that the low frequency region of the spectrum may contain data relevant to the mechanism of photosynthetic water oxidation.

In Figure 5-12a is shown the LI-FTIR difference spectrum of Tris-treated BBY particles. In Tris-treated BBY particles, the manganese cluster has been removed, and thus any vibrations in the difference spectrum of O_2 evolving samples that are attributable to the manganese cluster, should not be present in the difference spectrum of Tris-treated samples. Figure 5-12b shows the spectrum of the same sample in the 1000cm^{-1} to 600 cm^{-1} range. In Figures 5-11b and 5-12b it can be seen that the signal to noise ratio for the peaks in the 680 cm^{-1} region is approximately two. In order to make clear, definitive observation of the peaks, the signal to noise ratio must be increased. Because of this, it would be advantageous to utilize a more highly resolved preparation of photosystem II, such as reaction center cores. This would increase the effective concentration of

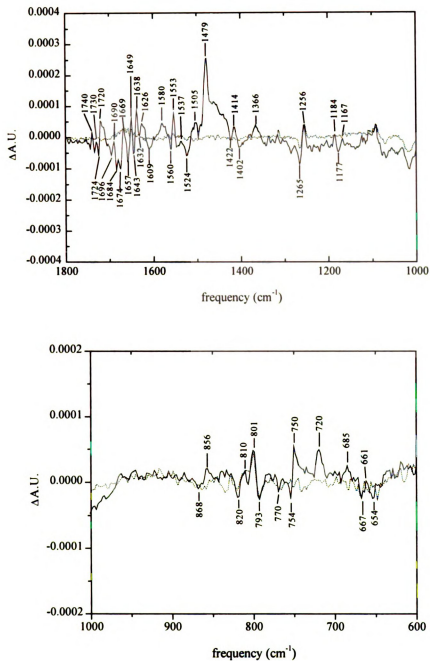


Figure 5-11 a) (top) and b) (bottom) Black: S_2Q_A -/ S_1Q_A - light induced FTIR difference spectra of BBY particles, 200K, 9000 scans. Dash: “dark-dark” for noise reference.

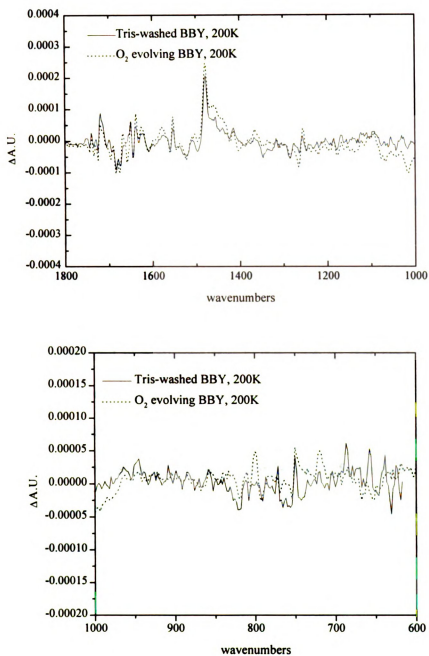


Figure 5-12a) (top) and b) (bottom) Light-induced FTIR difference spectrum of tris-washed BBY particles, 200K. 6000 scans.

oscillators in our samples, thus increasing the signal to noise ratio. However, the more highly resolved preparations are more delicate, and thus require special conditions where they can handle the partial dehydration process required for the FTIR work.

EPR Control Experiments-RCCs: Because of the increased reaction center concentration in samples of reaction center cores as compared to subchloroplast preparations, it was desirable to develop conditions where the more fragile reaction centers could withstand the partial dehydration process and still exhibit the EPR signals attributed to fully native reaction centers. Resuspension of the samples in a lightly buffered medium that contains reduced amounts of sucrose, allows us to detect the various EPR signals with the dried samples, that have been previously attributed to intact reaction center core preparations. If the samples were suspended in a sucrose free buffer, such as that used for the BBY experiments, then the dried samples exhibited the multiline EPR signal, but were not competent in generating an alternate signal from the S_2 state, the $g=4.1$ signal. This $g=4.1$ signal is attributed to a magnetically different conformer of the S_2 state of the manganese cluster. Additionally, it was found that with RCCs, the small amount of sucrose greatly enhanced the signal amplitude in the LI-FTIR difference spectra. In the case of BBY particles, the LI-FTIR signal amplitudes were not dependent upon the sucrose content of the medium.

Figure 5-13 shows the multiline EPR spectrum generated in the partially hydrated films of reaction center cores deposited on mylar strips. As in the case of the BBY samples, the amplitude of the multiline signal generated in the partially hydrated films of RCCs is equal in amplitude on a per chlorophyll basis as the multiline signal generated in the fully aqueous reaction center core samples. Figures 5-14a-c show the dark stable

radical Y_D spectra of the dried O_2 -evolving, tris-washed and Sr^{2+} substituted RCC films, respectively, at 200K. Under illumination there is a significant increase in amplitude in each spectrum, indicating that at 200K, a chlorophyll radical is generated in the samples. Integration of the signals before and after illumination shows that chlorophyll radicals are present in 50%, 85% and 75% for O_2 -evolving, tris-washed, and Sr^{2+} substituted samples respectively. In Figure 5-15 is shown the EPR spectrum of the $g=4.1$ signal generated in reaction center core samples by substituting Sr^{2+} for Ca^{2+} , or by introducing NH_3 to the samples.

FTIR Spectra of Reaction Center Cores: Figures 5-16a and 5-16b show the light induced FTIR difference spectrum at 200K of partially hydrated O_2 -evolving samples of reaction center cores, from 1800 cm^{-1} to 1000 cm^{-1} . This spectrum is the average of 13 different samples. For reference, the average of the dark/dark spectra are also included to allow visualization of the random noise levels present in the spectra. Immediately apparent is the increased signal-to-noise ratio of the spectrum acquired from RCCs versus the same spectrum generated with BBY particles. Part of this can be attributed to the increase in reaction center concentration in the RCCs over the BBYs. RCCs typically contain approximately 80 chlorophyll molecules per reaction center[42] while BBYs typically contain 3 times that number. Hence, the increase in reaction center concentration should substantially improve the signal to noise ratio of the light induced difference spectrum. As in Figures 5-11a and 5-11b positive modes correspond to the vibrations induced upon formation of the $S_2Q_A^-$ state and negative modes correspond to modes from the S_1Q_A state. In Figure 5-17a and 5-17b, is presented the difference spectrum from Tris-treated

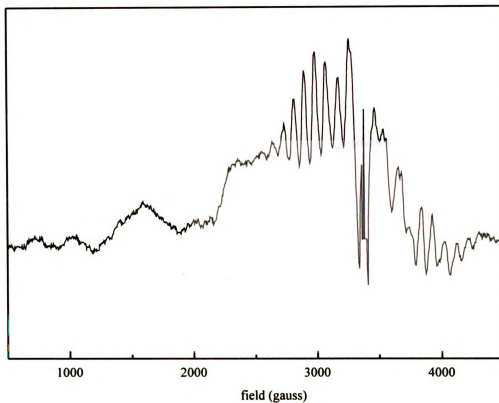


Figure 5-13: Multiline EPR spectrum of partially-hydrated reaction center cores. 200 μ g chlorophyll dried on mylar. Microwave power: 2 mW, 20 gauss modulation amplitude, gain = 1×10^5 . Temperature = 8K.

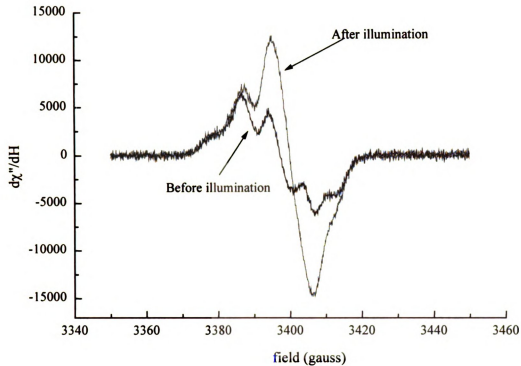


Figure 5-14a: EPR spectrum of O_2 evolving RCCs, before and after illumination. Integration indicates the formation of chlorophyll radical in approximately ~50% of the centers. Same spectral conditions as Figure 5-10.

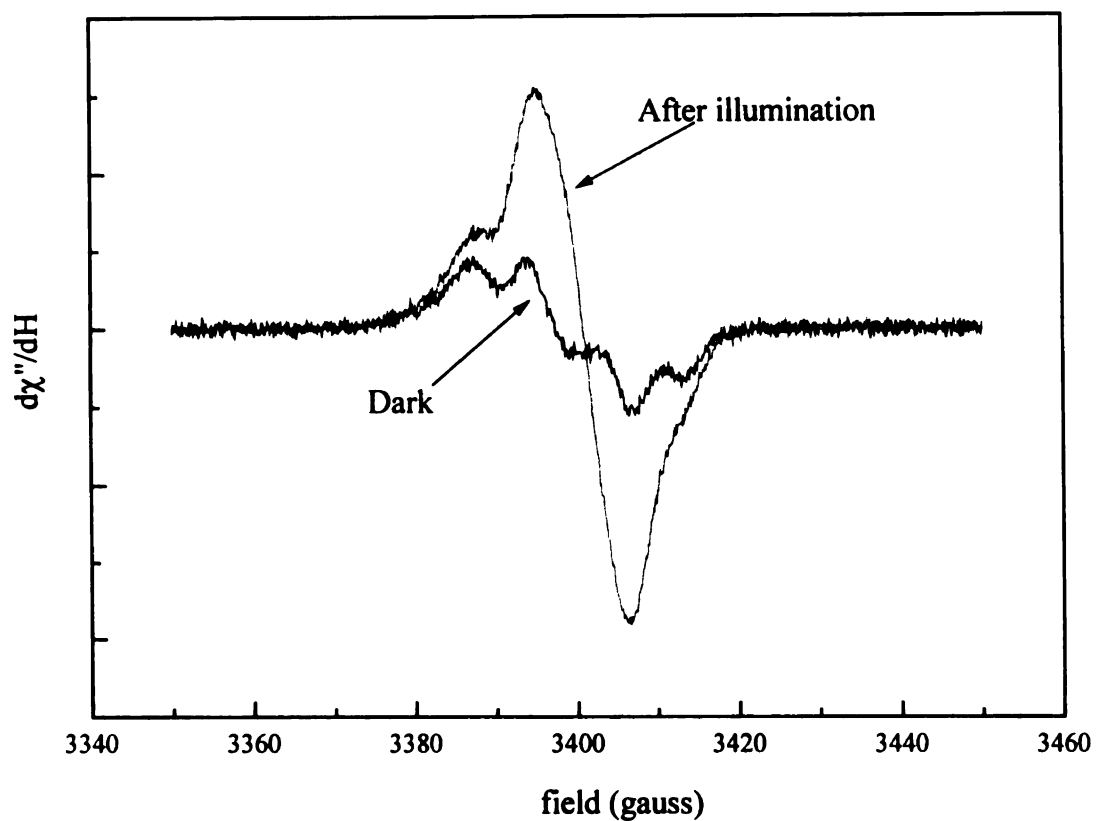


Figure 5-14b: EPR spectrum of Tris-washed RCCs at 200K, before and after illumination. Integration of signals shows generation of chlorophyll radical in approximately 85% of centers. Same spectral conditions as Figure 5-10.

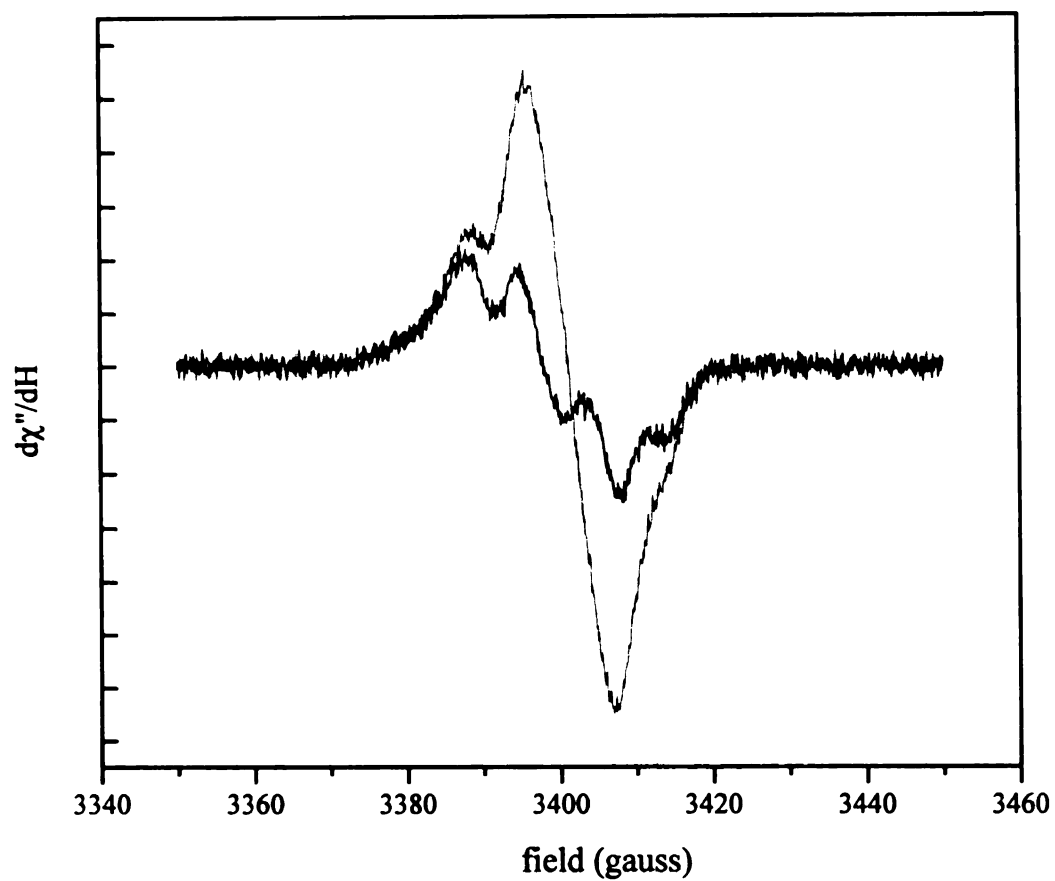


Figure 5-14c: EPR spectrum of Sr^{2+} substituted RCCs at 200K before and after illumination. Integration of signals showed chlorophyll radicals generated in approximately 75% of the centers. Same spectral conditions as Figure 5-10.

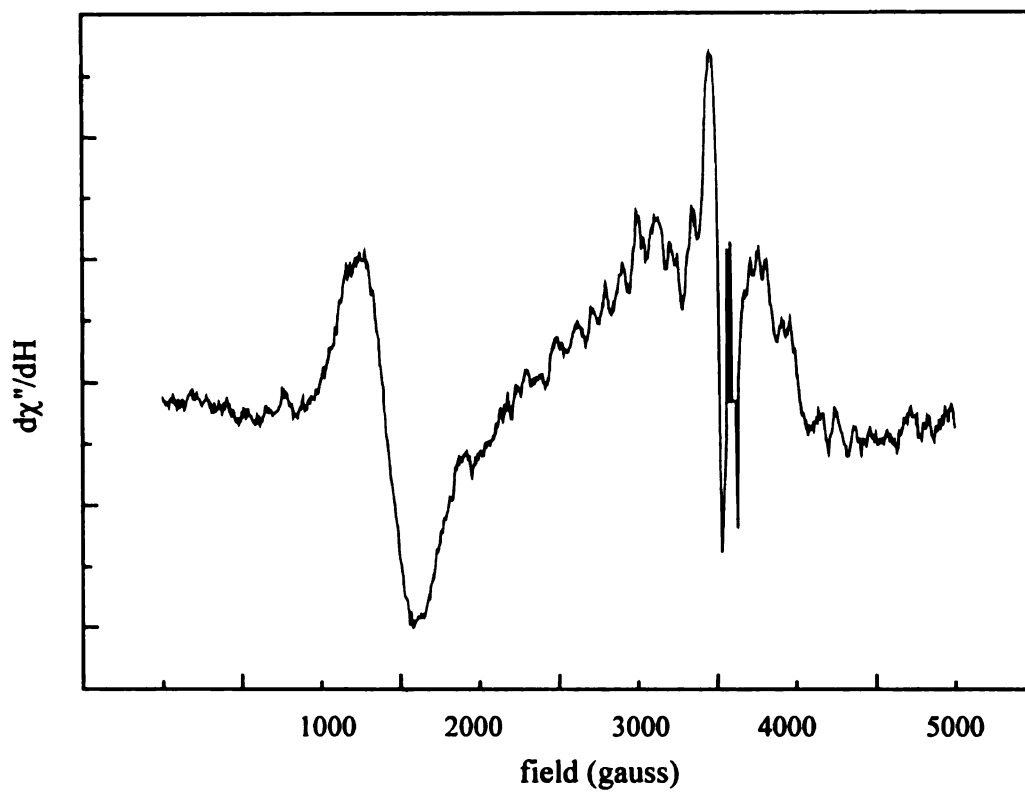


Figure 5-15a: EPR spectrum of Sr^{2+} substituted $g=4.1$ signal in partially hydrated RCC sample. Spectral conditions same as Figure 5-13.

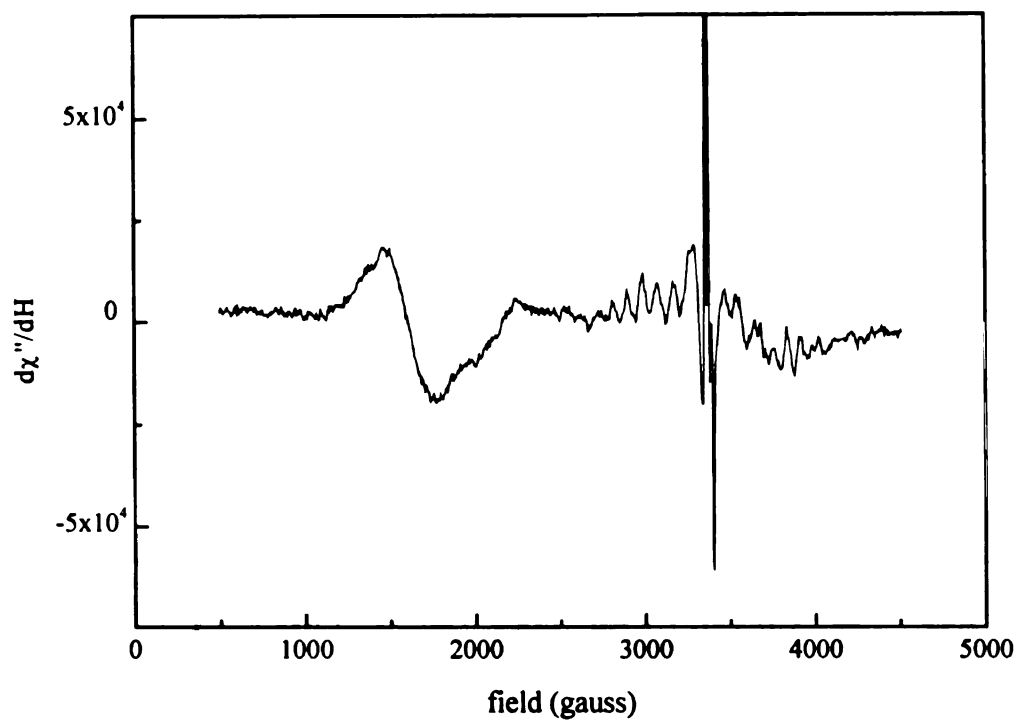


Figure 5-15b: EPR spectrum of NH_3 substituted $g=4.1$ signal in partially hydrated RCC sample. Spectral conditions same as Figure 5-13.

RCC particles. Because the tris-treated samples are manganese depleted, we expect that any absorbances in the spectrum of O_2 evolving samples that are due to vibrations of the manganese cluster should not be present in the spectrum of the manganese depleted samples. As a control experiment, RCCs were manganese depleted using an alternative method. Low concentrations (~ 1 -10mM) of hydroxylamine (NH_2OH) is known to effectively reduce the manganese cluster to Mn^{2+} . EPR measurements of dried NH_2OH -treated RCCs exhibited similar quantities of light-induced chlorophyll radical as the tris-treated samples. LI-FTIR spectra were acquired (Figure 5-18) to check for agreement with the spectra acquired with Tris treated data.

Figure 5-19a and 5-19b shows the light induced FTIR spectrum of RCCs that were resuspended in FTIR buffer using 97% ^{18}O labeled H_2O . The samples were allowed to incubate on ice, in the dark, for 12-14 hours before they were deposited onto AgCl infrared windows and dried. Oxygen evolution of these samples was unaffected by the prolonged soak period. Not shown is the EPR control spectra of partially dehydrated samples treated in this way. The signals were identical to fully active RCC samples. Figure 5-20a and 5-20b shows the light induced FTIR difference spectrum of RCCs that were resuspended in 97% ^{18}O labeled FTIR buffer with 100 μ M 2,6-dichlorobenzoquinone, a quinone molecule that can accept electron from the primary quinone acceptor, Q_A , of PSII. The samples, before being dried on to the IR windows, were incubated on ice, under room lights for 30 minutes to allow the manganese cluster to cycle through the S-states several times. Control samples, in ^{16}O buffer, were tested to

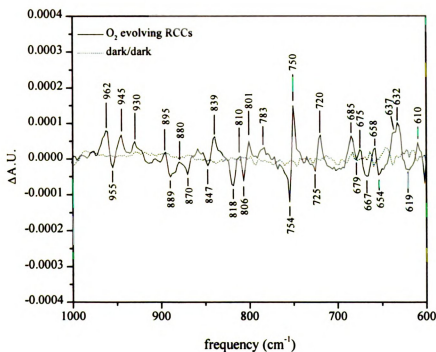
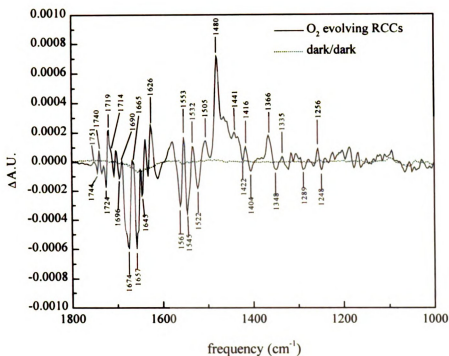


Figure 5-16 a) top and b) bottom. LI-FTIR difference spectrum of the $S_2Q_A^-/S_1Q_A$ state. reaction center cores, 200K illumination. 6500 scans total. Dashed spectrum is dark/dark for noise reference.

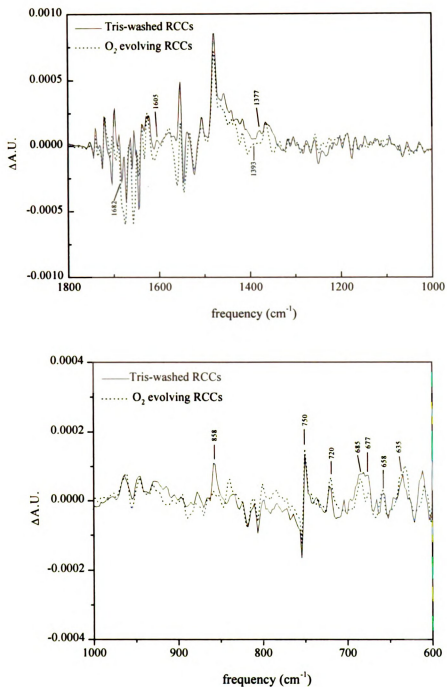


Figure 5-17a) top and b) bottom. (black) LI-FTIR spectrum of tris treated reaction center cores, 200K. (dash) O_2 evolving RCCs (Figure 5-16). Tris-spectrum average of 12 samples, 6000 scans. 200 K.

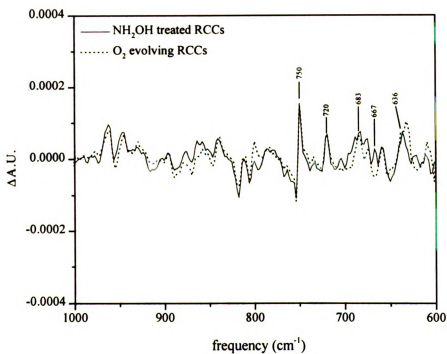
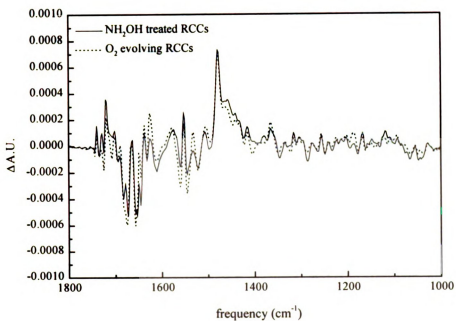


Figure 5-18a) top, and b) bottom. (black) LI-FTIR spectrum of NH_2OH treated RCCs (manganese depleted), 200K, 6000 scans. (dash) O_2 evolving samples (Figure 5-16).

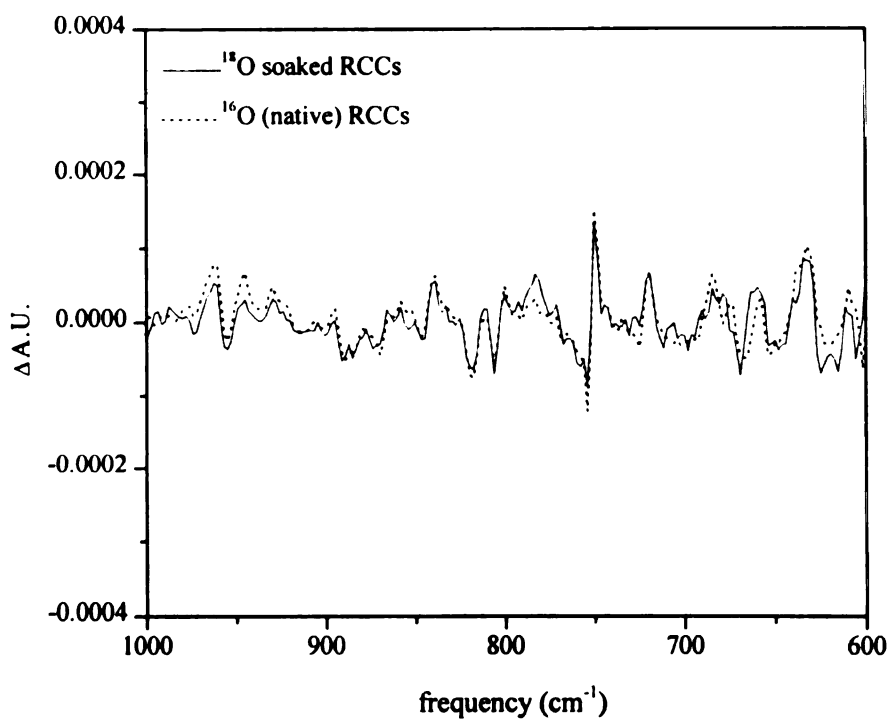
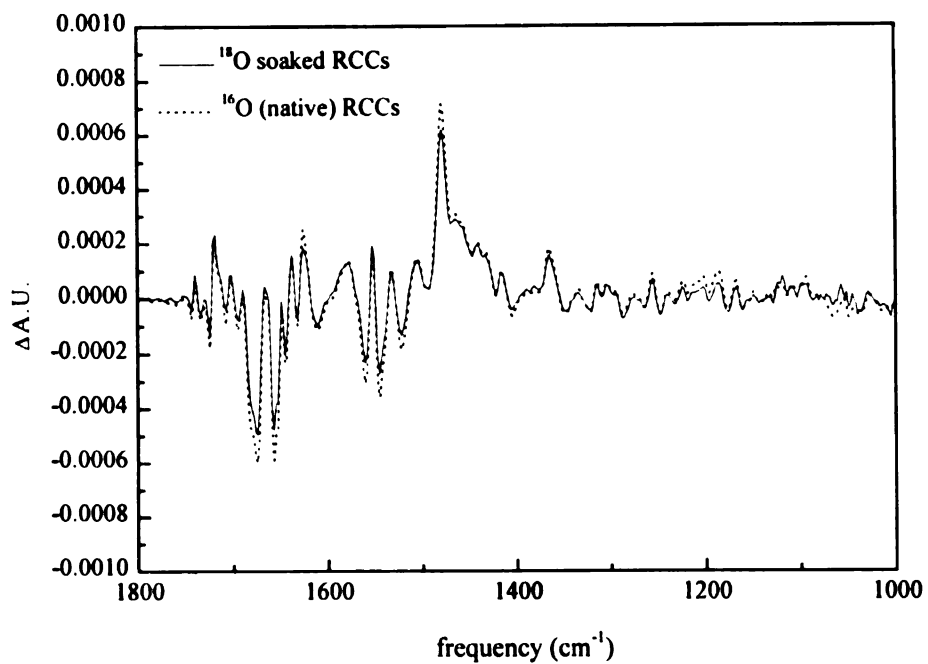


Figure 5-19a) top, and b) bottom. (black) LI-FTIR spectrum of RCCs soaked in ^{18}O -labeled buffer. 6000 scans, 200K. (dash) O_2 evolving RCCs (Figure 5-16).

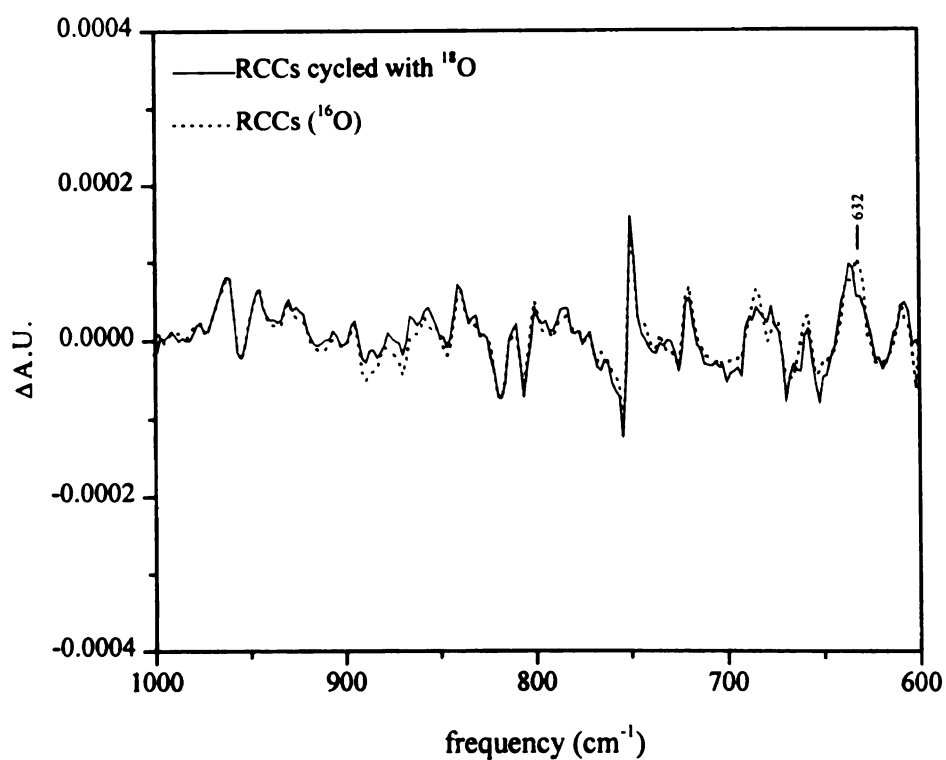
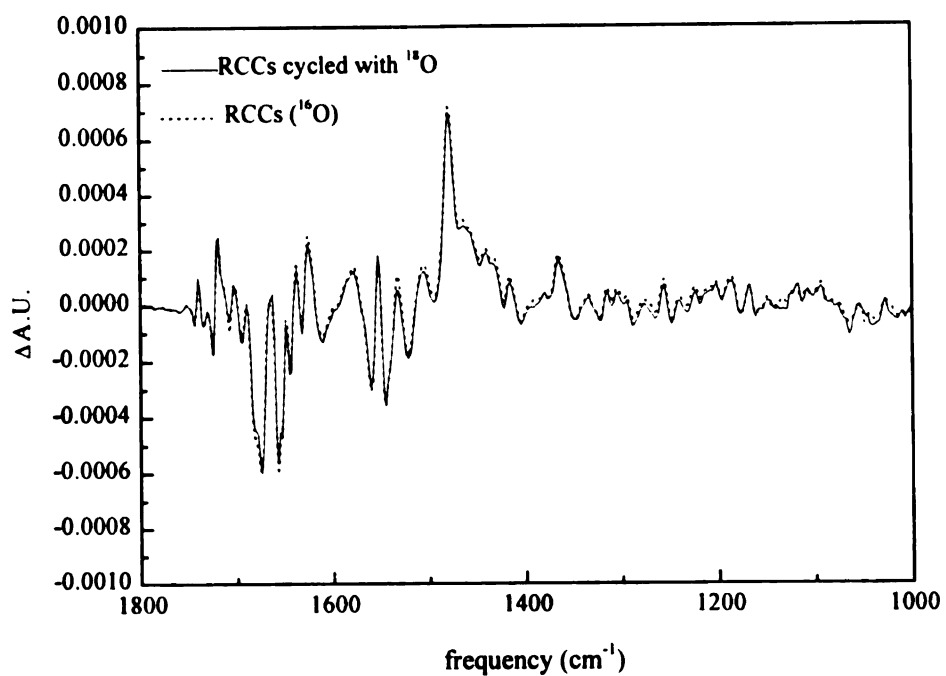


Figure 5-20a) top, and b) bottom. (black) LI-FTIR spectrum of RCCs turned over in presence of ^{18}O -labeled buffer. 6000 scans, 200K. (dash) O_2 evolving RCCs (Figure 5-16)

ensure that samples treated this way, showed oxygen evolution rates and EPR spectra that were consistent with native, untreated samples.

Figures 5-21 and 5-22 show the FTIR spectra acquired by 200K illumination of samples that were treated with either a) ammonia (Figure 5-21) or b) Sr^{2+} (Figure 5-22). EPR studies have shown that these conditions will generate the $g=4.1$ signal in lieu of the multiline signal. When samples exhibit the $g=4.1$ signal, it has been proposed that the manganese cluster is in a significantly different geometric arrangement compared to the cluster under conditions that the S_2 multiline signal is displayed. These spectra may shed light on the origin of this difference.

Discussion

We have developed methods whereby we can acquire data on the vibrations exhibited in the low frequency region for photosystem II preparations. The vibrations associated with the specific molecular structures thought to be present during the catalytic cycle of the oxygen evolving complex will be contained in this region of the infrared spectrum. Data in this frequency range have not been previously reported in the literature. The specific advancements that we have made that allowed the acquisition of these data include sample cooling techniques that allow the use of window materials that do not obscure the low frequency region of the spectrum and biochemical techniques that allow us to utilize the more highly resolved reaction center core preparation of PSII rather than the cruder subchloroplast preparations utilized by other research groups.

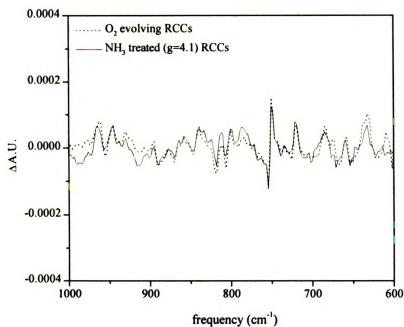
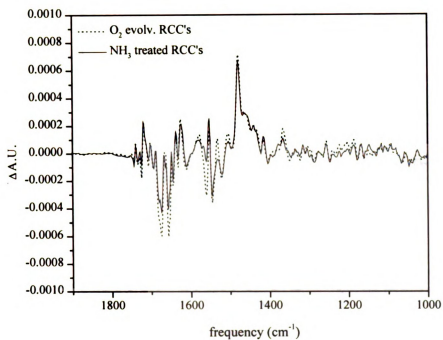
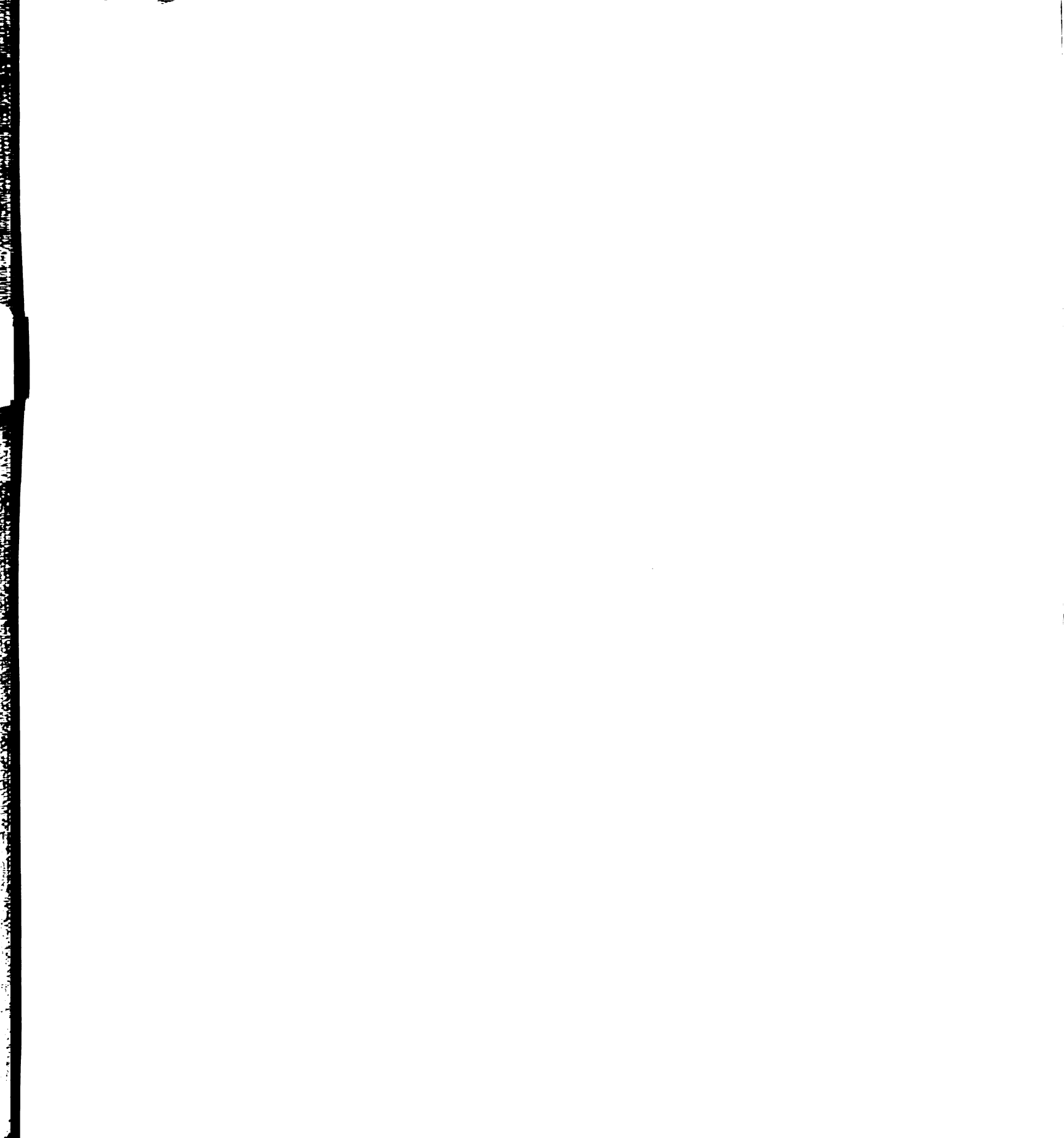


Figure 5-21a) top and b) bottom. (black) LI-FTIR difference spectrum of NH_3 treated RCCs. ($g=4.1$ conditions) 3000 scans. (dash) O_2 evolving RCCs (Figure 5-16).



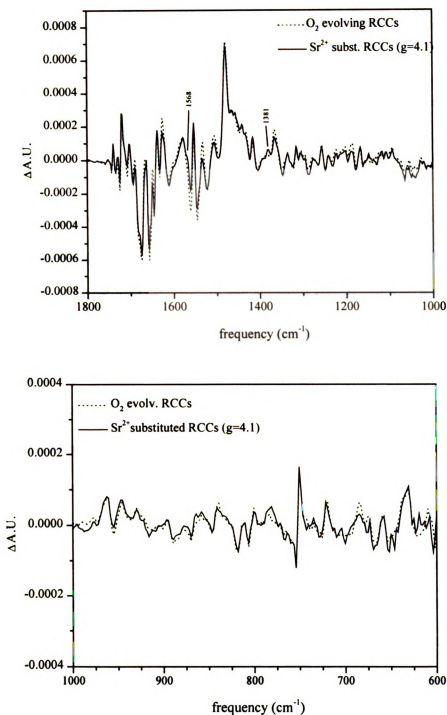


Figure 5-22 a) top and b) bottom. LI-FTIR difference spectra of Sr^{2+} substituted RCCs (g=4.1) conditions. 4000 scans. (dash) O_2 evolving RCCs (Figure 5-16).

The first step in developing these methods, however, was establishing experimental conditions whereby we could reproduce the infrared difference spectra reported by other groups, for the S_2Q_A -/ S_1Q_A transition of the enzyme. The data acquired, shown in Figure 5-11, show the infrared difference spectra of partially dehydrated BBY particles illuminated at 200K. When compared to previously reported spectra[48-50], it can be seen that we have essentially identical spectra (Table 5-1). It is very difficult to assign modes in this region of the spectrum due to the presence of numerous difference bands and the overlapping predictions made by group frequency arguments. Table 5-2 shows a compilation of vibrational information and expected vibrational frequencies for a number of protein backbone modes of vibration and amino acid side chain vibrations. Despite the complexity of this region of the spectrum it is possible, however, to make some very general assignments. The amide I mode of vibration from the protein backbone(primarily composed of the C=O stretch of the backbone carbonyl moieties) is centered around 1635cm^{-1} - 1670cm^{-1} . These modes of vibration are sensitive to the specific secondary structure of the protein, and thus large scale changes in the secondary structure of the protein would be manifested as changes in the amide I modes of vibration. While there are definitely difference peaks in the spectrum in the range of the amide I vibrations, the fact that the peaks observed are no larger than the others in the difference spectrum indicates that the protein does not undergo large scale conformational rearrangement upon advancement of the S-state. If any differential peaks in that region of the spectrum do arise from changes in the Amide I modes of vibration, the

Table 5-1 Vibrational Data (1800-1000 cm^{-1}) From Various LI-FTIR Measurements of Photosystem II

S_2Q_A-/S_1Q_A This work (RCCs)	S_2Q_A-/S_1Q_A This work (BBY)	S_2Q_A-/S_1Q_A [49] (BBY)	S_2/S_1 [51] (RCC)	Q_A- [49]	Q_A- [52]	Chl ⁺ [53]
+1751		+1748		+1749		+1747
-1744	-1743	-1742	-1744	-1743	-1744	
+1740	+1740	+1739	+1739	+1740	+1738	
-1734	-1734	-1736	-1735	-1735		-1736
+1730	+1730	+1731	+1729	+1731		
-1724	-1724	-1725	-1725	-1725	-1724	
+1719	+1720	+1719	+1719	+1720	+1719	
+1714		+1714				+1714
-1707		-1710		-1710		
+1703	+1703	+1704		+1706	+1707	
-1696	-1696	-1695		-1694	-1695	
+1690	+1690	+1688	+1689	+1688	+1687	
-1684	-1684	-1683		-1683	-1682	-1684
-1674	-1674	-1675	-1679	-1673	-1672	
+1665	+1669	+1666	+1667	+1663	+1660	+1665
-1657	-1657	-1659	-1657	-1658	-1657	-1660
+1649	+1649	+1650	+1650	+1649	+1650	
-1645	-1643	-1643	-1645	-1644	-1644	
+1638	+1638	+1637	+1637	+1637	+1637	
-1632	-1632	-1632	-1630	-1632	-1630	
						+1620
						-1614
+1626	+1626	+1625	+1622	+1624	+1625	
						+1570
-1561	-1560	-1560		-1560	-1560	
						-1551
+1553	+1553	+1551		+1551	+1550	
-1545	-1545	-1544		-1544	-1542	
						-1533
+1532	+1537	+1532		+1532	+1530	
-1522	-1524	-1522		-1521	-1519	
+1505	+1505	+1505		+1506	+1506	
						-1493
+1480	+1479	+1478		+1478	+1478	
+1456		+1456		+1458	+1456	
+1441	+1439	+1437				
-1422	-1422	-1421				
+1416	+1414	+1417		+1417	+1417	
-1404	-1402	-1402				
+1366	+1366	+1364		+1365	+1365	

Table 5-2 Group Frequencies of Protein-based Vibrations

Frequency (cm-1)	Mode	Origin
1750-1725	carboxyl C=O stretch	Aspartate/glutamate side chain
~1680	side chain C=O	Asparagine
1670-1630	C=O	quinone
1670-1635	Amide I (C=O, backbone)	Protein secondary structures
1670-1680	CN ₃ H ₃ ⁺	Arginine side chain
1670-1640	H-O-H bend	water
~1670	side chain C=O	Glutamine
~1660	NH ₂ ⁺ deformation	Histidine
1640-1610	NH ₃ ⁺ . asymm. deform.	Lysine
1640-1630	CN ₃ H ₃ ⁺ symm. stretch	Arginine
~1620	NH ₂ deformation	Asparagine
1620-1570	carboxylate C-O, asymm. stretch	Aspartate/glutamate
~1610	C=C stretch	quinone
~1550	N-H bend, Amide II	Protein secondary structures
~1480-1460	C-O stretch	semiquinone
~1480-1460	C-C stretch	semiquinone
~1450-1350	carboxylate C-O symm. stretch	Aspartate/glutamate

amplitudes indicate that conformational changes in the protein must be subtle or localized to the immediate vicinity of the manganese cluster.

Upon generation of the S_2 state, an electron travels from the manganese cluster, through the electron transport chain, and, at 200K, is inhibited from proceeding further than the plastoquinone molecule, Q_A , thus generating the anion radical $Q_A^{\cdot-}$. Therefore, in FTIR samples studied before and after illumination at 200K, the $Q_A^{\cdot-}$ species should contribute to the infrared difference spectrum. This $Q_A^{\cdot-}$ spectrum has been observed, and some of the modes were assigned previously by FTIR difference spectroscopy of photosystem II samples[54]. The difference peaks at $1724\text{ cm}^{-1}/1719\text{ cm}^{-1}$ have been assigned to the reduction of the primary quinone acceptor, Q_A . The peak at 1478 cm^{-1} has been assigned to the C-O stretch of the anion radical form of Q_A . Additional peaks in the 1650 cm^{-1} to 1750 cm^{-1} range may arise from side chain carbonyls, or carbonyls on chlorophyll molecules that undergo changes as the S-state advances. Between 1500 cm^{-1} and 1650 cm^{-1} , the antisymmetric stretches of carboxylates will be observed, as will the N-H stretches of amino groups, such as are found in glutamine or lysine residues. The Amide II protein backbone mode (composed of N-H bending modes) usually appears near 1550 cm^{-1} . Therefore it is reasonable to deduce that, analogous to the case of the Amide I modes, large scale conformational changes do not occur in the protein as the manganese cluster is oxidized. The pair of peaks at $1364\text{ cm}^{-1}/1403\text{ cm}^{-1}$ have been attributed to the symmetric stretching vibration of a carboxylate-containing residue that is involved with the coordination of the Ca^{2+} associated with the manganese cluster. The antisymmetric stretch of the same residue is located at $1560\text{ cm}^{-1}/1587\text{ cm}^{-1}$. This

assignment is based upon studies of Ca^{2+} -depleted samples, and the fact that upon ^{15}N labeling of the samples, these peaks were unaffected. The frequency difference between the symmetric and antisymmetric modes in the S_1 and S_2 states was used to propose that the carboxylate in the S_1 state is bound in a bridging bidentate conformation, and in the S_2 state, adopts a unidentate conformation. This is based upon the empirical observation that, in model systems, the difference in frequency between the symmetric and antisymmetric modes of a carboxylate ligand is a reflection of the specific mode of binding of the ligand to a metal ion[50].

It has been shown previously that it is possible to detect the presence of as little as 5% chlorophyll radical in photosynthetic systems with FTIR [55]. Therefore, in the FTIR spectra of BBY or RCC samples, we expect some contribution from chlorophyll radical to the light-induced FTIR spectrum. Some modes from chlorophyll radicals in PSII have been assigned previously[53]. Several vibrations in the S_2Q_A -/ S_1Q_A spectrum of BBY particles presented in Figure 5-11 are attributable to chlorophyll radical species present in the sample. The negative mode at 1684 cm^{-1} , and a positive shoulder at 1714 cm^{-1} are both vibrations that have been assigned in chl^+/chl difference spectra[53]. However, only the most intense difference peaks from the chl^+/chl difference spectra are apparent in our S_2Q_A -/ S_1Q_A spectrum of BBY particles.

The low frequency region of the S_2Q_A -/ S_1Q_A spectrum also exhibits a number of modes of vibration. However in order to identify conclusively absorptions that arise from the manganese cluster, it is necessary to acquire spectra that have better signal to noise ratios. By using reaction center core preparations the effective concentration of reaction centers is increased by a factor of three to four, which will improve the quality of the

spectra substantially. One issue regarding the use of reaction center cores is the relative fragility of these preparations relative to the more robust BBY type particles. It was necessary to develop conditions whereby these samples can be partially dehydrated, yet still exhibit all of the signals associated with native, fully aqueous systems.

In Figure 5-13, the multiline EPR spectrum obtained from samples partially dehydrated in FTIR buffer, which consists of 5mM MES (pH 6.0), 5mM NaCl, 5mM CaCl₂, and 150mM sucrose, is shown. It was found that normal multiline spectra could be acquired under conditions when samples were dried without any sucrose present, but the amount of chlorophyll radical generated by illumination was increased. Additionally, it has been shown that, under a variety of conditions, native, O₂ evolving PSII samples, generate a different signal associated with the S₂ state of the manganese cluster centered at g=4.1[2]. Without sucrose present, it, however, was not possible to generate the g=4.1 signal in the dried PSII films. Apparently, the appearance of the g=4.1 signal depends upon the presence of sucrose in the sample. A possible reason for this is the samples that include small amounts of sucrose in the drying medium retain approximately double the water after drying, than the samples that are dried in sucrose-free medium. It is possible that this increased level of hydration is what allows the formation of the g=4.1 signal.

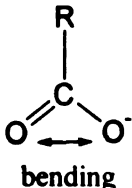
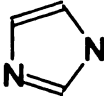

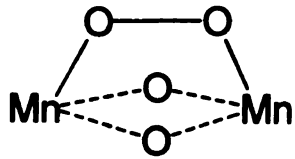
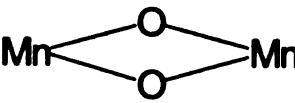
In Figure 5-16, the FTIR spectrum of partially hydrated samples of reaction center cores is presented. 13 individual sample spectra were averaged to produce this final spectrum. The signal to noise ratio of this spectrum is approximately 80, for the peak at 1478 cm⁻¹. The signal-to-noise ratio of the same peak in the spectrum from BBY particles, is approximately 12. This is despite the fact that the spectrum of RCC's was

acquired on the same total quantity of chlorophyll (30 μ g), and was the result of fewer total scans (6500 versus 9000 scans). The number of difference peaks appearing in the low frequency region is striking. Unfortunately, few studies have been performed with the goal of assigning the low frequency modes of proteins and amino acids. Table 5-3 lists the molecular structures, along with their projected frequencies, that may appear in the S_2Q_A -/ S_1Q_A difference spectrum of PSII. As these structures form, or are depleted in the $S_1 \rightarrow S_2$ transition, we expect difference peaks to appear in our spectra.

The protein backbone modes Amide IV, V and VI are all expected to vibrate within the range of 600 cm^{-1} to 725 cm^{-1} . Each of these could contribute to the difference spectrum. However, because we do not see large scale rearrangements in the protein matrix (as would be evidenced by large Amide I or Amide II difference peaks), the protein structural modes contributing to the difference spectrum in the low frequencies are, most likely, the result of small, localized changes of the protein in the immediate vicinity of the manganese cluster.

Other modes that could be contributing to the spectrum in the low-frequency region include the bending motion of carboxylate residues. It has been shown that carboxylates that bind metals, including manganese, display shifts in their infrared absorption spectra as the metal to which they are bound undergoes a change in redox level[56]. It is universally accepted that the manganese cluster is oxidized directly on the S_1 to S_2 transition, thus we can expect that any carboxylate residues that are ligated directly to the manganese will display redox dependent shifts of their bending vibrations.

Table 5-3 Low-Frequency Vibrations Possibly Present in Photosystem II

Structure	Approximate Vibrational Frequency (cm ⁻¹)
Protein Backbone Modes	
Amide V (NH _{ob} , CN _l) [*]	725
Amide IV (C _{ob} , CC _s , CNC _d)	625
Amide VI (CO _{ob} , CN _l)	600
Amide VII (NH _{ob} , CN _t , CO _{ob})	200
Ligand Side Chain Modes	
 bending	500-720
 Out-of-plane bending	600-650
 C-O-H bending (in plane)	600-720
Metal-Ligand Modes	
Mn=O	750
Mn-OH	400-500
	600-800
	600-700
Mn-Cl	300-400

* s, stretch; d, deformation, t, torsion; ib, in-plane-bend; ob, out-of-plane-bend

The EPR control studies performed on the dried samples demonstrated the presence of chlorophyll radicals generated by illumination with visible light. Because these are a light induced species it is conceivable that their presence contributes to the overall light induced difference spectrum. However no infrared studies have examined the changes exhibited in the low frequency region as neutral chlorophyll molecules are oxidized to the cation radical form. One possible indication of the relative contribution of chlorophyll radical to the difference spectrum comes from the control EPR studies. The light induced increase of the dark stable tyrosine EPR signal observed in O_2 -evolving versus tris-washed material shows that the tris-washed material exhibited a much larger light induced increase in amplitude after illumination. Based upon the line-width and g value of this new signal in the EPR spectrum, it is clear that a chlorophyll radical species is generated under illumination. Therefore, any signals in the FTIR spectrum that arise from the chlorophyll radical species should exhibit increased signal amplitude in the tris-treated material versus the O_2 evolving material. In Figure 5-17, the light-induced FTIR difference spectrum of tris-treated RCC samples, at 200 K, shows one mode, at 687 cm^{-1} , that has a slight increase in amplitude relative to the same peak in the O_2 evolving samples. This indicates that this peak may originate from a chlorophyll radical species, or from a new species that coincidentally vibrates at approximately 687 cm^{-1} . However, by the same argument, the fact that there are no substantial increases in signal intensity in the higher ($1800\text{-}1000\text{cm}^{-1}$) region of the spectrum indicates that chlorophyll radicals contribute only minimally to the overall light-induced difference spectrum.

The peaks observed below 1000 cm^{-1} could also have their origin in manganese-oxygen vibrations. In model compounds, vibrations that arise from manganese-oxygen

structures, such as di- μ -oxo structures, are seen in the range of 600 cm^{-1} to 700 cm^{-1} . in order to have confidence in our ability to detect these signals it is important to consider the extinction coefficients of the vibrations that we intend to observe. By measuring the infrared absorption spectrum of a model compound that contains the Mn_2O_2 structure, we calculated an extinction coefficient of approximately 10^6 mole^{-1} . We can assume 80 chlorophyll molecules per reaction center core particle[42], and that $3\mu\text{g}$ of chlorophyll are interrogated in each experiment. Each oxygen evolving complex, of which there is one per PSII, contains two Mn_2O_2 units. With these approximations, we calculate an expected absorbance of $\sim 10^4$ absorbance units due to the Mn_2O_2 structures present in the OEC. As can be seen from Figure 5-11, and the noise levels present in the spectra, that these levels are well within our instrumental detection capabilities.

A legitimate question that can be asked regards the peaks that might be observed from these manganese oxygen structures. As the di- μ -oxo core is oxidized by one electron, it might seem logical that the force constants of the individual bonds that make up this structure will change, leading to peaks in the difference spectrum of the system. However, one brief study on manganese-containing model compounds showed minimal change in the resonance Raman spectrum of these compounds as a function of oxidation state of the compound[57]. That does not preclude any di- μ -oxo structures in the oxygen evolving complex from displaying redox induced vibrational changes, however. It is known that the spectroscopic behavior of metal ligand structures can change dramatically when studied in highly asymmetric protein matrices as compared to the more symmetric conditions of small inorganic coordination compounds. More comprehensive studies of

the redox dependent vibrational properties of structurally relevant manganese model compounds need to be performed in order to draw conclusions about the contributions of these vibrations to the low frequency difference spectra of photosystem II.

As a set of control experiments, and ones that can start shed light on possible assignments of the low frequency modes, manganese depleted RCC samples were investigated under the same conditions as were the O₂ evolving samples. When the light-minus dark spectra of the Tris-treated samples were examined, the low frequency range of the spectrum was notable for its similarity to the low frequency region of the oxygen evolving samples. However, there were some potentially important differences. If any of the low frequency peaks observed in the O₂ evolving samples arise from manganese-oxygen vibrations, then samples that are depleted of manganese should not show those modes in a light induced difference spectrum. In Figure 5-23a, the 800-600 cm⁻¹ range of tris treated samples is overlaid with a spectrum of O₂ evolving samples. It can be seen that a peak at 632 cm⁻¹ in the O₂ evolving samples is not present in the spectrum of the tris treated samples. This observation could be attributed to one of two possible scenarios. The first is that the peak at 632 cm⁻¹ is, in fact, due to a manganese-oxygen or manganese ligand vibration. Under manganese depleted conditions, if this vibration is the result of a manganese-oxygen interaction then under manganese depleted conditions, it would not be observed. If the vibration were from a manganese-ligand interaction, then it would either not be observed if the vibration were primarily composed of normal coordinates from the manganese-ligand interaction, or it would be perturbed if it was composed of primarily

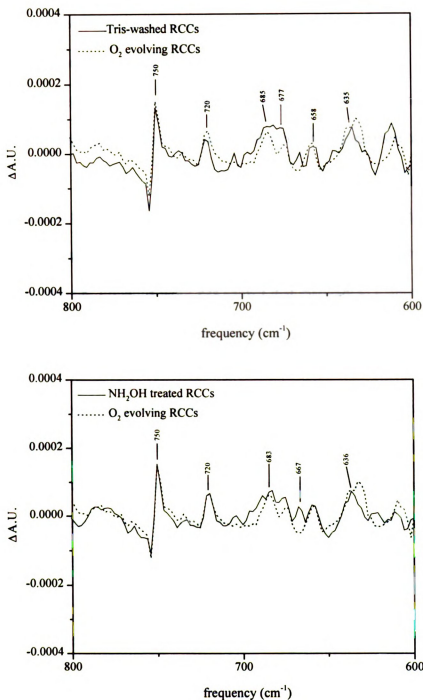


Figure 5-23: a) top 800-600 cm⁻¹ range of LI-FTIR difference spectrum of tris-washed and O₂ evolving RCC samples. 5000 scans (tris washed) and 6500 scans (O₂ evolving) respectively b) 800-600 cm⁻¹ range of NH₂OH and O₂ evolving RCCs. 4000 scans (NH₂OH) and 6500 scans (O₂ evolving)

ligand-based normal coordinates. As a control for these possible assignments, samples that were manganese depleted in an alternative way, by exposure to hydroxylamine, were investigated. It can be seen from Figure 5-23b that the same result was obtained. In manganese depleted samples, the vibration at 632 cm^{-1} that is present in oxygen evolving samples, is no longer present in samples that have had the manganese removed from the system.

If the vibration in question is the result of a manganese-oxygen interaction then its vibrational frequency should exhibit characteristic dependence upon the oxygen isotope present in the system. Previous work has shown that manganese atoms linked by a di- μ -oxo core, show a pronounced isotope shift of some of its low frequency modes of vibration upon labeling of the μ -oxo bridges with ^{18}O [58]. Our first attempt to label the PSII samples isotopically consisted of soaking the samples in FTIR buffer that was 97% enriched with ^{18}O . The samples were simply resuspended in the labeled buffer, and allowed to incubate for 12-14 hours, on ice in the dark. The sample did not perform any water oxidation chemistry during this dark incubation. The spectra from these samples appeared identical to the spectra obtained with ^{16}O labeled buffer (Figure 5-19). This is not surprising in light of the reported slow exchange kinetics of the bridging oxo groups proposed to be present in the OEC[58, 59]. In order to induce the bridges to exchange, we incubated PSII samples in the presence of ^{18}O labeled buffer, and an exogenous electron acceptor, 2,6 dichlorobenzoquinone. By incubating the samples on ice, under room light for 30 minutes, the samples undergo several cycles of catalytic chemistry. If the di- μ -oxo oxygen atoms are involved with the catalytic chemistry, then we expect them to exchange

easily under these conditions. Figure 5-24 shows the 800-600 cm^{-1} range of the FTIR spectrum of the samples treated in this manner. The peak at 632 cm^{-1} appears altered in these spectra. Unfortunately, our current experimental conditions do not allow us to examine modes that appear below 600 cm^{-1} , owing to the cutoff of the germanium filter we use to block the helium-neon laser beam that is coaxial with the IR probe beam. The results of the work we have performed on di- μ -oxo manganese complexes suggest that, under conditions of isotopic exchange, an isotopic shift of approximately 30 cm^{-1} to lower frequencies is expected, when the heavier isotope is exchanged into the bridging positions. So, if the 632 cm^{-1} peak is in fact due to a manganese-oxygen vibration, then, with the heavier isotope, the vibration would appear at the threshold of our current detection limits. As a result, definitive assignment is not yet possible.

Figure 5-22 shows the LI-FTIR spectra from Sr^{2+} substituted samples that exhibit the $g=4.1$ EPR signal. Recently, it has been proposed that the manganese cluster, under conditions in which it exhibits the $g=4.1$ EPR signal, is structurally different from the cluster under conditions that generate the multiline EPR signal. EXAFS studies have shown a significant lengthening of a Mn-Mn distance upon generation of the $g=4.1$ signal[14]. It has been shown in model compound studies that protonation of one of the bridging μ -oxo ligands of a Mn_2O_2 dimer not only causes a significant lengthening of the Mn-Mn distance, but also significantly alters the J-coupling between the two manganese ions. In this case, the study showed a decrease of antiferromagnetism (i.e more ferromagnetic coupling) upon protonation[60, 61], while another study showed an

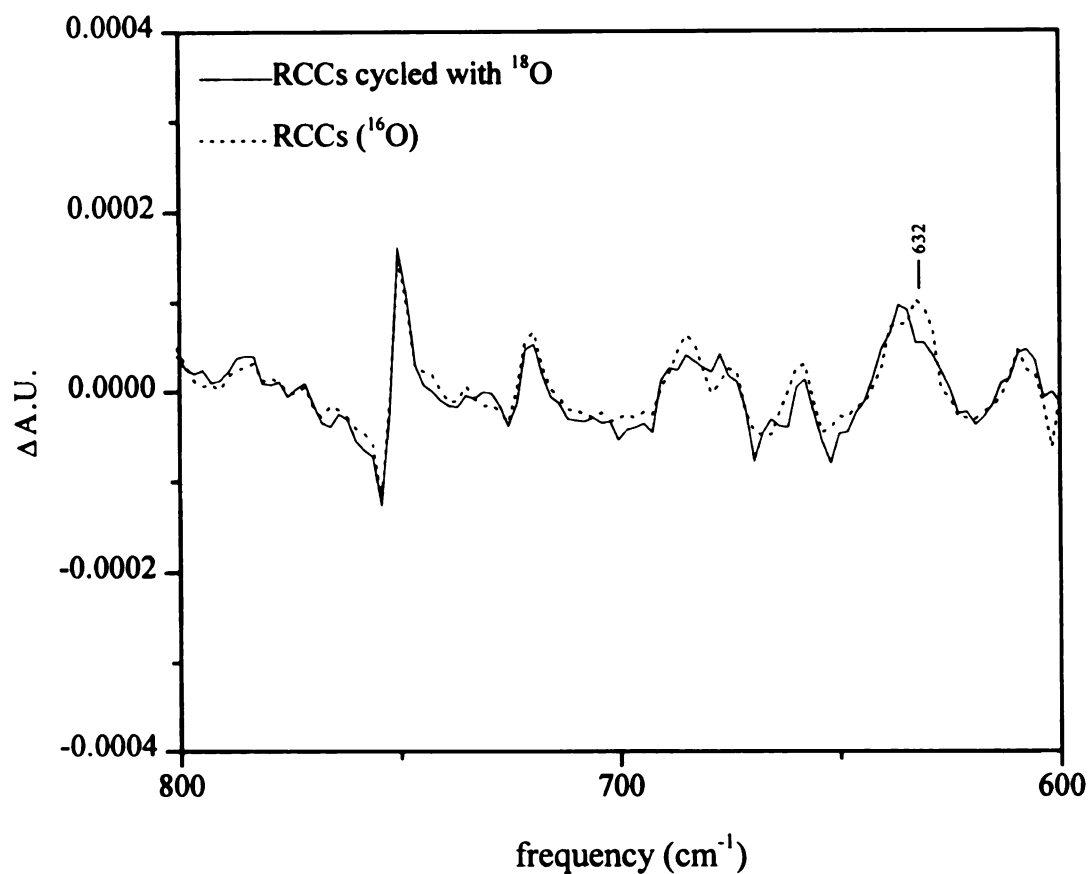


Figure 5-24: 800-600 cm^{-1} range of LI-FTIR spectrum of RCCs allowed to turnover in presence of ^{18}O labeled water. (dash) O_2 evolving RCCs (Figure 5-16).

increase in the antiferromagnetism upon protonation of a bridging oxo[62, 63]. Protonation, or any other structural rearrangement of the manganese cluster to form the $g=4.1$ signal, should be accompanied by an alteration of the vibrational properties of the manganese cluster. The FTIR difference spectrum of the Sr^{2+} substituted, $g=4.1$ samples shows some interesting differences when compared to the normal multiline generating samples. The differences include the addition of a shoulder at approximately 1560 cm^{-1} and the appearance of a new derivative shaped feature overlaying the peaks attributed to the calcium-binding carboxylate at $1364/1403\text{ cm}^{-1}$. In the low frequency region, there are some subtle differences, and the addition of some new peaks. In Figure 5-25 we can see new peaks appear at 650 cm^{-1} , 625 cm^{-1} and 619 cm^{-1} in the Sr^{2+} substituted samples. Also, there appear to be some pronounced differences between the Sr^{2+} substituted spectrum, and that of the O_2 evolving samples at approximately 675 cm^{-1} in the difference spectra. All of these peaks are in the region where Mn_2O_2 cores will exhibit vibrations. If the manganese cluster undergoes structural rearrangement as it forms the $g=4.1/\text{S}_2$ state, then this is the region where those changes would manifest themselves vibrationally.

Conclusions

We have reported here, for the first time, light-induced FTIR difference spectra of photosystem II of vibrations that occur below 1000 cm^{-1} . This region of the infrared spectrum is expected to contain information regarding vibrations due to 1) protein structural rearrangements upon changes of oxidation state of the manganese cluster 2) Protein derived metal ligands whose vibrations are perturbed by oxidation of the

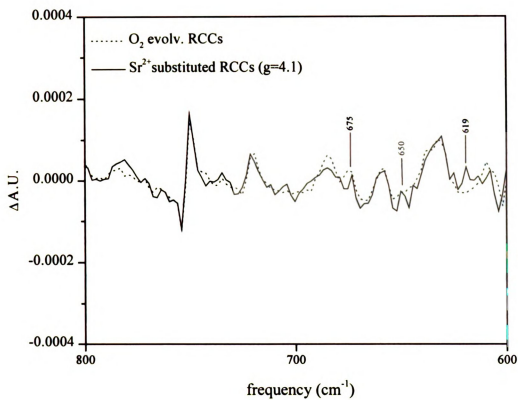


Figure 5-25: 800-600 cm^{-1} range of LI-FTIR spectrum of Sr^{2+} substituted RCCs. LI-FTIR spectrum of O_2 evolving samples shown for reference.

manganese cluster, and 3) metal-oxygen vibrations from species in which the oxygen atoms are either substrate derived, or are non-catalytically active atoms that are structural in nature. While we have not been able to make definitive assignments as of yet, the fact that we can observe these modes with adequate signal to noise ratios shows the promise of this technique for helping determine the mechanism of photosynthetic water oxidation. We are planning experiments where we will dismantle, then reassemble the manganese cluster in the presence of ^{18}O -labeled water. This will guarantee the incorporation of ^{18}O into the manganese cluster, which should provide definitive answers regarding the origin of the spectral features present in the LI-FTIR difference spectrum of PSII samples. We are currently in the process of developing the technology to extend the spectroscopic range of sensitivity of our instrumentation to 300 cm^{-1} , where almost all of the potential vibrations of structures proposed in the mechanism of water oxidation will be observable.

LIST OF REFERENCES

1. Pirson, A., *Z. Bot.*, 1937. **31**: p. 193.
2. Debus, R.J., *Biochim Biophys. Acta*, 1992. **1102**: p. 269.
3. Britt, R.D., in *Oxygenic Photosynthesis: The Light Reactions*, D.R. Ort and C.F. Yocum, Editors. 1996, Kluwer: Dordrecht. p. 137.
4. Diner, B.A. and Babcock, G.T., in *Oxygenic Photosynthesis: The Light Reactions*, D.R. Ort and C.F. Yocum, Editors. 1996, Kluwer: Dordrecht. p. 213.
5. Joliot, B., Barbieri, G., and Chabaud, R., *Photochem. Photobiol.*, 1969. **10**: p. 309.
6. Kok, B., Forbush, B., and McGloin, M., *Photochem. Photobiol.*, 1970. **11**: p. 457.
7. Dismukes, G.C. and Siderer, Y., *Proc. Natl. Acad. Sci.*, 1981. **78**: p. 274.
8. Hansson, O., Andreasson, L.-E., and Vanngard, T., *FEBS Lett.*, 1987. **185**: p. 151.
9. Andreasson, L.-E. and Hansson, O., *NH₃ treated ml samples*, in *Advances in Photosynthesis Research*, J. Biggins, Editor. 1987, Martinus Nijhoff/Dr. Junk Publishers: Dordrecht, The Netherlands. p. 503.
10. Beck, W.F., de Paula, J.C., and Brudvig, G.W., *J. Am. Chem. Soc.*, 1986. **108**: p. 4018.
11. Penner-Hahn, J.E., Fronko, R.M., Pecoraro, V.L., Yocum, C.F., Betts, S.D., and Bowlby, N.R., *J. Am. Chem. Soc.*, 1990. **112**: p. 2549.
12. MacLachlan, D.J., Hallahan, B.J., Ruffle, S.V., Nugent, J.H.A., Evans, M.C.W., Strange, R.W., and Hasnain, S.S., *Biochem. J.*, 1992. **285**: p. 569.
13. DeRose, V.J., *Ph.D. Thesis, University at California, Berkeley*. Lawrence Berkeley Laboratory Report LBL-16901. 1990.

14. Liang, W., Latimer, M.J., Dau, H., Roelefs, T.A., Yachandra, V.K., Sauer, K., and Klein, M.P., *Biochemistry*, 1994. **33**: p. 4923.
15. Rompel, A., *et al.*, *J. Am. Chem. Soc.*, 1997. **119**: p. 4465.
16. Yachandra, V.K., DeRose, V.J., Latimer, M.J., Mukerji, I., Sauer, K., and Klein, M.P., *Science*, 1993. **260**: p. 675.
17. Dau, H., Andrews, J.C., Roelefs, T.A., Latimer, M.J., Liang, W., Yachandra, V.K., Sauer, K., and Klein, M.P., *Biochemistry*, 1995. **34**(5274).
18. Cramer, S.P., Eccles, T.K., Kutzler, F., Hodgson, K.O., and Mortenson, L.E., *J. Am. Chem. Soc.*, 1976. **98**: p. 1287.
19. Kirby, J.A., Goodin, D.B., Wydrzynski, T., Robertson, A.C., and Klein, M.P., *J. Am. Chem. Soc.*, 1981. **103**: p. 5537.
20. Yachandra, V.K., Sauer, K., and Klein, M.P., *Chem. Reviews.*, 1996. **96**: p. 2927.
21. Hoganson, C.W., Personal communication
22. Baumgarten, M., Philo, J.S., and Dismukes, G.C., *Biochemistry*, 1990. **29**: p. 10814.
23. Boussac, A., Zimmerman, J.-L., and Rutherford, A.W., *Biochemistry*, 1989. **28**: p. 8984.
24. Tso, J., Sivaraja, M., Philo, J.S., and Dismukes, G.C., *Biochemistry*, 1991. **30**: p. 4740.
25. Boussac, A., Zimmerman, J.-L., Rutherford, A.W., and Lvergne, J., *Nature*, 1990. **347**: p. 303.
26. Ono, T. and Inoue, Y., *FEBS Letters*, 1991. **278**: p. 183.
27. Gilchrist, M.I., Ball, J.A., Randall, D.W., and Britt, R.D., *Proc. Natl. Acad. Sci.*, 1995. **92**: p. 9545.
28. Hoganson, C.W., Lydakis-Simantiris, N., Tang, X.-S., Tommos, C., Warncke, K., Babcock, G.T., Diner, B.A., McCracken, J., and Styring, S., *Photosynth. Res.*, 1995. **46**: p. 177.
29. Ghanotakis, D.F., Babcock, G.T., and Yocum, C.F., *FEBS Letters*, 1984. **167**: p. 127.

30. Tang, X.-S., Randall, D.W., Force, D.A., Diner, B.A., and Britt, R.D., J. Am. Chem. Soc., 1996. **118**(7638).
31. Tommos, C., Tang, X.-S., Warncke, K., Hoganson, C.W., Styring, S., McCracken, J., Diner, B.A., and Babcock, G.T., J. Am. Chem. Soc., 1995. **117**: p. 10325.
32. Sigel, H. and Sigel, A., *Metal Ions in Biological Systems*. Vol. 30. 1994: Marcel Dekker, Inc., USA.
33. Frey, P.A., Chem. Rev., 1990. **90**: p. 1343.
34. Blomberg, M.R.A., Siegbahn, P.E.M., Styring, S., Babcock, G.T., Akermark, B., and Korall, P., J. Am. Chem. Soc., submitted, .
35. Baldwin, M.J. and Pecoraro, V.L., J. Am. Chem. Soc., 1996. **118**: p. 11325.
36. Caudle, M.T. and Pecoraro, V.L., J. Am. Chem. Soc., submitted, .
37. Gardner, K.A. and Mayer, J.M., Science, 1995. **269**: p. 1849.
38. Varotsis, C. and Babcock, G.T., Biochemistry, 1990. **29**: p. 7357.
39. Varotsis, C., Woodruff, W.H., and Babcock, G.T., J. Biol. Chem., 1990. **265**: p. 11131.
40. Brudvig, G.W., Casey, J.L., and Sauer, K., Biochim. Biophys. Acta, 1983. **723**: p. 366.
41. Berthold, D.A., Babcock, G.T., and Yocum, C.F., FEBS Letters, 1981. **134**: p. 231.
42. Ghanotakis, D.F. and Yocum, C.F., FEBS Letters, 1986. **197**: p. 244.
43. Mishra, R.K. and Ghanotakis, D.F., Photosyn. Res., 1994. **42**: p. 37.
44. Cheniae, G.M. and Martin, I.F., Plant Physiol., 1971. **47**: p. 568.
45. Miller, A.-F. and Brudvig, G.W., Biochemistry, 1990. **29**: p. 1385.
46. Tamura, N. and Cheniae, G.M., Biochim. Biophys. Acta, 1987. **890**: p. 179.
47. Barry, B.A. and Babcock, G.T., Proc. Natl. Acad. Sci., 1987. **84**: p. 7099.

48. Noguchi, T., Ono, T., and Inoue, Y., *Biochim. Biophys. Acta*, 1993. **1143**: p. 333.
49. Noguchi, T., Ono, T., and Inoue, Y., *Biochemistry*, 1992. **31**: p. 5953.
50. Noguchi, T., Ono, T., and Inoue, Y., *Biochim. Biophys. Acta*, 1995. **1228**: p. 189.
51. Steenhuis, J.J. and Barry, B.A., *J. Am. Chem. Soc.*, 1996. **118**: p. 11927.
52. Hienerwadel, R., Boussac, A., Breton, J., and Berthomieu, C., *Biochemistry*, 1996. **35**: p. 15447.
53. Noguchi, T. and Inoue, Y., *FEBS Letters*, 1995. **370**: p. 241.
54. Berthomieu, C., Navedryk, E., Mantele, W., and Breton, J., *FEBS Letters*, 1990. **269**: p. 363.
55. MacDonald, G.M., Steenhuis, J.J., and Barry, B.A., *J. Biol. Chem.*, 1995. **270**: p. 8420.
56. Smith, J.C., Gonzales_Vergara, E., and Vincent, J.B., *Inorg. Chim. Acta*, 1997. **255**: p. 99.
57. Dave, B.C. and Czernuszewicz, R.S., *Inorg. Chim. Acta*, 1994. **227**: p. 33.
58. Cooper, S.R. and Calvin, M., *J. Am. Chem. Soc.*, 1977. **99**: p. 6623.
59. Carroll, J.M. and Norton, J.R., *J. Am. Chem. Soc.*, 1992. **114**: p. 8744.
60. Baldwin, M.J., Gelasco, A., and Pecoraro, V.L., *Photosyn. Res.*, 1993. **38**: p. 303.
61. Baldwin, M.J., Stemmler, T.L., Riggs-Gelasco, P.J., Kirk, M.L., Penner-Hahn, J.E., and Pecoraro, V.L., *J. Am. Chem. Soc.*, 1994. **116**: p. 11349.
62. Dube, C.E., Wright, D.W., and Armstrong, W.H., *J. Am. Chem. Soc.*, 1996. **118**: p. 10910.
63. Hagen, K.S., Westmoreland, T.D., Scott, M.J., and Armstrong, W.H., *J. Am. Chem. Soc.*, 1989. **111**: p. 1907.

MICHIGAN STATE UNIV. LIBRARIES



31293015707791